CA1 pyramidal cells as computing units: From inputs to output

Dissertation

presented by

Antonio Benjamín Yáñez Santamaría

February 2018

University of Heidelberg

Dissertation

submitted to the

combined faculties for the Natural Sciences and for Mathematics

of the Ruperto-Carola University of Heidelberg, Germany

for the degree of

Doctor of Natural Sciences

presented by

Diplom-Phys Antonio Benjamín Yáñez Santamaría

born in A Coruña, Galicia, Spain

Oral-examination: 20 April 2018

.....

.....

.....

Referees: Prof. Dr. Andreas Draguhn
Prod. Dr. Stephan Frings

Mais son probe e, mal pecado!,
a miña terra n'é miña,
que hastra lle dan de prestado
a beira por que camiña

Rosalía de Castro

Si no fuera porque hice colocado
el camino de tu espera
me habría desconectado

Robe Iniesta

Aber Zeit ist Leben.
Und das Leben wohnt im Herzen.
Und je mehr die Menschen daran sparten,
desto weniger hatten sie

Michael Ende

Nos volveremos a ver
cuando salgamos del túnel
tumbando alguna pared
para poder ver las nubes

La Raíz

Contents

List of Figures

List of Tables

List of abreviations

AcD	Axon carrying Dendrite
ACSF	Artificial Cerebro Spinal Fluid
AIS	Axon Initial Segment
AMPA	α-amino-3-hydroxy-5-methyl-4-isoxazolepropionic acid)
AP	Action Potential
APV	(2R)-Amino-5-Phosphonopentanoate
ATP	Adenosine TriPhosphate
CA	Cornu Ammonis
CC	Current Clamp
DG	Dentate Gyrus
DS	Dendritic Spike
eAP	ectopic Action Potential
EC	Entorhinal Cortex
EPSC	Excitatory Post Synaptic Current
EPSP	Excitatory Post Synaptic Potential
GABA	Gamma Amino Butiric Acid
GHK	Goldman-Hodgkin-Katz
HCN	Hyperpolarization-Activated cyclic Nucleotidegated
ICA	Independent Component Analysis
IPSC	Inhibitory Post Synaptic Current
IPSP	Inhibitory Post Synaptic Potential
LFP	Local Field Potential
LSTM	Long Short Term Memory
MAD	Median Absolute Deviation
MNIST	Modified National Institute of Standards and Technology
NMDA	N-Methyl-D-Aspartate

nonAcD	non Axon carrying Dendrite
PSC	Post Synaptic Current
PSP	Post Synaptic Potential
PV	ParValvumin
RC	Resistor-Capacitor
relu	rectified linear unit
RMSprop	Root Mean Square propagation
SGD	Stochastic Gradient Descent
SL	Shunting Level
SNR	Signal to Noise Ratio
SPW-r	SharP Wave ripples
TTX	TeTrodoXin
VC	Voltage Clamp

Abstract

Pyramidal cells of the CA1 area in the hippocampus are one of the most studied neurons nowadays due to their role in memory formation or spatial navigation. CA1 pyramidal cells possess an apical dendrite which receives excitatory synaptic input mainly from CA3 axons.

To better understand apical synaptic input to these neurons, a new recording technique is proposed to measure excitatory synaptic input applied onto neurons. First, the theoretical derivations are presented. Then, the technique is applied to measure CA1 pyramidal cells and finally a computational model studies in depth the influence of the distance between synaptic input and recording on the estimation. The conclusion is that the method cannot improve current experimental techniques.

In addition, in some cases the axon of a neuron stems out of a dendrite rather than out of the soma. This particular morphology favors synaptic inputs onto this dendrite to generate action potentials. A computational model is applied to characterize the propagation of synapses from dendrites to the axon in a neuron with this feature. The model shows that electronic propagation is responsible of this favorable action potential generation.

Finally, extracellular stimulation of the axons of CA1 pyramidal cells generates ectopic action potentials with a bimodal distribution of time to arrive to the soma. The computational model suggests that this bimodal distribution is due to two different sites of action potential initiation, namely the axon initial segment and the first node of ranvier.

Zusammenfassung

Pyramidenzellen der Region CA1 des Hippokampus sind heutzutage durch ihre Rolle in der Gedächtnisbildung oder in der rumlichen Navigation eine der meist untersuchten Nervenzellen. Diese Neurone besitzen Fortsätze, die Dendriten, die sich vom Zellkörper ausgehend verzweigen und Eingangssignale von anderen Zellen erhalten. Der apikale Dendrit der CA1 Pyramidenneurone erhält vor allem erregende synaptische Eingangssignale von der Region CA3 des Hippokampus.

Um die Eingangssignale von CA3 näher zu untersuchen, wurden exzitatorischen synaptischen Eingänge mit einer neuen Messmethode gemessen. Zuerst wurden die theoretischen Ableitungen dargelegt. Auerdem wurden Messungen mit der neuen Technik an CA1 Pyramidenzellen durchgefhrt. Schlielich konnte mit einem Computermodel der Einfluss des Abstandes des synaptischen Signals und der Position der Messung analysiert werden. Zusammenfassend, konnte keine Verbesserung der momentanen experimentellen Techniken durch die neue Methode gezeigt werden.

Das Axon von Nervenzellen stellt eine weitere Art von Fortsatz dar, der das Aktionspotential als Ausgangssignal der Neurone erzeugt. Das Axon kann in manchen Fllen, nicht wie üblich vom Zellkörper, sondern von einem basalen Dendriten ausgehen. Diese spezielle Morphologie begnstigt synaptische Eingangssignale auf diese Dendriten um ein Aktionspotential zu generieren. Mit Hilfe eines Computermodells wurde die Weiterleitung der synaptischen Eingänge von Dendriten zum Axon in diesen besonderen Neuronen charakterisiert. Das Model zeigte, dass eine elektrotonische Weiterleitung die gnstigere Erzeugung eines Aktionspotentials verursacht.

Zuletzt wurden mit dem Computermodel ektopische Aktionspotentiale untersucht. Extrazelluläre Stimulation des Axons von CA1 Pyramidenzellen generiert ektopische Aktionspotentiale mit einer bimodalen zeitlichen Verteilung. Das Model zeigte, dass die bimodale Verteilung auf zwei verschiedene Regionen der Aktionspotential Generierung zurck zu führen ist. Die zwei Regionen sind das Axon Initialsegment und der erste Ranviersche Schnürring.

1 Introduction

1.1 Hippocampal neuroanatomy

The hippocampus is a region of the mammalian brain located in the temporal lobe. The name derives from its similarity to the seahorse (greek: hippokampos). This area is generally associated with memory formation and spatial navigation. One of the first studies that drew attention to the hippocampus and its implications in memory formation involved the patient H.M. (Scoville and Milner, 1957; Milner et al., 1968). Upon removal of his medial temporal lobes, the patient experienced serious impairments in creating new memories, despite keeping other cognitive functions.

The hippocampus is composed of two U-shaped structures named dentate gyrus (DG) and the cornu ammonis (CA), which is further divided into four regions: CA1, CA2, CA3 and CA4 (figure 1.1). Anatomically, the hippocampus shares with other cortical areas the layer division. The dentate gyrus has a granule cell layer, where the somata of the granule cells reside, and a molecular layer where dendrites are located. The cornu ammonis is divided in stratum oriens, pyramidale, radiatum and lacunosum moleculare. The hippocampus proper is adjacent to the subicullum, parasubicullum and the entorhinal cortex. Collectively, these regions are denoted hippocampal formation.

The dentate gyrus is the main input site of the hippocampus. The most important afferents come from the entorhinal cortex. Projections from layer II of the entorhinal cortex arrive to the dentate gyrus through the perforant pathway. Another part of the perforant pathway connects layer III of the EC to the CA1 pyramidal cells in the stratum lacunosum moleculare. Furthermore, it receives more inputs from the septal nuclei, hypothalamus and locus coeruleus.

The trisynaptic pathway is seen as the main information flow within the hippocampus. This pathway starts in the dentate gyrus and projects to the CA3 via the mossy fibers. Then, CA3 pyramidal cells project to the CA1 area through the schaffer collaterals

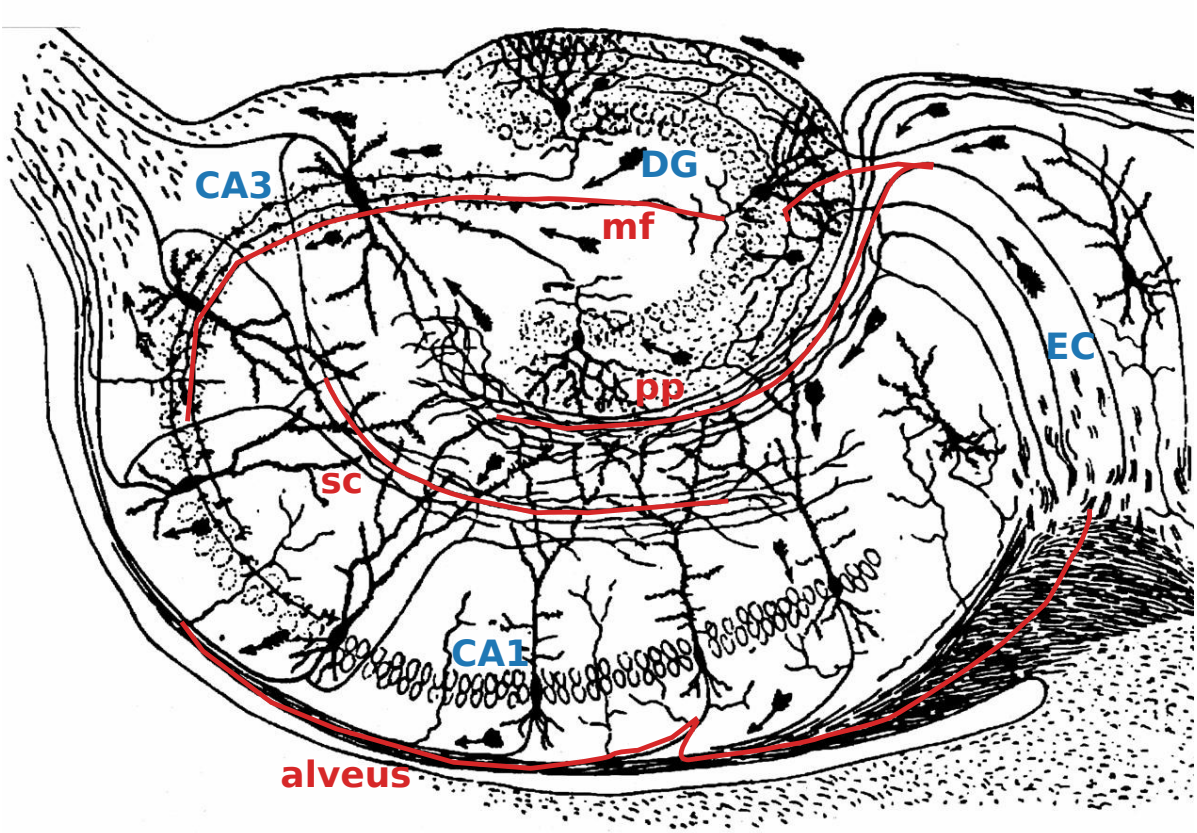

Figure 1.1: Overview of the hippocampal formation. The main regions marked in blue: Entorhinal Cortex, Dentate Gyrus, CA3 and CA1. The main pathways marked in red: perforant path, mossy fibers, schaffer collaterals and alveus. Adapted from (Ramón y Cajal, 1911)

(figure 1.1). From CA1, the hippocampus projects back to the entorhinal cortex, with proximal pyramidal neurons projecting to the medial entorhinal cortex and most distal ones to the lateral entorhinal cortex (Andersen, 2007a).

The CA1 area is one of the most widely studied structures of the brain. After the first recording of place fields (O'Keefe and Conway, 1978) from CA1 pyramidal cells, it became clear that the hippocampal cells act as a cognitive map of the space.

The cornu ammonis is divided in pyramidal cell layer (stratum pyramidale) where the somata of the pyramidal cells are found. Deeper than the stratum pyramidale is the stratum oriens, where the basal dendrites and many interneurons are located. Deeper than the stratum oriens in the CA1 area is the alveus, where bundles of pyramidal axons project outside the hippocampus . Superficially to the pyramidal cell layer is the stratum radiatum, where the apical dendrites are located. The most distal apical dendrites are

located in a final layer, named stratum lacunosum moleculare (figure 1.2).

Pyramidal cells constitute the main excitatory population in the CA1 area. These cells are surrounded by a rich diversity of up to 21 different types of interneurons with different molecular markers and projections (Klausberger and Somogyi, 2008). The most important ones are basket cells which provide perisomatic inhibition Also, axo-axonic chandelier cells regulate spike initiation and timing projecting in the vicinity of the axon initial segment (AIS).

As explained above, the laminar structure of the hippocampus separates input integration and output sites spatially. Furthermore, this laminar structure, together with input synchronicity, allows the small post synaptic currents to collectively create a macroscopically measurable field potential, which can be recorded extracellurarly. This local field potential (LFP), contains frequencies of up to 400 Hz (Brette and Destexhe, 2012).

1.1.1 Pyramidal cells in the CA1 area

On the dawn of electrophysiology, most of the characterization and analytical modeling of neurons was applied to motoneurons (Lorente De Nó, 1947; Rall, 1960). In recent decades, CA1 pyramidal cells gradually replaced motoneurons as the archetypical neuron to measure and model computationally (Spruston et al., 1994; Nevian et al., 2007; Gasparini and Magee, 2006; Remy et al., 2009). One reason for this shift is that CA1 pyramidal cells have higher cognitive functions than the action potential (AP) relay of motoneurons. Furthermore, the straightforward laminar structure of the hippocampus allows to easily identify different targets, namely, basal and apical inputs. Basal dendrites of CA1 receive mainly afferents from CA2 and interneurons. Apical dendrites receive afferents from the CA3 in the proximal part (stratum radiatum) and from the EC in the distal (stratum lacunosum moleculare) (figure 1.2).

CA1 pyramidal cells present a rich variety of ionic channels. The density of these channels is sometimes distance dependent. For instance, there is an increase density of A-type potassium channels (Hoffman et al., 1997) and HCN (Lörincz et al., 2002) channels along the apical dendrite.

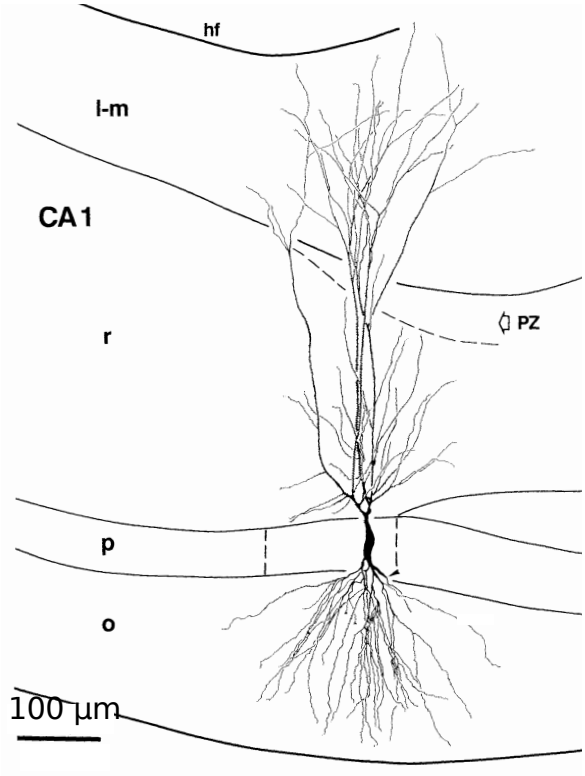

Figure 1.2: CA1 pyramidal cell and the laminar structure of the CA1 area. Adapted from (Ishizuka et al., 1995)

Magnitude	Typical units	Description
c_m	nF	membrane capacity
E	mV	electric resting potential
RT	J/mol	thermal energy
F	C	charge of one mol
P	cm/s	permeability of the membrane
I/i	nA	transmembrane current
g_l	μS	leakage conductance
V	mV	membrane potential
E_l	mV	leakage reversal potential
λ	μm	length constant
g_{in}	μS	axial conductance
g_{syn}	μS	maximum synaptic conductance
τ	ms	time constant

Table 1.1: Magnitudes described in the introduction

1.2 Biophysics of the neuronal membrane

The cellular membrane is composed of a lipid bilayer. Its main components are amphiphilic phospholipids. These molecules possess a lipophilic tail and a hydrophylic head. They aggregate forming two layers that are bound to one another at the lipophilic tails, forming the outside surface of the cell. The hydrophilic, polar heads are present at both sides of the membrane and are in contact with both the cytoplasm and the extracellular space.

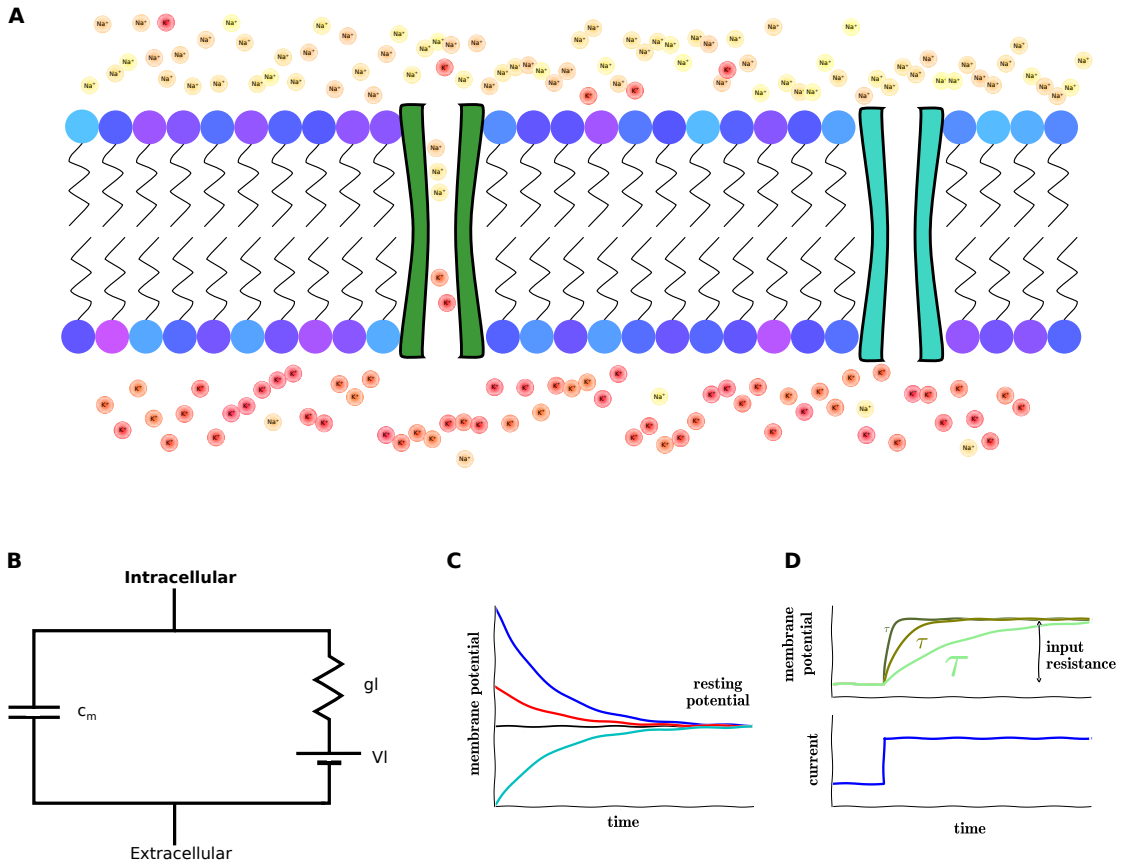

Figure 1.3: Schematic of the cell membrane and basic circuit behavior. (A) Diagram of the lipid bilayer with Na^+ions in the extracellular space and K^+ions in the cytoplasm. (B) Electric circuit representation of the membrane, where the membrane and its holes are represented by a capacitor and a resistor, respectively.. (C) The membrane behaves as a RC circuit where the time constant ($\tau = RC$) sets the timescale at which the membrane relaxes to the resting membrane potential. (D) After a current injection, larger (smaller) values of the time constant make the membrane achieve slower (faster) the new target potential.

As the heads of the lipids have a negative polarity, they can attract positive ionic charges nearby. Thus, ions with opposite charges accumulate at either side of the membrane. In electrical terms, the membrane is acting as a capacitor, i.e., a charge storage. The amount of charge (Q) the membrane can store depends on the membrane capacitance (c_m) as well as the area (S) of the membrane and the difference of potential (V) between both sides of the membrane:

$$Q = S \times c_m \times V \tag{1.1}$$

In addition to that, the membrane can host a variety of proteins which allow the passive or active transmission of ions through the membrane. The most important is the A-type potassium channels which are tonically open and conduct potassium outside of the cell. Also, the Na^+/K^+-ATPase plays an important role. This enzyme uses ATP and pumps 3 Na^+ions to the extracellular space while pumping 2 K^+ions into the cytoplasm. Overall there is a net gain of charge in the outside of the cell, and thus the inside becomes negatively polarized with respect to the extracellular space (usually set as reference at $0mV$). Typical resting membrane potentials of neurons can range from -80 to $-60mV$.

When there is a concentration gradient, two opposing forces are competing. First, diffusion tends to equilibrate the concentration and thus diffuminate the gradient. On the other hand, ions also react to an existing electric field and moving towards the lowest potential. In equilibrium conditions, the two forces balance and there is no net movement of ions. In such case, there is an equilibrium potential that balances the gradient and is given by the Nernst equation:

$$E_{ion} = \frac{RT}{F} \ln \frac{[in]}{[out]} \tag{1.2}$$

where R is the gas constant, T is the absolute temperature and F is the charge of one mole of electrons. In the case of the membrane, there are several ionic species, each of which has a different permeability through the membrane. For that case, the equilibrium potential can be calculated from the Goldman-Hodgkin-Katz (GHK) voltage equation (Goldman, 1943; Hodgkin and Katz, 1949), which applied to K^+, $Na^+$and Cl^-yields

$$E_m = \frac{RT}{F} \ln \frac{P_{K^+}[K^+]_{in} + P_{Na^+}[Na^+]_{in} + P_{Cl^-}[Cl^-]_{in}}{P_{K^+}[K^+]_{out} + P_{Na^+}[Na^+]_{out} + P_{Cl^-}[Cl^-]_{out}} \tag{1.3}$$

where P represents the permeability of different species through the membrane. Plugging into the equation the relative concentrations of these ions measured in the squid giant axon yields a membrane reversal potential of $-60mV$ (Sterratt et al., 2011).

One important issue of this view is that the current flowing depends not only on the potential different between cytoplasm and extracellular space, but also on the relative concentrations at both sites. Thus, current is not completely linear with respect to potential and the membrane is not ohmic. Assuming that the concentration of both sites does not change much and within the range where most physiological membrane potentials occur $(-100, 50)mV$, the flow of current through the membrane can be further simplified to follow Ohm's law:

$$I_m = g_l(V - E_L) \tag{1.4}$$

where the current is proportional to the deviation of the membrane potential from the equilibrium potential from equation 1.3. This proportionality, the leakage conductance, accounts for the weighted permeability of all ionic species. This approximation is the standard to apply to the membrane, as it enables to apply all linear circuit theory to solve for the membrane potential. Nevertheless, attempts to characterize the full solution of the diffusion-drift problem have been recently made (Pods et al., 2013).

1.2.1 General membrane equation

As stated above the hydrophilic nature of the lipid bilayer can be modeled as a capacitor between the extracellular space and cytoplasm. Moreover, the permeability of certain ions through the membrane due to gradients can be modeled as a conductance in parallel with the capacitor. Thus, the membrane can be simply described in terms of an electric circuit (figure 1.3 B).

$$c_m \frac{dV}{dt} = g_l(E_l - V) \tag{1.5}$$

or, equivalently,

$$\frac{dV}{dt} = \frac{(E_l - V)}{\tau} \tag{1.6}$$

where $\tau = c_m/g_l$ is the membrane time constant of the neuron. For membrane potentials below the leakage reversal potential (hyperpolarized), the rate of change of the membrane potential ($\frac{dV}{dt}$) is positive and thus the membrane potential will depolarize until the equilibrium is reached. Conversely, for depolarized potentials $\frac{dV}{dt}$ is negative so it will repolarize to E_l (figure 1.3 C). The time constant sets the time scale in which this process occur, and can also be recorded as the time it takes to respond to a current injection. Smaller values of τ will yield a faster charging time whereas bigger values of τ will make the recharging slower (figure 1.3 D). Finally, the ratio between the membrane potential shift and the injected current that causes the shift is the input resistance of the neuron.

In summary, a circuit containing a resistor and a capacitor (RC circuit) can be used to describe the membrane. From the capacitance and the conductance, two magnitudes of physiological importance can be directly obtained: the time constant ($\tau = c_m/g_l$) and the input resistance ($R_{in} = 1/g_l$).

1.2.2 Cable theory

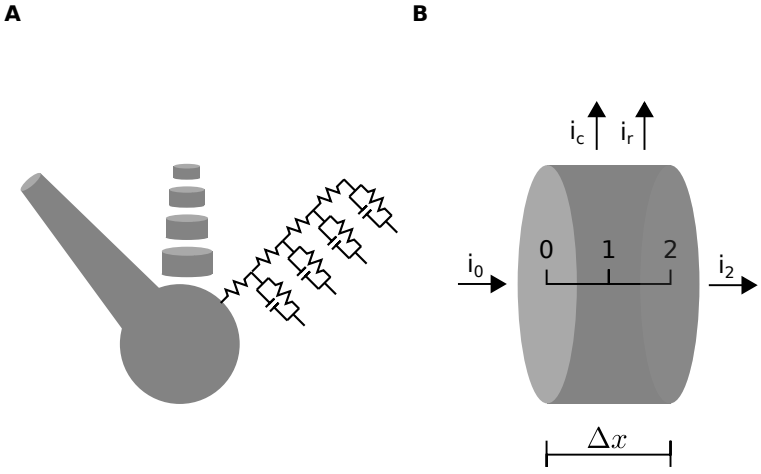

Figure 1.4: Cable theory schematic. (A) Spherical soma with a full dentrite (left), a compartmentalized dendrite (center) and the equivalent circuit (right). (B) Patch of a cylindrical dendrite of length Δx with axial currents at both ends (i_2 and i_0) and resistive and capacitive transmembrane currents (i_c and i_r).

So far, only two points in space have been considered: The extracellular space and the cytoplasm. The underlying assumptions have been that either a single compartment cell

is considered, or both the extracellular space and the inside of the neuron are isopotential, i.e., they have the same potential throughout their extension. Single compartment cells are powerful and computationally efficient models for implementation in bigger network models, although they reduce the whole behavior of a cell to a single equation (Dayan and Abbott, 2005). When considering a cell with a given morphology, it is acceptable to use a multicompartmental cell,assuming the extracellular space to be isopotential due to its low resistance (Brette and Destexhe, 2012). However, the internal resistance of the neuron must be considered.

Multicompartmental computational models recreate neurons as a set of cylindrical patches of neuronal membrane joined by an internal resistance (Carnevale and Hines, 2006) (figure 1.4 A). Moreover, for simple geometries such as a uniform dendrite, an analytical solution can be addressed. What follows is the general cable equation based in the works of Wilfrid Rall (Rall, 1967; Rall, 1969) and can be found in many textbooks (Johnston and Wu, 1995; Dayan and Abbott, 2005; Sterratt et al., 2011).

Let us first consider a patch of cylindrical dendrite of radius a and length Δx (figure 1.4 B). The patch has a resistance and capacitance per unit area r_l and c_m, respectively, and an axial resistivity per unit length r_a. Furthermore, being the dendritic diameter small, it can be safely assumed that the patch is isopotential. The current that traverses a short dendritic patch is given by Ohm's law,

$$\Delta V = r_a \frac{\Delta x}{\pi a^2} i_a \tag{1.7}$$

taking the limit for small displacements, we have

$$i_a = \frac{\partial V}{\partial x} \frac{\pi a^2}{r_a} \tag{1.8}$$

which means that the current flows towards the site of the dendrite of lesser potential. The membrane is not impermeable to current flowing through. Rather, there is a capacitive current and an leakage current through the membrane. By conservation of charge, all currents from figure 1.4 B must equal to 0. Thus,

$$i_2 - i_1 = i_c + i_r \tag{1.9}$$

or, from equations 1.5, 1.8

$$\frac{\partial V_2}{\partial x}\frac{\pi a^2}{r_a} - \frac{\partial V_0}{\partial x}\frac{\pi a^2}{r_a} = \frac{\partial V_1}{\partial t} c_m 2\pi a \Delta x + (V_1 - E_l)\frac{2\pi a \Delta x}{r_l} \tag{1.10}$$

dividing everything by $2\pi a \Delta x$ we arrive at

$$\frac{a}{2r_a \Delta x}\left(\frac{\partial V_2}{\partial x}\frac{\partial V_0}{\partial x}\right) = cm\frac{\partial V_1}{\partial t} + \frac{V_1 - E_l}{r_l} \tag{1.11}$$

the right side of the equation, in the limit for short patches is the second derivative of the membrane potential with respect to position. Furthermore, to express the general cable equation in the natural units of the system, the following substitutions can be made: $\tau = c_m r_l$, $\lambda = \sqrt{\frac{a r_l}{2 r_a}}$ to have

$$\lambda^2 \frac{\partial^2 V}{\partial x^2} = \tau \frac{\partial V}{\partial t} + V - E_l \tag{1.12}$$

this equation is the same as a well known physics problem, the heat equation. Although it only applies to a uniform cylinder, many insights can be taken from general dendritic behavior. First of all, in the case of equilibrium, all derivatives are 0 and thus $V = E_l$, so the tendency of the neuron is to be at its resting membrane potential. Furthermore, when a perturbation is produced, i.e., as post synaptic potential (PSP) or an ionic current, it will propagate along the dendrite through time and space while decaying. The scale at which it decays is given by the natural units of the system, the length and time constants.

1.2.3 Active conductances

So far, only the capacitance and the tonic component of ionic permeability has been introduced. Indeed, the membrane also possesses a rich variety of voltage and G-protein coupled channels with very precise kinetics that account for the excitability of the membrane.

The formalism introduced by Hodgkin and Huxley (Hodgkin and Huxley, 1952) was the first attempt to describe the kinetics of voltage activated channels. In that study, they described the ionic currents in terms of a reversal potential for each ionic species and a variable conductance dependent on two gating variables: activation and inactivation

(only to Na^+conductance).

$$I_{Na^+} = m^3 h(V - E_{Na^+}) \tag{1.13}$$

$$I_{K^+} = n^4(V - E_{K^+}) \tag{1.14}$$

The gating variables are described by first order equation with voltage-dependent time values and time constant. Finally, there is also a temperature dependent factor. Altogether, these equations can describe the dynamics of action potential initiation and propagation along the giant squid. Although initially these equations were only implemented to fit experimental data, functional meaning was given later. For instance, the delayed rectifier potassium channel is composed of four subunits, and all need to be open in order for the channel to permeate. If n is the probability that a subunit is open, and the opening of individual subunits is independent, then n^4 is the probability that all four subunits are open simultaneously. The notion that the kinetics of individual subunits and channels is independent allows for stochastic treatment. However, recently it has been proposed that cooperation of sodium channels can accelerate onset of action potentials and thus process signals of frequencies up to frequencies in the order of kilohertz (Naundorf et al., 2006; Tchumatchenko and Wolf, 2011; Huang et al., 2012). Analogous studies have been made to characterize other ionic channels (Hille, 2001).

Synaptic inputs are along with gap junctions the mechanisms by which neurons receive inputs from other neuron. There is a big variety of neurotransmitters and receptors. The two most common receptors are the glutamatergic AMPA receptor and the GABAergic GABA_A receptor. Their kinetics are again modeled by a conductance change and a reversal potential which is close to $0mV$ for excitation and the reversal potential of $Cl^-$for inhibition. The conductance change is modeled by the sum of two exponentials, one fast which is the opening and a slower decay.

The analytical solution of active conductances is intractable. However, the addition of active mechanisms to computational models is straightforward and allows for comprehensive characterization of the behavior or neurons.

1.3 Theoretical techniques

1.3.1 Computational Modeling

The main idea underlying the definition and applications of the instantaneous time constant deals with how excitatory conductances change the passive properties of neurons. The pioneer works of Rall (Rall, 1957; Rall, 1959; Rall, 1960) set the foundations of electrical propagation of signals within neurons. This work has been followed my many other who have contributed to the understanding of this field (Koch et al., 1983; Koch et al., 1990; Segev and Rall, 1998; Shepherd et al., 1985).

In parallel of the passive understanding of the neurons the work of Hodgkin and Huxley (Hodgkin and Huxley, 1952) laid the foundation of active generation of action potentials. In their 1952 study (Hodgkin and Huxley, 1952), they characterized quantitatively for the first time the generation and propagation of action potentials in the squid giant axon. The analytical treatment proposed in their works opened the door to the characterization of voltage dependent ionic channels and has been deeply influential over decades. Their works have been followed my many others (see (Hille, 2001; Sterratt et al., 2011; Catterall et al., 2012) for extensive details), which applied the formalism of Hodgkin and Huxley to quantify the dynamics of voltage and concentration gated channels. Many of these characterization were possible thanks to the technical breakthrough of the patch clamp technique (Neher and Sakmann, 1976), which allowed for massive data recording on single and multiple channels.

All the knowledge of passive and active components of neurons has been incorporated into computational models, among which the NEURON environment stands out (Hines, 1984; Hines and Moore, 1997; Carnevale and Hines, 2006; Hines et al., 2009). This framework has led to the construction of complex biophysical models on which state of the art computational models have been built (Jarsky et al., 2005).

As the complexity of these models grows, it increases its capacity to imitate the normal physiological functioning of the neuron. On the other hand, this complexity also obscures the synthesis of the biophysical principles into magnitudes easy to interpret and to measure experimentally.

In this aspect, several magnitudes have been proposed, like the shunting level (SL, (Gidon and Segev, 2012)), passive normalization (Jaffe and Carnevale, 1999) or a rule of non linear summation (Hao et al., 2009). All these magnitudes follow directly from

theoretical principles and try to reduce it to a magnitude easy to interpret from a physiological point of view and also easy to test experimentally.

(Gidon and Segev, 2012) have proposed the shunting level, with is defined as the change in input resistance that an arbitrary synapse exerts onto a particular location. Its value ranges between 0 (no effect) and 1 (completely cancels the input resistance at that location). Using their formalism, they arrive to the conclusion that inhibitory inputs are most effective when they are not located between the excitatory inputs and the soma. This contradicts the intuitive notion that inhibition is most effective when located between excitation and soma (on-path inhibition, (Koch et al., 1983)), yet conclusive evidence about off-path inhibition is yet to come.

(Jaffe and Carnevale, 1999) have extensively studied the transfer between excitatory synaptic inputs at their application site and a fixed point (soma in most cases). The careful application of this formalism to different reconstructed morphologies has shown that the synaptic processing and transmission may fall into two categories. In arbors such as CA3 or dentate gyrus all inputs cause more or less the same depolarization in the soma, independent on their origin. They name this feature as passive normalization. On the other hand, in morphologies like in CA1, the somatic effect of synapses is location dependent, with a strong decay with distance. It is known that active mechanisms can counteract this passive decay (postulated in (Anderson et al., 1987), evidence in (Jarsky et al., 2005; Nevian et al., 2007; Remy et al., 2009)).

1.3.2 Deep Learning

Deep learning has recently drawn attention as a set of tools to generalize the information of a data set. The underlying idea is analogous to the operation of the cortex, where the output of some areas project to others in a hierarquical process. Analogously, deep networks are built of several layers, in which the the outputs are the inputs of the higher layers. Each layer is composed of a set of neurons. As biological neurons, these neurons receive inputs. This input is a set of real numbers as opposed to synaptic input. They perform a linear operation with all this inputs and then perform a non-linear operation. The most typical operations are sigmoids and rectified linear units (linear if the result is greater than zero, zero otherwise). Figure 1.5 illustrates the flow of information in a deep network. Starting with the input (marked in blue), it is fed to the first hidden layer. There, a linear operation (matrix multiplication and bias addition) is performed,

and output is passed to a non-linear operation (relu in the figure). The resulting output is passed on to the successive layers until the final layer, the network output is reached.

Then the output is measured against a loss function and yields an error. The weights of the network are recalculated so as to minimize the resulting error. This procedure is analogous to plasticity and is repeated in an iterative process so that the final error is minimized. In order to know how the weights of all the network are adjusted to reduce the error, an optimizer is necessary. An optimizer is an algorithm that calculates the synaptic weight update needed to minimize the loss.

The most straightforward optimizer is to calculate the total error for the whole dataset and, as this error can be written analytically as a function of the weights, calculate its gradient with respect to all the parameters. The gradient then indicates the direction in which all parameters must change in order to reduce the error, and thus update them following the direction of the gradient. How much are the parameters updated? This is a hyperparameter given, denoted learning rate. Hyperparameters are those parameters in a deep learning model that deal with how to regulate the parameters of the model (weights and biases). The higher the learning rate, the more the weights are updated after each run. However, given that the error is a complex function depending on many parameters, updating too much from a single step may push the system away from the global solution. On the other hand, too small updates may go go in the right direction but the time taken for optimization might be too large. Thus, choosing the appropiate learning rate is problem-dependent.

The procedure described above is named gradient descent. To apply it, the full dataset needs to be passed through the network in order to calculate the gradient. This is not computationally efficient. It has been shown that choosing a subset of the full data and updating the weights more times is as reliable as with the full dataset, while being computationally much faster. This is denoted Stochastic Gradient Descent (SGD). SGD, however, does not work well with deep models for a number of reasons. The main one is that the parameters of the outermost layer depend solely on the error, and they can be well optimized. Nevertheless, the weights of the subsequent layers depend not only on the error, but also on the weights of the layers between the given layer and the output. Thus, the amount of error remaining to the deeper layers is decreasing. This is known as the vanishing gradient problem (Hochreiter, 1998). To overcome that, more sophisticated algorithms have been proposed in the recent years. For this study, I implemented two state of the art optimizers, Adam (Kingma and Ba, 2014) and Adadelta (Zeiler, 2012)

to train the artificial neural network.

1.4 Aims of the study

The following study has two main lines of research.

The first one is related to the propagation of synaptic currents from their input site, the dendrites towards the soma. To measure the conductances due to synaptic input in a patch clamp recording in the soma of neurons, I have developed a novel method based on the measurement of the time constant as a function of time. The method is based on the injection of a current of sinusoidal waveform and the application of the RC circuit properties to the neuron. Based on it, a readout of excitatory conductances can be made. Furthermore, as the synaptic conductance changes influence the time constant, which is the timescale in which the membrane potential changes, its effects on synaptic integration are explored. Finally, an extension of the method is applied to estimate excitatory and inhibitory conductances during sharp wave ripple oscillations.

Secondly, two experimental findings on the nature of AP initiation in CA1 pyramidal cells have been made in the lab of Prof. Dr. Andreas Draguhn . The first one is characterization of neurons whose axon emanates from a basal dendrite, and the enhanced efficacy of that input towards AP generation. The second one is the existence of a bimodal AP timing distribution for antidromic action potentials. Computational studies where carried out to provide support for those experiments and further study the underlying mechanisms of their synaptic propagation and action potential initiation.

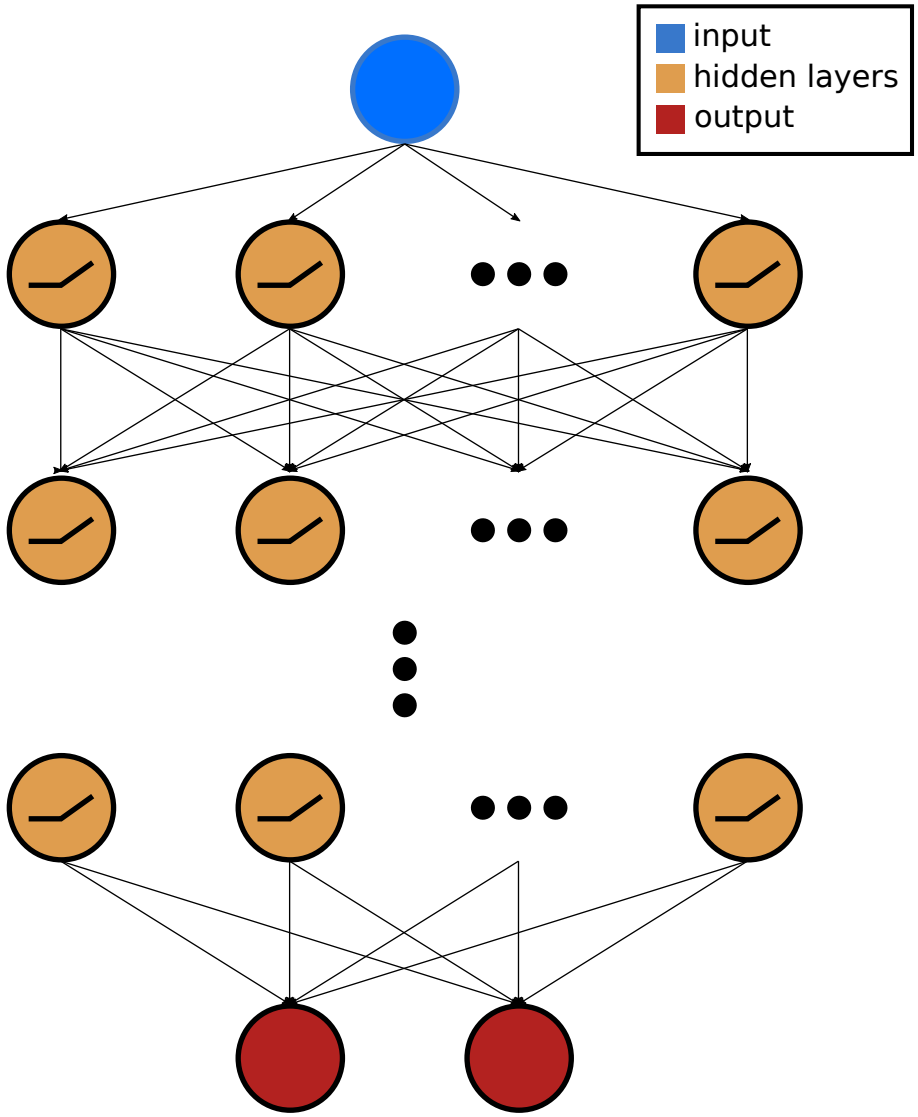

Figure 1.5: Schematic of general deep network. Inputs (blue) feed the first hidden layer of neurons (top row in brown). The inputs are multiplied by a weight matrix and a bias is added. The result is passed through a rectified linear operation and this output is the input of the following layer. Layers may contain several nodes and the network may have several layers (depicted as . . . in the figure). The information traverses the network forward until the output is reached (red). The output is fed to a loss function, and then is used to give feedback to the network on how the weights and biases should be updated to minimize the error in a backpropagating manner.

2 Materials and Methods

2.1 Experimental Procedures

All experimental procedures were performed in accordance with the regulations of the states of Baden-Württemberg and Nordrhein-Westfalen.

2.1.1 Preparation

Young adult (p21-28) male mice were used for the experiments. After being anesthetized with CO_2, they were beheaded and their head was kept in artificial cerebro spinal fluid (ACSF, see table 2.1). The brain was carefully removed from the cranium and the most rostral and caudal parts thereof were sectioned with a razor blade. After that, a thin slice of the dorsal part was sectioned to ensure a flat surface. Then, the remaining brain was set in a vibratome chamber VT1200S (Leica Camera AG, Wetzlar, Germany) . Horizontal slices of $300\mu m$ width were sectioned in the presence of sucrose ACSF (table 2.1). This sucrose ACSF contains low sodium and greater concentration of sucrose to avoid neuronal damage during slicing. After extraction, the slices were incubated for 30 minutes at 32^oC and for a further 60 minutes at room temperature.

2.1.2 Patch Clamp Recordings

Patch clamp is a technique developed in the 70s by Neher and Sakmann (Neher and Sakmann, 1976) to measure from a patch of membrane. By gently approximating a micropipette to the membrane and then applying a negative pressure, a patch of membrane is trapped in the pippete (gigaseal) and an electrode inside the pipette can record the channels inside it. The configuration used in the experiments was whole cell. In this configuration, the membrane is opened and the pipette has direct electrical contact to the inside of the neuron.

	ACSF	Sucrose ACSF
	[mM]	[mM]
$NaCl$	124	60
KCl	3	2.5
NaH_2PO_4	1.25	1.25
$CaCl_2$	1.6	1
$MgCl_2$	–	5
$MgSO_4$	1.8	–
$NaHCO_3$	26	–
Glucose	10	20
Sucrose	–	100

Table 2.1: Preparation recipes

	[mM]
potassium gluconate	140
KCl	3
$NaCl$	4
HEPES	10
EGTA	0.2
$MgATP$	2
Na_2GTP	0.1

Table 2.2: Intra solution recipe. pH was adjusted to 7.2 by addition of KOH.

Neurons were visually selected via confocal microscope (RIM Scope II, LaVision Biotec, Bielefeld, Germany) and then patched with pipettes obtained from GB200F glass tubes. The glass tubes were pulled with an DMZ universal puller (Zeitz Instruments, Martinsried, Germany) , and had input resistances between 2 and 6 $M\Omega$.

The patch pipette contained an intracellular solution (table 2.2). To visualize the neuron, 150μM Alexa 488 (Thermo Fisher Scientific, Waltham, USA) was added to the intracellular solution.

The signal was measured with an ELC03XS amplifier (npi electronic, Tamm, Germany) . In order to obtain the greatest voltage and current ranges, the amplifying factor was set to 50. Raw data was low pass filtered at 8 kHz.

Finally, raw data was acquired with Igor in its proprietary binary formats. The traces were read and further processed with custom made python tools.

In order to isolate the effect of AMPA synapses, NMDA-r were blocked with 30μM

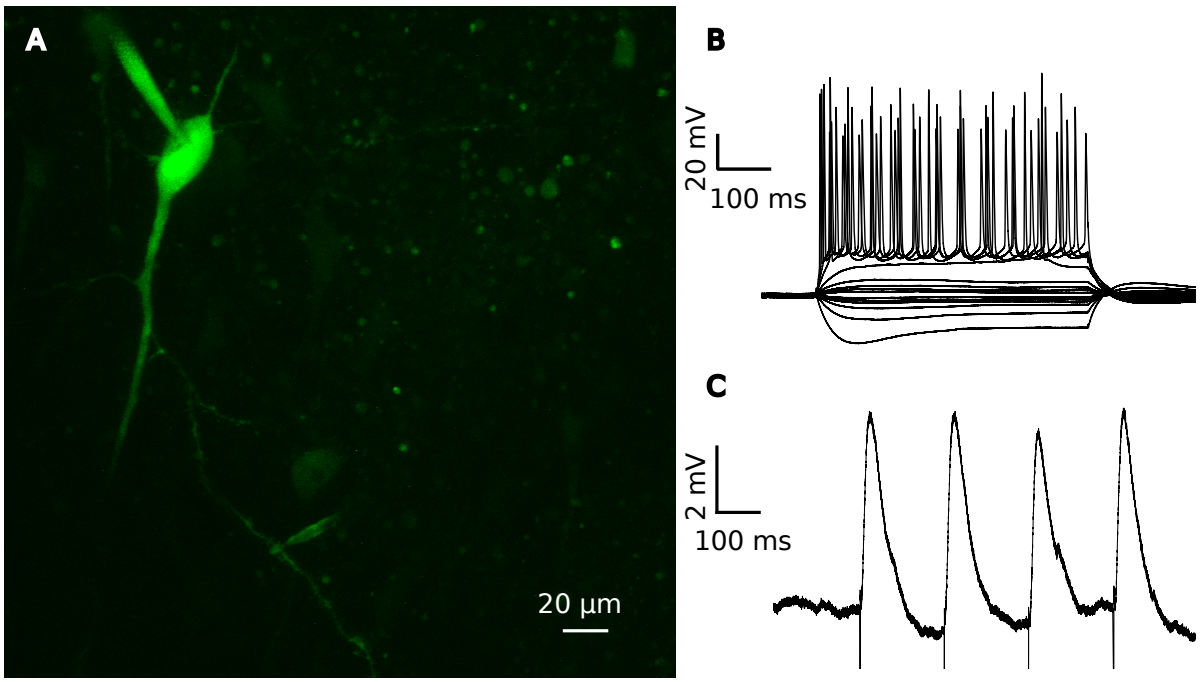

Figure 2.1: Overview of patch clamp experiment. (A): Maximum projection of z-stack of a patched CA1 pyramidal cell filled with Alexa 488 and and imaged with a two photon microscope. Iontophoresis pipette was placed nearby an apical dendrite. (B) Neuron's response to constant current injections. (C) Neuron's response to a train of iontophoretic stimulations.

AP5 (Häusser and Roth, 1997).

Synaptic events where triggered by iontophoresis (Müller and Remy, 2013). This technique consists of filling a pipette with glutamate and maintaining it inside the pipette by an electric field. Then, a short squared pulse of the opposite polarity releases the neurotransmitter with high spatio-temporal precision.

The iontophoresis pipettes (GB150-F (Science Products, Hofheim, Germany)) were pulled with a DMZ puller. In order to prevent glutamate spillage, the opening of the pipette needs to be smaller than the resolution of the 60x microscope. Thus, quality of the pipette needs to be assessed after the whole cell recording is established and the iontophoresis pipette is approximated to the neuron. If the baseline noise is incremented, there is glutamate spillage and the pipette is discarded.

The iontophoresis pipette was filled with a solution containing $150\mu M$ glutamic acid and its pH was adjusted to 7.2 with NaOH. Then, it was filled with $150\mu M$ Alexa 488 be visible with the two photon microscope.

The iontophoresis pipette was controlled by an MVCS-C-02 stimulator (npi electronic, Tamm, Germany) . This unit has an embedded capacity compensation circuit to ensure the application of square pulses despite the capacitive loss of the pipette. The amplitude of the pulses was tuned to ensure an EPSP waveform of around 5-10 mV amplitudes and a physiologically looking waveform.

2.1.3 Network oscillation recordings

Network oscillations were also recorded. These experiments, performed by Martin Kaiser in the lab of Prof. Dr. Andreas Draguhn . Acute slices were prepared as described above, with the difference of having a thickness of $450\mu m$. They were incubated for two hours in an interphase chamber and then the local field potential was recorded with an extracellular glass electrode (tip diameter $> 5\mu m$; filled with ACSF and acquired with an EXT-10-2F amplifier (npi electronic, Tamm, Germany) .

Additionally, intracellular recordings were measured in the vicinity of the extracellular electrode with SEC-05 LX amplifier (npi electronic, Tamm, Germany) in bridge mode. Data was acquired with Spike2 (CED, Cambridge, United Kingdom) and stored in its binary format. Data was further analyzed and processed using custom made python tools.

2.2 Computational Modeling

2.2.1 Theoretical model

To test the obtention of the instantaneous time constant in a simple, controllable environment, I created a single compartment passive neuron from the general membrane behavior.

All the equations on the theoretical model were solved using the ode module of scipy (Jones et al., 2001). They were solved using the Dormand-Prince method, which belongs to the Runge-Kutta family of fourth order. The time step for this theoretical model was set to $dt = 0.1ms$, which corresponds to a frequency of $10\,kHz$. Although this was smaller than the experimental sampling rate, it was more than an order of magnitude higher than the fastest process to occur in the cell (AMPA decay constant, $5ms$ (Spruston

parameter	value		description
g_l	0.01	μS	leakage conductance
c_m	0.2	nF	capacity
g_{in}	0.5	μS	axial conductance
E_l	-65	mV	leakage reversal potential
g_{syn}	0.005	μS	maximum synaptic conductance
τ_1	0.2	ms	synaptic rise time
τ_2	2	ms	synaptic decay time

Table 2.3: Theoretical model parameters

et al., 1995)). Furthermore, the absence of noise helps to keep the traces stable. The comprehensive parameter values are given in table 2.3.

Synapses were modeled with a double exponential (equation 2.1), where τ_1 and τ_2 are the rise and decay times, respectively, and K is a normalization constant so that $g_{syn,max}$ is the maximum conductance. This only applies for positive times. Otherwise, it is set to zero to avoid the exploding exponential.

$$g_{syn}(t) = g_{syn,max} \times K \times \left(e^{-t/\tau_2} - e^{-t/\tau 1}\right) \tag{2.1}$$

Two computational models of CA1 pyramidal cells were used for this study. The first one comes from a reconstructed CA1 pyramidal cell extensively used in the literature (Jarsky et al., 2005) and the second one is a simplified CA1 pyramidal cell designed by Dr. Alexei Egorov .

All simulations were carried out with the NEURON simulation environment (Hines and Moore, 1997; Carnevale and Hines, 2006). The NEURON version 7.4 was compiled from source and its python module was used ((Hines et al., 2009)) for simplicity of integration with further stages of analysis. Data coming from the simulations was processed and analyzed with tools from the scipy stack (Jones et al., 2001) trough custom-made applications. Finally, figures were designed and implemented with the matplotlib plotting library (Hunter, 2007). Most of the simulations where carried out in a Core i7 desktop computer with 16GB RAM.

The time step for the simulations was set to $dt = 0.01ms$. This time step is an order of magnitude higher than the theoretical model to allow higher precision in highly non linear calculations of the ionic channels. Although a variable time step might have been computationally more optimal, the duration of the simulations was not impractically

large (see below), and having a constant time step facilitated the implementation of trace-wide operation (i.e., calculating the derivative, or locating and comparing onsets or peaks of APs).

2.2.2 Computational model: Instantaneous time constant

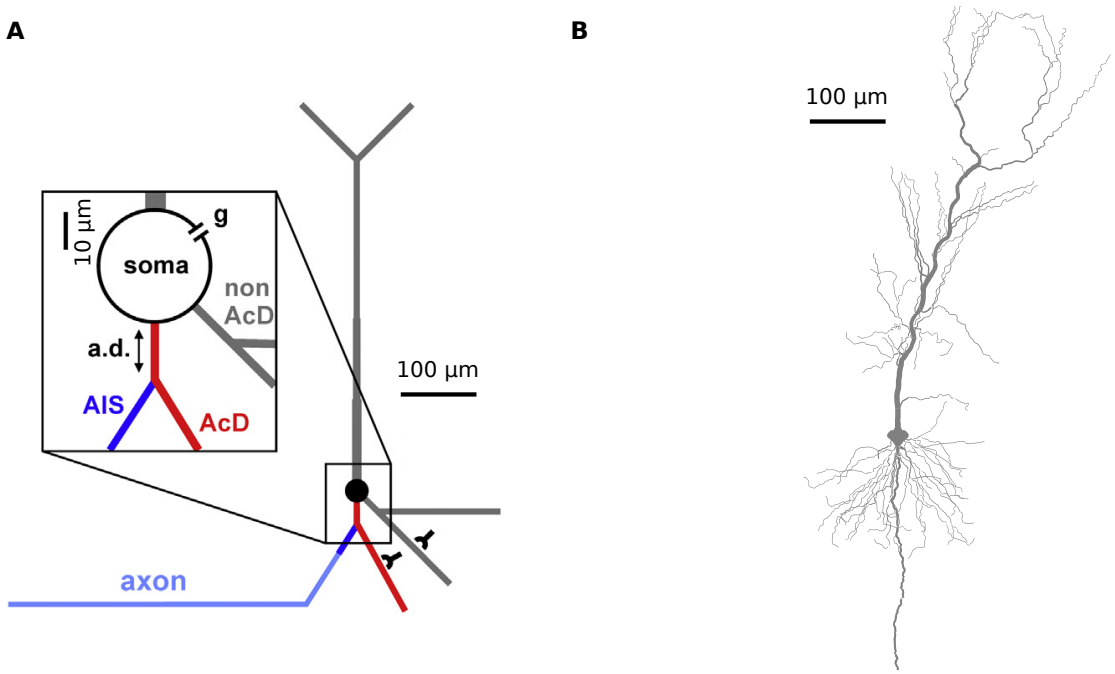

Figure 2.2: Schematic of computational cells. (A) Model of AcD cell (adapted from (Thome et al., 2014). (B) Model of the cell used in the instantaneous time constant and in the ectopic simulations adapted from (Jarsky et al., 2005).

Following from the theoretical single compartment model described above, a more complex model was needed to study the effects of post synaptic potential propagation and effects of active conductances of CA1 pyramidal cells.

Morphology and biophysics

The morphology used was the same as in (Jarsky et al., 2005). Regarding the biophysical tuning, the model mostly followed the parameters from the original model. This model consists of three types of ionic channels: the fast sodium channel, the delayed-rectifier potassium channel and the A-type potassium channel. The latter one has two variants,

the proximal and the distal . The distal one is only present in the apical dendrite and increases with the distance to the soma (Hoffman et al., 1997).

Sodium channel density was increased (to $0.24 S/cm^2$) in the AIS to ensure this is the AP onset site. As this model is able to produce dendritic spikes, sodium channels were reduced on the dendrites so as not to interfere with the passive propagation of EPSPs and add a further source of variability. Further, both the capacitance in the myelinated parts of the axon was reduced (from 0.75 to 0.04 $\mu F/cm^2$) to model the insulation of the myelin sheath. Comprehensive information about the biophysics is shown in table 2.5

Simulation settings

Excitatory synapses were implemented with a double exponential ($\tau_{rise} = 0.2ms$, $\tau_{decay} = 2ms$) and reversal potential of $0mV$. The peak conductance was $0.2nS$). The number of synapses was adjusted to have a peak EPSP amplitude in the absence of the sinusoidal of $5mV$ or, if that amplitude was not reached, 257 synapses. A sinusoidal current injection of $10Hz$ frequency and amplitude of $10pA$ was applied. The same synaptic input was elicited for 10 uniformly distributed phases. Further, for comparison, the soma was clamped to $-70mV$ and the same synaptic input was elicited in the absence of the sinusoidal current.

For the double input experiments, the same sinusoidal input was applied. A target apical dendrite was chosen and it received 20 synaptic inputs. Along this input, another input was chosen from the same dendrite, a nearby dendrite and an apical dendrite. The timing between both inputs was set between 0 and $10ms$ in a logarithmic scale.

2.2.3 Computational model: Axon carrying Dendrites

It has been shown (Thome et al., 2014) that in 50% of CA1 pyramidal cells, the axon stems out not from the soma but from a dendrite, the Axon carrying Dendrite (AcD). Therefore, a model to mimic this behavior was constructed.

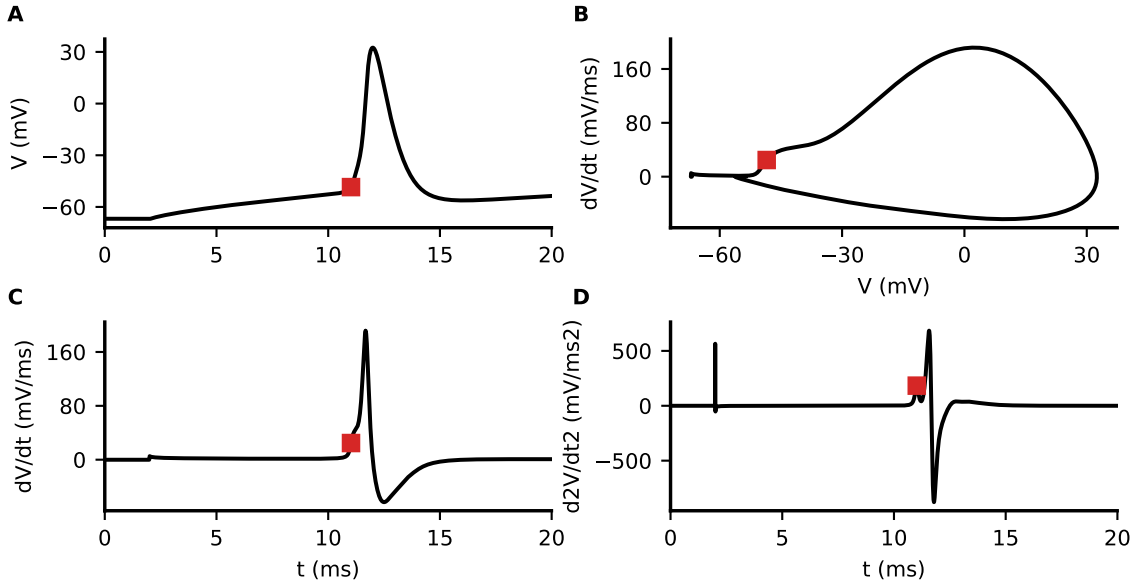

Figure 2.3: Calculation of AP threshold. In accordance to the experimental data, it was calculated as the first peak of the second derivative (D, red square). Compare the point with the membrane potential (A), phase plot (B) or first derivative (C).

Morphology and Biophysics

A simplified model of a CA1 pyramidal neuron was employed. It consists of a somatic compartment ($30\mu m$ diameter), a single apical dendrite ($400\mu m$ length, $2-4\mu m$ diameter) branching into two tuft dendrites ($150\mu m$ length, $2\mu m$ diameter) and two basal dendrites.

The first basal dendrite, AcD , has the axon stemming out of it at a variable distance, *axon distance*. The second, nonAcD, has the same morphology as the AcD and has a branching dendrite similar to the axon to keep the electrotonic symmetry between AcD and nonAcD.

On the basal area, there are two basal dendrites. The first one, the AcD ($150\mu m$ length, $1.4\mu m$ diameter), has the axon attached to it. The distance to the soma at which the axon is located is the main independent variable of this set of simulations and is denominated *axon distance*. As a control, there is another basal dendrite, the nonAcD, which has the same length and diameter as the AcD and acts as a control for synaptic inputs forced to be propagated through the soma. In order to ensure

electrotonic symmetry, the non AcD has a dendritic branch connected to it at the same distance as the axon, and whose length is ($100\mu m$).

The axon is divided into two compartments, the AIS ($33\mu m$ length, $1.22\mu m$ diameter), and the rest of the axon. ($500\mu m$ length, $1.2\mu m$ diameter).

The compartments are divided into segments for numeric integration of the equations. A typical segmentation is to make the length of the segments one order of magnitude smaller than the length constant of the compartments (Carnevale and Hines, 2006), which was used throughout most of the neuron. Still, this segmentation does not properly resolve high frequency events (i.e., the rise time of the synapse) (Carnevale and Hines, 2006). To avoid that, I set a segment size of $0.5\mu m$ on the $5\mu mu$ closest to the synaptic application site.

The biophysical properties were taken from (Cutsuridis et al., 2010; Hu et al., 2009). All used parameters are included in table 2.4. The most salient characteristics is that this model has an increased sodium channel density in the AIS, $0.5S/cm^2$, to ensure these unit to be the initiation site of the AP (Yu et al., 2008). Comprehensive details are given in table 2.4.

Excitatory synapses were modeled via 2 exponentials ($\tau_{rise} = 0.5ms$, $\tau_{decay} = 3ms$) and reversal potential of $0mV$. Low maximum conductance values were used ($5pS$) to allow for a continuum of inputs.

Simulation settings

In the first set of experiments, the axon start was set at distances from 0 to $15\mu m$ in steps of $0.5\mu m$. For each distance, the minimum input to elicit an AP was calculated. Inputs were AcD and nonAcD inputs at $50\mu m$ from the soma and constant current injection into the soma. For comparability, inputs appear normalized in the figures with respect to their values with no axon distance in the first experiment: 5149 synapses and $0.3735nA$. For all inputs, the threshold of AP initiation was calculated (figure 2.3) like in the experimental data (Thome et al., 2014). The threshold was defined as the first local maxima of the second derivative, which accounts for the maximum acceleration of the change of membrane potential.

To model the effects of the electrotonic distance, the axial resistance was reduced proportionally to the increase in the axon distance (Baranauskas et al., 2013). Perisomatic inhibition was implemented by increasing chloride conductance to account for 30% re-

	basal	soma	AIS	axon	radTprox	radTmed	radTdist	lm
$L(\mu m)$	150	30	33	500	100	100	200	150
diam (μm)	1.40	30.00	1.22	1.20	4.00	3.00	2.00	2.00
leak resistivity (Ωcm^2)	25000	25000	25000	25000	25000	25000	25000	25000
$C_m(\mu F/cm^2)$	1.0	1.1	1.0	1.0	1.0	1.0	1.0	1.0
$R_a(\Omega/cm)$	200	200	200	200	200	200	200	200
Na^+ conductance (S/cm^2)	0.0025	0.0500	0.5000	0.0700	0.0070	0.0070	0.0070	0.0070
delayed rectifier K^+ conductance (S/cm^2)	0.0009	0.0100	0.0200	0.0140	0.0009	0.0009	0.0009	0.0009
proximal A-type K^+ conductance (S/cm^2)	0.0256	0.0075	-	-	0.0150	-	-	-
distal A-type K^+ conductance (S/cm^2)	-	-	-	-	-	0.030	0.045	0.049
$K^+(Ca^{2+})$ sAHP conductance (S/cm^2)	0.0005	0.0005	-	-	0.0005	0.0005	0.0001	-
medium AHP K^+ (BGP) conductance (S/cm^2)	0.0330	0.0908	-	-	0.0330	0.0330	0.0041	-
M-type K^+ conductance (S/cm^2)	-	0.0012	0.0012	-	0.0012	-	-	-
HVA L-type Ca^{2+} conductance (S/cm^2)	0.00003	0.00070	-	-	0.00003	0.00316	0.00316	-
LVA T-type Ca^{2+} conductance (S/cm^2)	0.0010	0.0001	-	-	0.0001	0.0001	0.0002	-
HVAm R-type Ca^{2+} conductance (S/cm^2)	0.00003	0.00003	-	-	0.00003	0.00003	0.00006	-
I_h conductance (S/cm^2)	0.00002	0.00002	-	-	0.00005	0.00005	0.00020	0.00035

Table 2.4: Parameters used in AcD model.

duction of input resistance. A more distal location ($90\mu m$ from the soma) was chosen to elicit dendritic spikes. The inputs were normalized to the value of the AP experiments.

2.2.4 Computational model: Ectopic AP generation and propagation

Ectopic action potentials are action potentials whose origin is not somatic depolarization and thus, they lack the somatic predepolarization that usually precedes APs (Bähner et al., 2011). They are believed to be of axonic origin and gap junctions play a role on its generation (Vladimirov et al., 2013). This model is meant to study how synaptic input can affect the generation of AP at remote locations, not only in the AIS, but also in the middle of the axon, at the nodes of ranvier.

Morphology and Biophysics

As with the $\tau\star$ model, the reconstructed CA1 pyramidal neuron from the Spruston Lab (Jarsky et al., 2005) was adapted. Here, to fully study the mechanisms of AP propagation, we redesigned the axon to fit our experimental data. First, the AIS was set to have a length of $33\mu m$ (Thome et al., 2014). The AIS is followed by a piece of unmyelinated axon of $100\mu m$. After that, the myelinated part starts, with nodes of ranvier separated $100\mu m$ each, in accordance with experimental observations in the lab (Dr. Alexei Egorov , data not published). Axon diameter was set to $0.9\mu m$. This is in accordance with the literature and produced comparable node-soma propagation delays to our experimental data.

Excitatory synapses were designed as in section 2.2.2 and they were randomly applied to the oblique apical dendrites. Inhibitory synapses were used with reversal potential of $-75mV$. They were modeled with a double exponential ($\tau_{rise} = 2ms$ and $\tau_{decay} = 18ms$ and the maximum conductance was set to $0.2nS$.

Simulation settings

The alvear stimulation was simulated by a current between two points separated $75\mu m$, mimicking the two tips of the stimulation electrode in the experiments. This current generated distance dependent dipolar field and this field caused a depolarization in

	soma	apical	basal	AIS	non myelinated axon	myelinated axon	node
$r_m\,(\Omega cm^2)$	40000	40000	40000	40000	40000	40000	50
$c_m\,(\mu F/cm^2)$	.75	.75	.75	.75	.75	0.04	.75
$R_a\,(\Omega cm)$	200	200	200	200	200	200	200
$g_{Na}\,(S/cm^2)$	.04	0.004	0.004	0.24	0.04	0.0008	3
$g_{Kdr}\,(S/cm^2)$	0.04	0.04	0.04	0.04	0.04	0.04	0.04
$g_{Kap}\,(S/cm^2)$	0.048	0.048	0.048	0.048	0.048	0.096	0.096
$g_{Kad}\,(S/cm^2)$	-	0.048	-	-	-	-	-

Table 2.5: Parameters for $\tau\star$ and ectopic model

the membrane. The first simulations dealt with the characterization of that alvear stimulation and AP generation.

The second run of simulations consisted on taking a constant alvear stimulation strength $1pA$ for late spikes and $1.6pA$ for and run it against changes of input of biophysical parameters to see the transition from one kind of spike (early or late, see results) to the other. In that manner, somatic current injection, excitatory input, perisomatic inhibition and change of AIS sodium channel density were performed.

Finally, to quantify the modulation effect of synaptic or current injections, simulations were run in the absence of other input. Then, the minimum input necessary to make the transition between no AP and late spike or between late and early spike were calculated. This was used as the normalization constant for other inputs. Then, somatic current injection, or post synaptic potentials were applied, and the minimum input to ellicit the same transition was calculated.

3 Results

3.1 Theoretical derivation of the instantaneous time constant

‘

This chapter describes the theory by which the instantaneous time constant can be calculated and, from it, the kinetics and amplitude of excitatory synaptic inputs can be calculated.

3.1.1 Passive cell with excitatory input

As seen in section 1.2.1, the membrane can be described by an electric circuit composed of a capacitance in parallel with a resistor (figure 1.3 B). The behavior of an active element (i.e., synapse or ionic channel) can be model by another conductance in parallel to these two. This active conductance may be dependent on membrane potential or ionic concentration. Thus, in the case of an excitatory synapse, the equation becomes

$$c_m \frac{dV}{dt} = g_l(E_l - V) + g_{syn}(t)\,(E_{exc} - V) \tag{3.1}$$

here, E_{exc} stands for the reversal potential for excitatory synapses. As this is equal to $0mV$, it can be taken out of the equation. Here we can see three currents that must be balanced. The first one is the tonic leakage current ($g_l(E_l - V)$) that sets the resting membrane potential, the second is the synaptic current, whose reversal potential is zero ($g_{syn}(t)\,(E_{exc} - V)$). Finally, the capacitive current ($c_m \frac{dV}{dt}$) accounts for the movement of ions that the other two cause. Without synaptic conductances, the time constant was immediate ($\tau = c_m/g_l$). Now let us find the analog of the time constant in the presence of a time varying excitatory conductance. If we combine together both the leakage and

Magnitude	Typical units	Description
c_m	nF	membrane capacity
E	mV	electric resting potential
RT	J/mol	thermal energy
F	C	charge of one mol
I/i	nA	transmembrane current
g_l	μS	leakage conductance
V	mV	membrane potential
E_l	mV	leakage reversal potential
λ	μm	length constant
g_{in}	μS	axial conductance
g_{syn}	μS	maximum synaptic conductance
τ	ms	time constant

Table 3.1: Magnitudes described in the introduction

the synaptic current to make it resemble equation-1.6, we have

$$\frac{dV}{dt} = \frac{E_l \times \frac{\tau\star}{\tau} - V}{\tau\star} \tag{3.2}$$

where

$$\tau\star = \frac{\tau}{1 + g_{syn}(t)\,/g_l} \tag{3.3}$$

is the instantaneous time constant. At any time point, the membrane has a time constant that depends of the conductance state at that very instant. This time constant depends not only on the resting properties of the membrane ($c_m$and g_l) but also on the opening of the synaptic receptors.

When there is no synaptic input, $g_{syn}(t) = 0$, there is no influence of transient conductances on the instantaneous time constant and thus $\tau\star$ equals τ. Equation 3.2 becomes equation 1.6. On the other hand, when there is synaptic input, there is a positive value of $g_{syn}(t)$. As this conductance is in the denominator of the definition of the instantaneous time constant, the value of $\tau\star$ decreases. This decrease has two consequences in the equation. Firstly, the target potential (towards which the membrane potential is evolving, i.e., $E_l\tau\star\ /\tau$) is not E_l but tends towards the synaptic reversal potential, 0 mV. This target potential is closer to $0mV$ the greater the synaptic input. Secondly, the characteristic time at which this process occurs is now given by $\tau\star$. This

means that the activation of synaptic input not only changes the target equilibrium value of the membrane potential but also, as the time constant of the membrane has been reduced, it evolves faster towards this target potential.

As the relationship between $\tau\star$ and $g_{syn}(t)$ is straightforward (equation 3.3), if we can measure $\tau\star$ as a function of time during depolarization due to synaptic input, we could determine $g_{syn}(t)$ without the obligation of fixing a neuron to a holding potential, and measuring the current, like in voltage clamp recordings. This has the difficulty that synaptic conductances have a small decay constant (for example $\sim 5\,ms$ for AMPA (Spruston et al., 1995)) in comparison with the time constant of the neuron ($\sim 30\,mV$ (Wheeler et al., 2015)). Therefore, if tried to determine the instantaneuous effects of synapses to the time constant, they will be blurred by the slower dynamics of the resting state membrane time constant (Borg-Graham et al., 1998; Häusser and Roth, 1997).

We have seen that the membrane has a capacitive current, a leakage current and a synaptic current. We can also add fourth current to the equation. This current can have the meaning of a current coming from a nearby location in the neuron (see in the introduction) or from a patch pipette in current clamp. The equation-3.4 has now a more general view and can be used to calculate the instantaneous time constant

$$c_m \frac{dV}{dt} = g_l(E_l - V) + g_{syn}(t)\,(E_{exc} - V) + I_{inj} \tag{3.4}$$

3.1.2 Determination of the instantaneous time constant

The question that arises is how we can calculate the instantaneous time constant (and, thus, the excitatory conductance) from equation-3.2. The first step is to rearrange equation 3.4 so that it includes the instantaneous time constant:

$$\frac{dV}{dt} = \frac{E_l}{\tau} + \frac{I}{c_m} - \frac{V}{\tau\star} \tag{3.5}$$

here, we have two magnitudes that can be obtained directly from an experimental recording: The membrane potential, V, and the injected current, I. The derivative of the membrane potential, $\frac{dV}{dt}$ can, in turn, be obtained indirectly from V. In addition, there are three parameters, namely $\frac{E_l}{\tau}$, c_m and $\tau\star$. The first one, E_l/τ includes the leakage reversal potential and the time constant and the second, c_m, is the capacitance of the neuron. Together, these parameters represent the static components of the membrane

equation and are not expected to change throughout the recording. The third one is the instantaneous time constant, $\tau\star$, and, in contrast to the previous ones, it is dependent on time. From equation 3.3, the change of excitatory conductance can be inferred from the change in $\tau\star$.

From equation 3.5, the parameters (E_l/τ, c_m, $\tau\star$) could be obtained from the recorded magnitudes, (I, V, $\frac{dV}{dt}$). As both the recorded magnitudes and the instantaneous time constant are time dependent, it must be applied independently to each time point. Thus, we have three unknowns for three known values and this yields no algebraically unique solution. A further refinement is that knowing that the two first values ($E_l/\tau$and c_m) are common to all time points, we could try to solve them all simultaneously. In this case, for N_t time points (the whole recording), we would have $N_t + 2$ values to calculate, and N_t equations. Again, this case yields no unique solution.

In summary, the problem is that more information is needed per time point than what we currently have. The solution is to make several recordings with a small perturbation added. This perturbation needs to provide some variability to the recordings so that it enables to determine the parameters from equation 3.5 but it remains subtle enough so we can still assume that the physiological state remains the same across trials (the receptors behave the same way).

The first possible solution would be to have several recordings of the same event. Sadly, those recordings alone would provide essentially the same information (albeit recording noise), and thus would be useless. Therefore, some kind of perturbation is to be added in a way that changes the values of our recording measurements (I, V, $\frac{dV}{dt}$) to ensure enough variability to have several different equations that can be simultaneously solved and still subtle enough so that every trial can be considered equivalent to the rest (i.e., neglect effects of openness of voltage gated ion channels or recording noise).

The simplest perturbation would be to add small current steps ΔI for every trial, which by Ohm's law would shift the resting membrane potential From this point, we could then estimate the conducting changes by recording several synaptic events with different current injections and calculating the slope of the $I - V$ curves for every time point. Despite its theoretical feasibility, this approach has three main drawbacks. First of all, we can see from 3.6 that the current step makes no change in derivative of the membrane potential. As all $\frac{dV}{dt}$ are the same for every trial, we are disregarding one third of the total information we can have. Secondly, in an experimental setting, we need to account for recording noise, thus, we may only have current steps that ostensibly make

changes greater that this noise. Finally, if we are to reliably estimate the conductance, we would need a higher number of points in the $I - V$. As this can only be achieved by going further away from the starting point, at some point our assumption that our recordings were in the same electrophysiological state will hold no more. A similar approach has been tried (Borg-Graham et al., 1998) (see discussion).

Instead, a dynamic perturbation is preferred. This allows to remain within a small membrane potential range, as well as using the full variability of the derivative of the membrane potential. From circuit theory, it is known that dynamic perturbations lead to transient states that are difficult to solve or track analytically. There is however one exception: periodic signals. When a linear system (and we assume the neuron to be such) is perturbed with a periodic signal, there is a decaying transient state (in this case, its amplitude decays with the time constant of the neuron) plus a static/equilibrium state which oscillates with the same frequency as the input signal.

From fourier analysis, it is known that every periodic signal can be decomposed as a sum of sinusoidals of the same frequency (main one) and its multiples. For simplicity, let us choose a pure sinusoidal wave as the injection current, in exponential notation $I = I_0 e^{\imath\omega t 1}$, where ω is the angular frequency ($\omega = 2\pi f$). Then, the transformation results in

$$I = I_0 + I_{amp} e^{\imath\omega t} \tag{3.6}$$

$$V = V_0 + V_{amp} e^{\imath\omega t + \phi} \tag{3.7}$$

$$\frac{dV}{dt} = \imath\omega V_{amp} e^{\imath\omega t + \phi} \tag{3.8}$$

$$\tag{3.9}$$

the phase shift between the current and the membrane potential is due to the impedance of the membrane. This impedance depends both on the capacitance and the conductance of the membrane and can be summarized by

$$tan\phi = -\omega\tau \tag{3.10}$$

where the minus sign means that the membrane potential is delayed with respect to the

[1] in exponential notation, sine, cosine and exponential by $e^{\imath x} = \cos(x) + \imath \sin(x)$

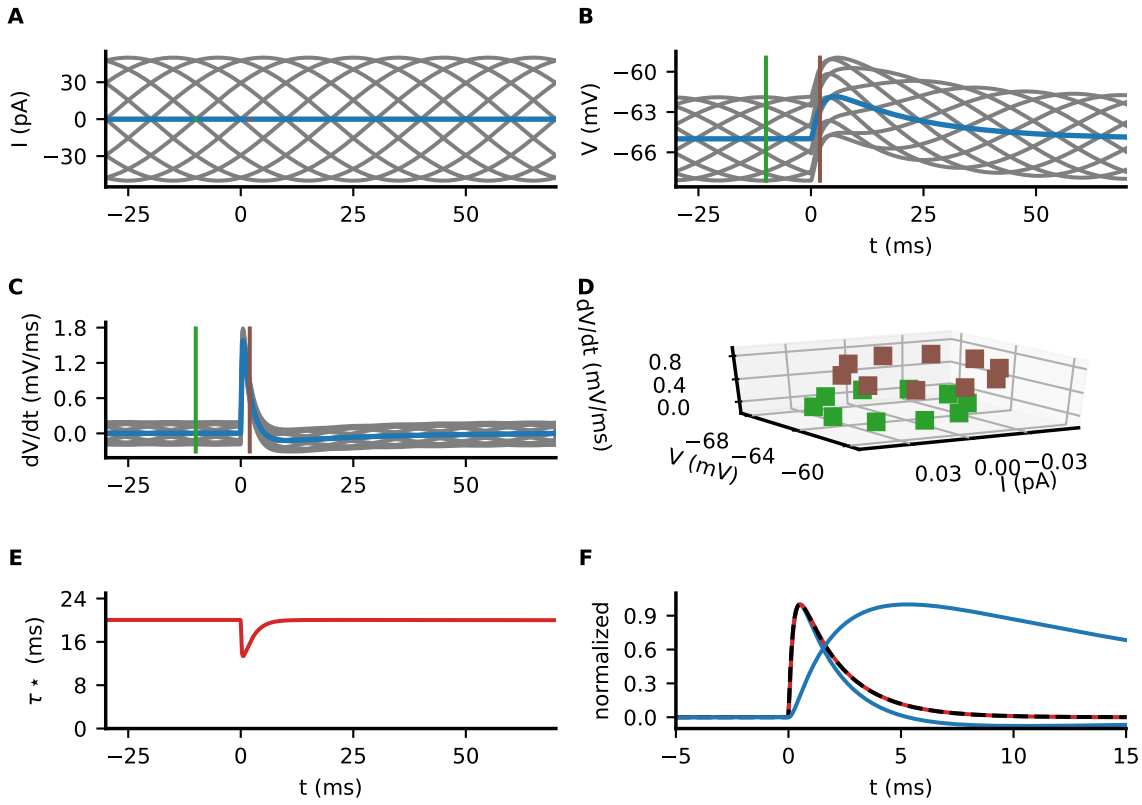

Figure 3.1: Calculation of $\tau\star$ on a model cell. (A) Multiple sinusoidal current injections (grey) and average (blue). (B) Membrane potential response to current injection and EPSP (each trial in grey, average in blue). (C) Derivative of membrane potential in (B). (D) I-V-dV/dt phase space of two trials (vertical bars in A-C). (E) Calculated $\tau\star$ using the procedure described in the text. (F) Normalized waveforms of V, dV/dt, $\tau\star$ and $g_{syn}(t)$.

current. This phase shift is a well known result from circuit theory and electrophysiology and can be also used to estimate the time constant of a membrane (Van Oosterom et al., 1979). More generally, the ratio between V_{amp} and I_{amp} is given by the full impedance

$$\frac{V_{amp}}{I_{amp}} = \frac{1/g_l}{1 + \imath\omega\tau} \tag{3.11}$$

which is the low pass filter representation of the membrane. The low pass filtering already suggests to avoid high frequencies in our injection current, as the denominator of the impedance will be big and thus the membrane potential response to the injected

current will be smaller.

Another advantage of using a sinusoidal current is that phases are uniformly distributed, their average is zero. In this way, we may record the trials with the sinusoidal perturbation to further apply our analysis, and then average them out to remove this oscillatory part.

In summary, we have chosen to inject a sinusoidal current (figure 3.1 A) via our patch pipette. The amplitude of this perturbation is small to avoid a change in the electrotonic state of the neuron. This procedure is repeated several times with the phase of the sinusoidal with respect to the synaptic input being shifted. In this manner, the sinusoidal oscillation. The voltage response to the combined oscillation and synaptic input has the shape of an EPSP distorted by the sinusoidal oscillation (figure 3.1 B). Due to the uniform distribution of the phases, averaging the trials removes the oscillatory component and yields the EPSP waveform (blue trace in figure 3.1 B). Moreover, the derivative of the membrane potential also has the oscillatory component of the sinusoidal plus a part that accounts for the conductance change (figure 3.1 C).

To obtain the instantaneous time constant out of this dataset, each time point is analyzed separately. For each time point, each trial has different values of membrane potential, injected current and derivative due to the shift in phase. A time point represented in the phase plane (I, V, $\frac{dV}{dt}$) forms an ellipse (figure 3.1 D). The inclination of this plane is given by the parameters (E_l/τ, c_m, $\tau\star$).

In order to obtain the values for $\tau\star$, and the static parameters, we apply a minimization to equation-3.5. As this equation is linear on all parameters, we can apply linear least squares. Moreover, given that two of the parameters, E_l/τ and $1/c_m$, are independent of time, we can use the same value for them throughout the whole time window. Thus, the quantity to be minimized is shown in equation-3.12, where i stands for trials of different phase, and j refers to the time points. In our case, $c_j = -1/\tau\star_j$ is the parameter we are most interested in, and $a = E_l/\tau$ and $b = 1/c_m$.

$$S^2 = \sum_{ij} \left(\frac{dV}{dt}_{ij} - a - bI_{ij} - c_j V_{ij} \right)^2 \tag{3.12}$$

Using this linear fit, a value for the instantaneous time constant can be recovered for each time point (figure 3.1 D). Let us carefully examine the evolution of $\tau\star$ for our excitatory input model (figure 3.1 E. Prior to the onset of the synaptic input, the

instantaneous time constant is equal to the resting state time constant, namely the 20 ms that were given a priori for this parameter. Furthermore, at the onset of synaptic input, the value of the instantaneous time constant is reduced, indicating that there has been a conductance increase. After the peak is reached, $\tau\star$ decays back to its resting state value, i.e., the normal time constant. As the relationship between $\tau\star$ and $g_{syn}(t)$ is known and straightforward (eq-3.3), we obtain the waveform of the synaptic receptor opening, which is a perfect correspondence to the synaptic kinetics given a priori (figure 3.1 F).

Furthermore, with this framework, one insight of the passive properties becomes clear. Excitatory synaptic input is not only causing a depolarization, but also changing the time constant that the neuron has exactly when the conductance is active. In the case of inhibitory input, the non-linearity of shunting is well known (Rall, 1967; Dingledine and Langmoen, 1980). In this case, the opposite feature is produced, that the change in time constant comes along with the change of the effective reversal potential, and thus it helps to integrate the signal towards more depolarized values.

In conclusion, I have here derived a new magnitude, the instantaneous time constant, $\tau\star$, which is a function of the total and time dependent conductance of the neuron. It is related to the time-relaxing dynamics of the membrane and thus through sinusoidal perturbations upon the neuron, we can obtain a readout of its excitatory conductance change.

3.1.3 Extension to inhibitory synaptic input

After the application of the instantaneous time constant to measure excitatory conductances, the next immediate question is whether this approach can also be used analogously to calculate inhibitory conductances along with excitation. Adding an inhibitory current to equation 3.4 yields

$$c_m \frac{dV}{dt} = g_l(E_l - V) + g_{exc}(t)\,(E_{exc} - V) + g_{inh}(t)\,(E_{inh} - V) + I \tag{3.13}$$

as before, $E_l$is the resting membrane potential (or close to it), around $-60mV$ and $E_{exc}$is the excitatory synaptic reversal potential, $\sim 0mV$. As opposed to excitation, the inhibitory reversal potential is rather close to the resting membrane potential ($\sim -70mV$), mostly due to the chloride reveral potential (Huguenard and Alger, 1986).

Here, $g_{exc}(t)$ and $g_{inh}(t)$ stand for the synaptic conductances for excitation and inhibition and are time dependent. Rewriting the former equation as is 3.3, we have

$$\frac{dV}{dt} = \frac{E_l + \hat{g}_{exc}(t)\, E_{exc} + \hat{g}_{inh}(t)\, E_{inh}}{\tau} - \frac{V}{\tau\star} + \frac{I}{c_m} \tag{3.14}$$

where here $\hat{g}_{exc}(t) = g_{exc}(t)\,/g_l$, $\hat{g}_{inh}(t) = g_{inh}(t)\,/g_l$ and now $\tau\star$ includes also the inhibitory contribution:

$$\tau\star = \frac{\tau}{1 + \hat{g}_{exc}(t) + \hat{g}_{inh}(t)} \tag{3.15}$$

here we see that the target potential towards which the membrane potential evolves (at rate $\tau\star$) is bound between $E_{exc}$and the minimum of $E_l$and E_{inh}. It can be that an increase in inhibition severely reduces the value of $\tau\star$, yet maintaining the target potential close to E_l. This phenomenon is already well studied and denominated inhibitory shunting (Rall, 1967; Dingledine and Langmoen, 1980). This means that, as opposed to the excitatory-only case, here the instantaneous time constant accounts for information regarding excitation and inhibition and is thus not possible to disentangle it.

Nevertheless, we can still use apply the same procedure of sinusoidal current injection as a readout of conductance, both for excitation and inhibition. In this case, we have 4 static parameters, namely E_l/τ, c_m, $E_{exc}$and E_{inh}, and two dynamic parameters, $g_{inh}(t)$ and $\hat{g}_{exc}(t)$. The equation to be fit is now of the form

$$\frac{dV}{dt} = \frac{E_l}{\tau} + \hat{g}_{exc}(t)\,\frac{E_{exc}}{\tau} + \hat{g}_{inh}(t)\,\frac{E_{inh}}{\tau} - (1 + \hat{g}_{exc}(t) + \hat{g}_{inh}(t)\,)\frac{V}{\tau} + \frac{I}{c_m} \tag{3.16}$$

and the value of $\tau\star$ is obtained indirectly from its definition (eq-3.15. Two practical problems, however, arise. First, there are parameters that are multiplied in the equation (conductance times reversal potential). As the equation is not anymore linear on its parameters, the least squares procedure applied in the last section is no longer applicable. Second, for the excitation-only case, there were two driving forces, towards excitation and resting potential. Now, there are three driving forces competing against each other, two of them ($E_l$and E_{inh}) close to one another, which makes attempts to fit it more

complicated as it will be difficult to distinguish these two close driving forces.

$$\frac{dV}{dt}\,\tau = \frac{I}{gl} + (V - E_l) + \hat{g}_{exc}(t)\,(V - E_{exc}) + \hat{g}_{inh}(t)\,(V - E_{inh}) \tag{3.17}$$

To overcome this difficulty and estimate the excitatory and inhibitory components when acting simultaneously (i.e., network oscillations), a deep learning fitting was designed. The aim is to determine the underlying average conductances during sharp wave ripples that would respond to the passive model with excitation and inhibition (equation 3.16, see theory). For that, the deep network was designed as in figure 3.2.

The input of the system is the time course of the sharp wave and the output is the parameters of the model. There are three subsets of parameters to be determined: the general passive properties, g_l, $E_l$and c_m; the reversal potentials for excitation and inhibition, $E_{exc}$and E_{inh}, and the conductances $g_{exc}(t)$, $g_{inh}(t)$. As the first two subsets are not expected to change during the course of the recording, the input of that part of the network does not depend on time. Moreover, as this parameters do not have a time dependence, the network here was simplified (two layers of 20 nodes each). On the other hand, solving for the conductances required a more complex network (10 layers, 100 nodes each layer). The output of the network was plugged into equation 3.16 along with the measured quantities ($I, V, \frac{dV}{dt}$) and its error was backpropagated to the weights and biases of the network.

Two more considerations are important. The system has a tendency to the trivial solution (all parameters are equal to zero, and thus the total error is zero). To avoid that, estimates of the passive parameters where calculated from the linear model outside the sharp wave and were added as an auxiliary loss. Also, a third loss was added making the reversal potential tend to $0mV$ for excitation and $-90mV$ for inhibition. The loss for the reversal potential was 10% the weight of the other two. The final consideration is that, as the recordings were too noisy, measurement errors outside from the sharp wave were disturbing the artificial neural network. To overcome that, the loss was weighted with a contrast like function ($(1 - t^2)/(1 + t^2)$), so that the values closer to the center of the sharp wave would contribute more to the minimization than those away from the ripple.

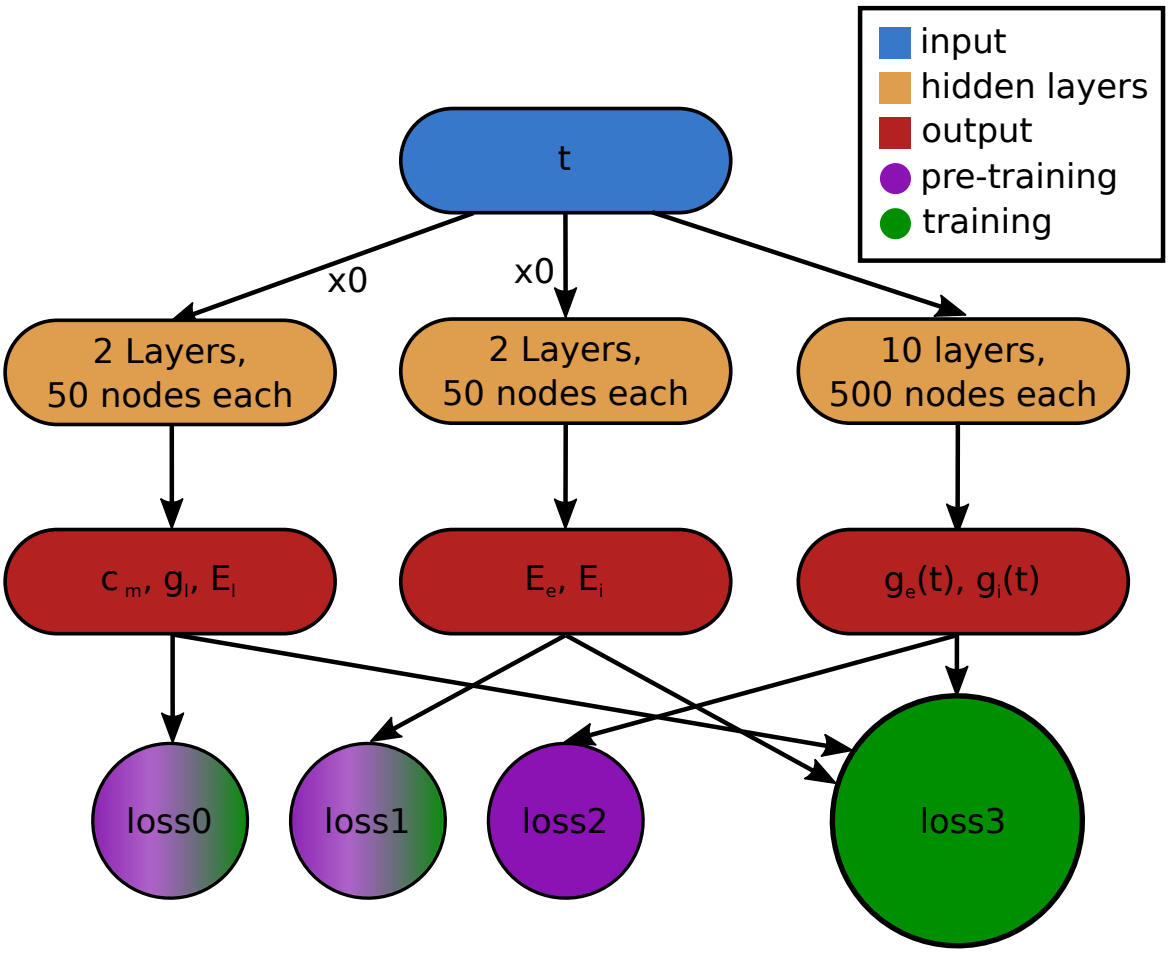

Figure 3.2: Schematic of the architecture chosen to estimated conductances. Input is the normalized time (blue). The network is divided in three deep columns. The first two yield the two sets of non time dependent parameters (passive parameters and reversal potentials). They are composed of two layers of 50 nodes with a relu output. The third one has 10 layers of 100 nodes each and will determine the time dependent conductances. A step of pre-training is performed adjusting the passive parameters and reversal potentials to estimates (violet losses). After pre-training is done, these losses are kept to ensure the system abides within physiological values and equation 3.16 is added to determine the conductances

3.2 Use of $\tau\star$ to estimate excitatory synaptic input

In the previous section, I demonstrated that the instantaneous time constant can be used to estimate the excitatory conductance change in a theoretical passive single compartmental model. The next question is whether this formalism can be applied in a more realistic context, such as a physiological neuron onto which synaptic input is applied. To that aim, patch clamp recordings of CA1 pyramidal neurons where carried out. Afterwards, computational simulations of a reconstructed CA1 pyramidal neuron are perform to study to which extent this method is valid.

3.2.1 Single stimulus, glutamate iontophoresis

The first effort was to repeat the analysis of the instantaneous time constant in physiological neurons. Traces were recorded from 12 CA1 pyramidal cells from acute slices of hippocampal mice. The cells where patched and filled with Alexa 488 for locating the dendritic arbor. After the neuron was filled, an iontophoretic pipette was placed next to an apical dendrite to elicit glutamate pulses of $50\mu s$ width that produced excitatory post synaptic potentials. As with the theoretical approach, a sinusoidal current injection of $10Hz$ was provided by the patch pipette. Its amplitude was adjusted at the beginning of the experiment to ensure an oscillation of $\sim 2mV$ amplitude in membrane potential 3.4 B). 40 trials were recorded in two rounds of 20 uniformly distributed stimulations along the oscillation cycle (5 ms delay applied or, equivalently, 18 degrees within the 10 Hz stimulation).

Trial selection

The membrane potential recordings (figure 3.3 A) contain four different components. Firstly, a baseline given by the resting membrane potential of the neuron and the subsequent average current injection. Secondly a 10 Hz sinusoidal signal due to the oscillatory part of the injected current. On top on these two, an EPSP waveform triggered by the glutamate release. Due to the stochastic nature of the synaptic receptors, there is variability between trials and different EPSP waveforms. Finally, there is a recording noise component.

In order to ensure that only the most suitable trials are passed on the analysis, quality criteria must be taken. Regarding the stability of the baseline, it is customary to set

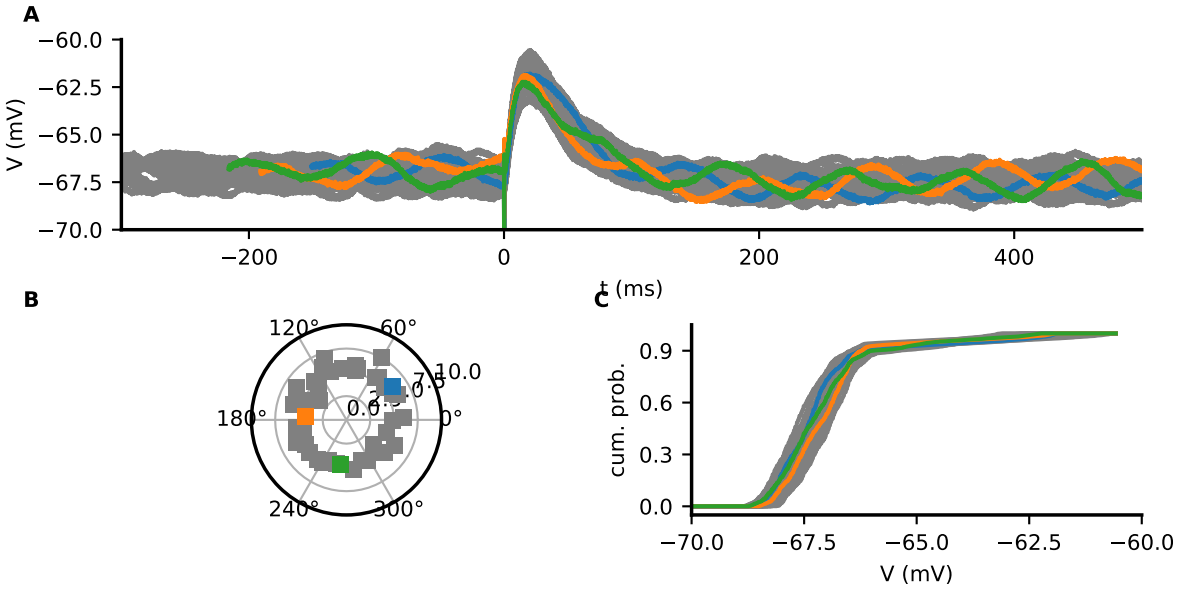

Figure 3.3: Trial selection for $\tau\star$. (A): Raw data of EPSP with sinusoidal current injections of different phases (grey lines, sample traces marked in colors). (B) EPSP amplitude is not dependent on phase. (C) Cumulative distribution of membrane potentials shows elements to discard.

a variance threshold on the baseline . Here, as the oscillatory component cannot be detached from the signal, the oscillation will overestimate the threshold and thus include trials with poor baseline. To overcome this difficulty, the stability of the baseline was assessed with the aid of the cumulative membrane potential distribution (figure 3.3 C). From this cumulative distribution we can see the that the lowest values correspond to extreme events (i.e., stimulation artifacts). After that, a steady part comes, where around 90% of the data points abide in a 3-4 mV region (oscillation of the sinusoidal, plus noise). This is where the baseline is, along with the sinusoidal oscillation. The remaining part (10% of the data points, and the most depolarized potentials) is where the EPSPs come into place. Based of this distribution, we can discern and quantify extreme events to discard them from the analysis, such as unstable baseline (red trace, figure 3.3) or extreme EPSP amplitude (pink trace). Quantitatively, the criteria where set to 3 median absolute deviations (MAD) for baseline and for amplitudes. After these quality criteria, the trimmed dataset was not severely diminished (range from 61% to 90% of accepted trials). i

Does the phase of the oscillation with respect to the onset of the synapses have an

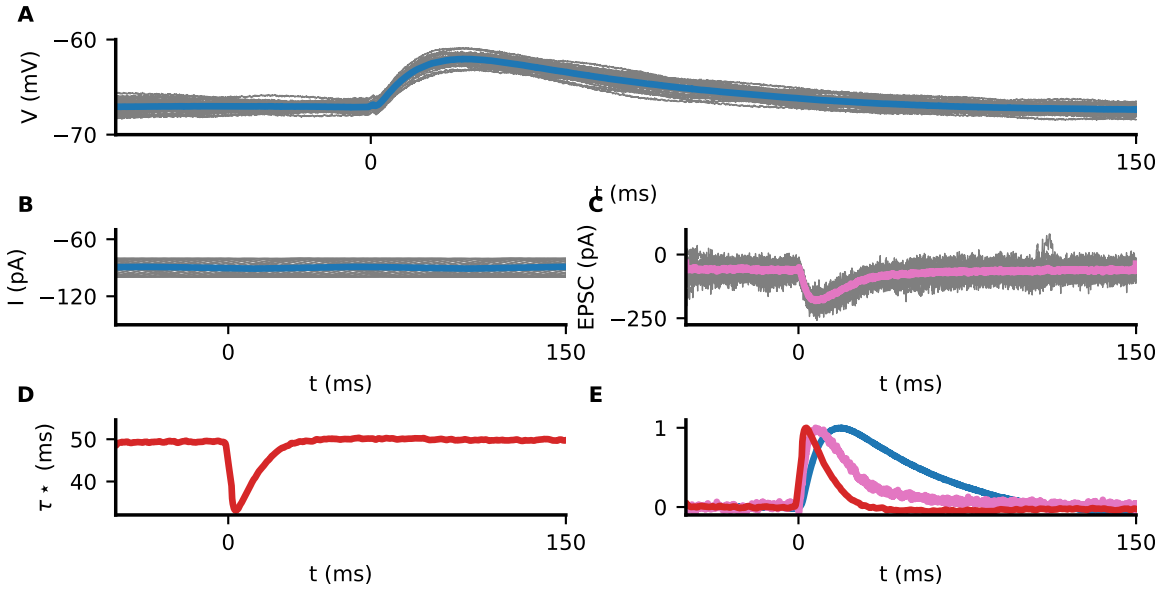

Figure 3.4: Experimental calculation of $\tau\star$. (A) Raw recordings (grey lines) and average (blue). (B) Sinusoidal current injection at each trial (grey lines) and average (blue). (C) Another experiment recording of EPSCs from the same cell (grey lines) and average (pink). (D) Calculated waveform of $\tau\star$. (E) Normalized waveforms of membrane potential (blue), EPSC (pink) and $\tau\star$ (red).

influence on the EPSP amplitude? The average amplitude and phase $EPSP \times e^{\imath\phi}$ did not significantly differ from the shuffled data (10000 iterations, 5% confidence interval, figure 3.3 B) suggesting the the phase of the oscillation and, thus, different states of voltage gated active channels did not affect the EPSP amplitude.

$\tau\star$ via the linear model

The traces portrayed in figure 3.3 A also include a stimulation artifact. As this stimulation disturbs the calculation of $\tau\star$ near the onset of the EPSP waveform, it was removed by linear interpolation of the membrane potential in a window of $0.55ms$ from the stimulation point (figure 3.4 A). Moreover, this removal also improved the quality of the derivative calculated by a variational method (Chartrand, 2011a).

This membrane potential recordings (figure 3.4 A), along the injected current (figure 3.4) and the derivative (not depicted) are used to calculate the values of the instantaneous time constant (figure 3.4 D). The calculated signal has two identifiable parts: baseline and waveform. According to the theoretical derivation (see section 3), the baseline is

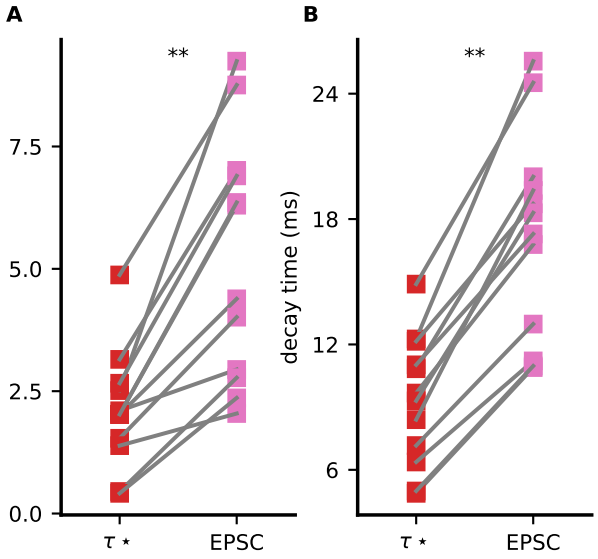

Figure 3.5: Comparison of magnitudes of $\tau\star$. (A): Synaptic rise time from $\tau\star$ (red) and EPSC (pink). (B): Synaptic decay time from $\tau\star$ (red) and EPSC (pink).

the calculated part in the absence of synaptic input and represents the value of the biophysical time constant. No significant differences where found between the time constant measured as the baseline of $\tau\star$ and by the kinetics of square pulse injections.

Secondly, the waveform corresponds to the kinetics of the synaptic conductance change. After the stimulation (time 0 in figure 3.4 D), the waveform of $\tau\star$ has a decrease of the value of the instantaneous time constant. This decrease corresponds to the increase in overall conductance due to the opening of the synaptic receptors. After the peak conductance is reached, the receptors close and thus the instantaneous time constant decays back to the default value, in the absence of synaptic conductances.

As opposed to the theoretical calculations, in the experimental setting is impossible to know the exact conductance change due to synaptic input. As a comparison, I also recorded excitatory post synaptic currents (EPSCs) from the same neuron in voltage clamp and without a sinusoidal current (figure 3.4 C).

Comparing the waveforms of EPSPs, EPSCs and $\tau\star$ (figure 3.4 E), we can see that the rising phase of the EPSPs concurs with the phases of highest value of both the EPSCs and $\tau\star$, suggesting that both are showing the activity of the excitatory driving force. The kinetics of the of $\tau\star$ seems faster as the kinetics of EPSCs. Indeed, rise times

(figure 3.5 A) and decay times (figure 3.5 B) where significantly faster in the case of $\tau\star$, suggesting the effect of space clamp is reduced for the instantaneous time constant with respect to excitatory post synaptic currents.

3.2.2 Computational Characterization

It was seen in the previous section that the instantaneous time constant can calculate the waveform of excitatory synaptic input with faster kinetics than EPSCs. The next question is to what extent this calculation is affected by space clamp. To this aim, a computational model was built.

The computational model combines some of the advantages of the theoretical and the patch clamp approach. As with the patch clamp, a complex morphology, and active conductances are present. As in the theoretical model, all synaptic inputs can be set a priori a repeated with the same value. Further advantages is that in the computational model each place in the neuron is subject to be recorded, and that the location of the synaptic inputs can be set.

Distance dependence of $\tau\star$

In this set of simulations, an excitatory synaptic input was applied onto a single site along the apical dendrite (figure 3.6 A) . The aim is to study how the calculation of $\tau\star$ depends on the electrotonic distance between the application site (the dendrite) and the patch pipette (the soma). For comparability, the number of synapses was adjusted to produce an EPSP of $5mV$ recorded in the soma.

Thus, the amplitude recorded in the soma did not differ between distal (figure 3.6 B) and proximal (figure 3.6 C) application, though a low pass filtering of the distal application is visible due to space clamp. As expected from cable theory (Rall, 1960), the distal application produces a higher amplitude on site in distal locations (figure 3.6 D) than in proximal (figure 3.6 E). The recorded EPSCs are higher in amplitude for the proximal application (figure 3.6 G) in comparison to the distal application (figure 3.6 F). Similarly, the same effect is seen in the instantaneous time constant (figure 3.6 I vs H). As in the EPSP waveform, the low pass filtering of distal applications is observed for EPSCs and $\tau\star$.

We see, then, that the behavior of $\tau\star$ is qualitatively analogous to EPSCs. To study

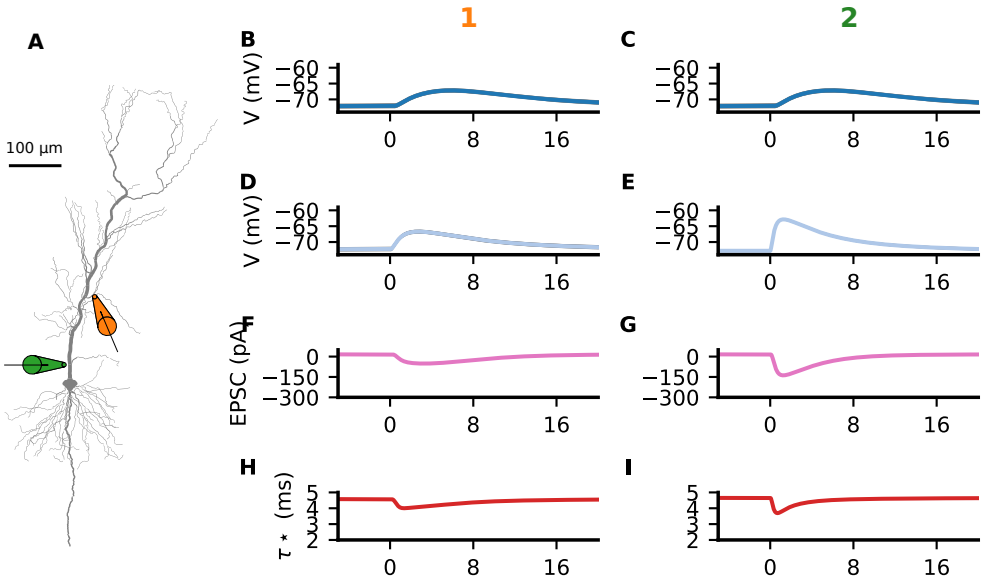

Figure 3.6: $\tau\star$ decays with distance from the applications site. (A) Morphology of the computational neuron. (B) Membrane potential of a distal EPSP measured at the soma. (C) Membrane potential of a proximal EPSP measured at the soma. (D) Same as (B) but measured in the application site. (E) Same as (C) but measured in the application site. (F) EPSC measured at the soma for same synaptic input as in (B) (G) EPSC measured at the soma for same synaptic input as in (C) (H) $\tau\star$ measured at the soma for same synaptic input as in (B) (I) $\tau\star$ measured at the soma for same synaptic input as in (C)

the quantitative behavior of the instantaneous time constant, the main features of the waveform (amplitude and rise and decay kinetics) were studied in terms of distance to soma. The amplitude of $\tau\star$correlates well with EPSCs (figure 3.7 A), indicating that the amplitude of the instantaneous time constant is a good indicator of the amount of synaptic input applied. To the contrary, the rise (figure 3.7 B) and decay (figure 3.7 C) show a systematically lower values for $\tau\star$ with respect to the EPSCs. The distance dependent increase is justified by the low pass filter properties of the membrane. Nevertheless, the lower values of the instantaneous time constant starting from the lowest electrotonic distance (where the effects of space clamp are lowest) suggests that $\tau\star$ underestimates the kinetics of synaptic input.

In summary, the amplitude of the waveform faithfully represents the amount of synaptic input being applied, whereas the waveform itself is faster than the synaptic input.

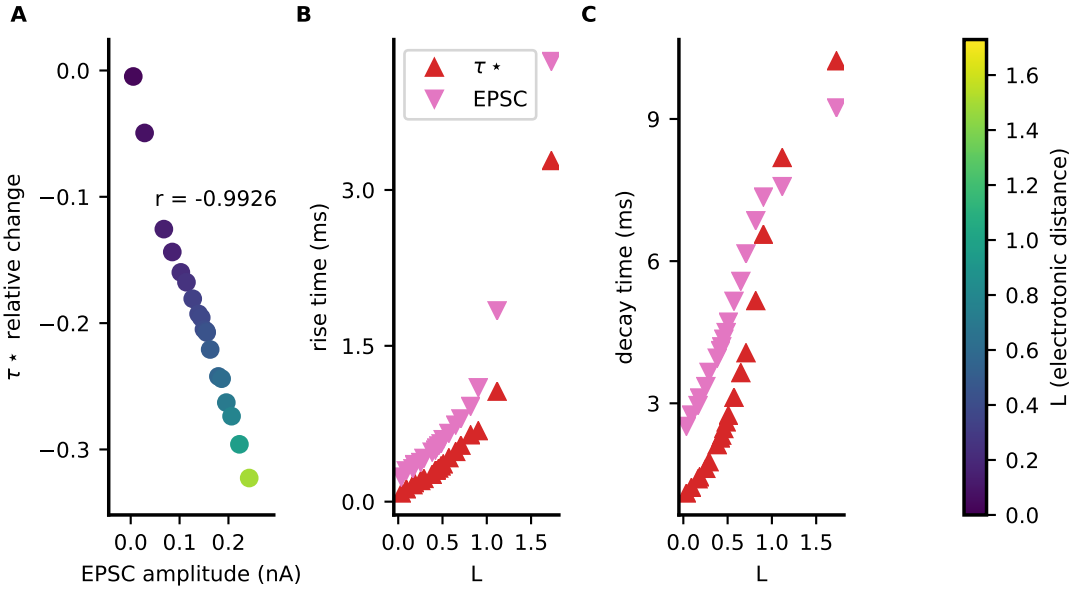

Figure 3.7: Distance dependent behavior of EPSCs and $\tau\star$. (A) Correlation of amplitudes between EPSCs and $\tau\star$. Color scale reflects the electrotonic distance (non dimensional). (B) Rise time of EPSCs and $\tau\star$ dependent on electrotonic distance. (C) Decay time of EPSCs and $\tau\star$ dependent on electrotonic distance.

Double input

The short-lived change in the passive properties during the opening of the synaptic receptors remains to be studied. In particular, I wanted to assess whether this reduction of the time constant affects the integration of two synaptic inputs from two different source. To that aim, I chose a reference stimulation in an apical trace (figure 3.8 A, blue trace) and three secondary stimulation sites at the same location, another apical dendrite, and a basal dendrite (figure 3.8 A). The simulations were performed with timings between both stimuli ranging from 0 to $10ms$. For the same timing between both applications, far away inputs (figure 3.8 D) result in greater EPSPs amplitude than close ones (figure 3.8 B), with the two apical stimulations in the apical arbor in a middle point (figure 3.8 C). The concurrent opening of the synaptic receptors from both stimulations can be seen from the overlap of the two waveforms both in the instantaneous time constant (figures 3.8 E-G) and EPSCs (figures 3.8 H-J).

Does this overlap of conductance play a role in synaptic integration? Normalizing the peak EPSP amplitude to the case of synchronous stimulations, we can see that

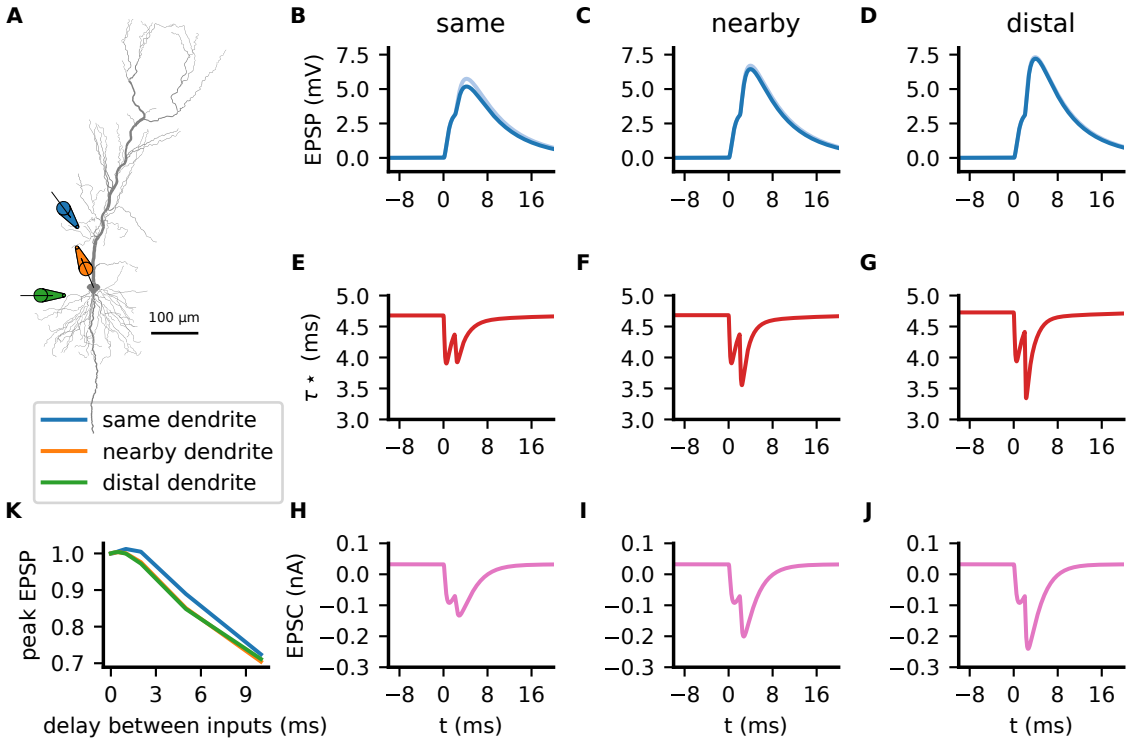

Figure 3.8: Integration of two inputs. (A) Schematic of the cell and the input sites. Average EPSP recorded in the soma for same dendrite input (B), proximal input (C) and distal input (D). Calculated $\tau\star$for same dendrite (E), proximal dendrite (F) and distal dendrite (G) input. EPSCs for same dendrite (H), proximal dendrite (I) and distal dendrite (J) input. (K). Peak EPSP of integrations as a function of the time delay between inputs. Data normalized to amplitude when inputs are simultaneous.

when the conductances are overlapping (first milliseconds) the EPSP peak amplitude is maintained. In particular, for inputs in the same dendrite, a mild increase in the peak amplitude can be observed (figure 3.8 K). This suggests that the overlap of conductances indeed helps synaptic integration.

3.3 Measurement of conductances during network activity

We found in section 3.2.1 that, under very specific conditions, a sinusoidal current injection helps recover the conductance changes due to excitatory input. The next question is whether this approach can also be applied to more complex patterns of activity, such as network oscillations. Hence, extracellular potentials were recorded during SPW-r activity in the pyramidal layer of CA1 from wild type mice. Simultaneously, a CA1 pyramidal cell was recorded intracellularly with sharp electrodes. Through the pipette we injected a sinusoidal current of sufficient amplitude to produce $\sim 2-3mV$ oscillation was injected. These recordings were kindly provided by Martin Kaiser, in Prof. Dr. Andreas Draguhn 's lab. The aim of this test dataset is to check whether the formalism of sinusoidal current injection can detect complex patterns of synaptic activities. In particular applying the extension to inhibitory synaptic input described in section 3.1.3.

3.3.1 Data recording

The sharp wave ripple complexes were detected based on the minimum of a bandpass filter of the local field potential (Bähner et al., 2011). Windows of $200ms$ around the center were taken to include a long baseline and allow to calculate the tonic conductance of the events, i.e., the passive terms depicted in equation 3.14. These terms remain constant throughout the recording and its accuracy is essential to obtain readouts of the conductances during the SPW-r proper.

Windows that contained more than one SPW were discarded. Besides, trials were discarded based on baseline instability, or noise (see section 3.2.1). Furthermore, as the neuron was subject to ongoing synaptic inputs, it fired action potentials. Windows that included APs were also discarded.

Afterwards, SPWs were averaged. If averaged together, the underlying ripple patterns patterns can be seen (figure 3.9 A). Furthermore, the spectrogram clearly presents two frequency bands of activity: The sharp wave, till 60 Hz and the ripple 200-300 Hz (figure 3.9 C), which matches literature values (Bähner et al., 2011).

Intracellular recordings also present a depolarization pattern during the SPW complex (figure 3.9 B). Moreover, the average intracellular membrane potential shows ripple-

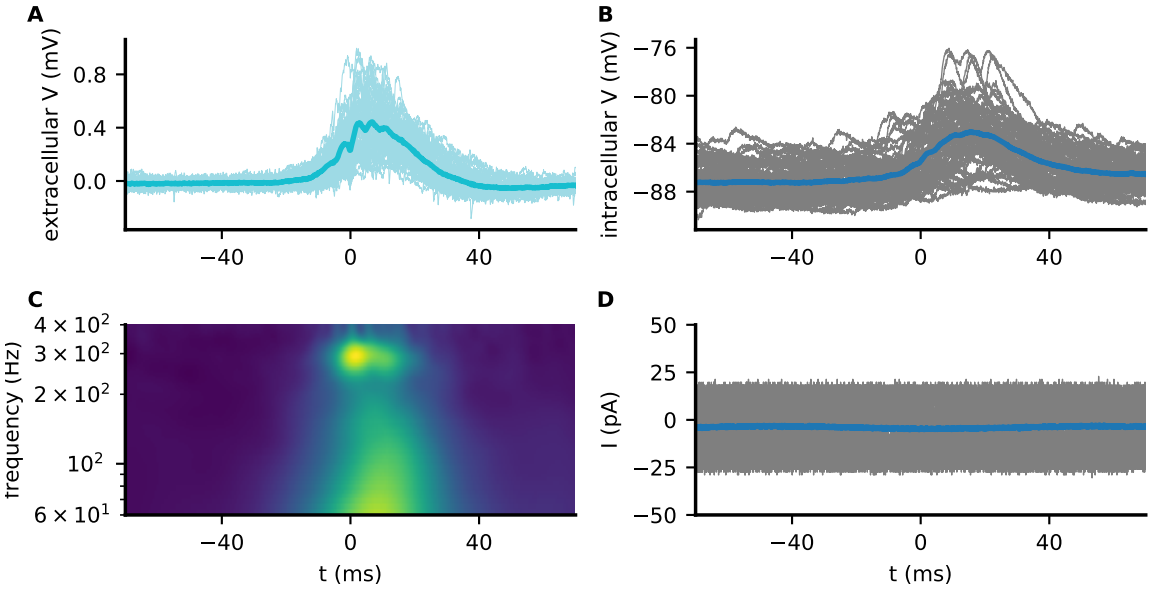

Figure 3.9: Overview of SPW-r recordings. (A): Extracellular recording of SPW-r events (light colors) and their average (darker). (B): Intracellular recording of a CA1 pyramidal cell during the recording in (A). Note the repeated pattern with the SPW. (C): Average wavelet spectrum of the total SPW-r. (D): Oscillatory current injected via the intracellular pipette (grey lines) and its average (blue lien). Note that averaging events reduces but not eliminates the oscillating component.

frequency pattern, though milder than the extracellular recording . The fact that the intracellular recording contains higher variability synchronized with the ongoing sharp wave suggests that intracellular membrane potential may contain enough information to determine the conductances.

3.3.2 The linear model and its limitations

The linear model described in section 3.1 was applied to the intracellular recordings (figure 3.9). Firstly, and for comparison purpose, the linear model for excitatory input applied in the previous sections was used ($\tau\star$model), although the presence of inhibitory currents is known and they are not considered inthis model. Then, the linear model with the inhibition component (described in section 3.1.3) is used to determine the inhibitory components along with excitation.

Indeed, direct application of the $\tau\star$model to the recorded membrane potentials (figure

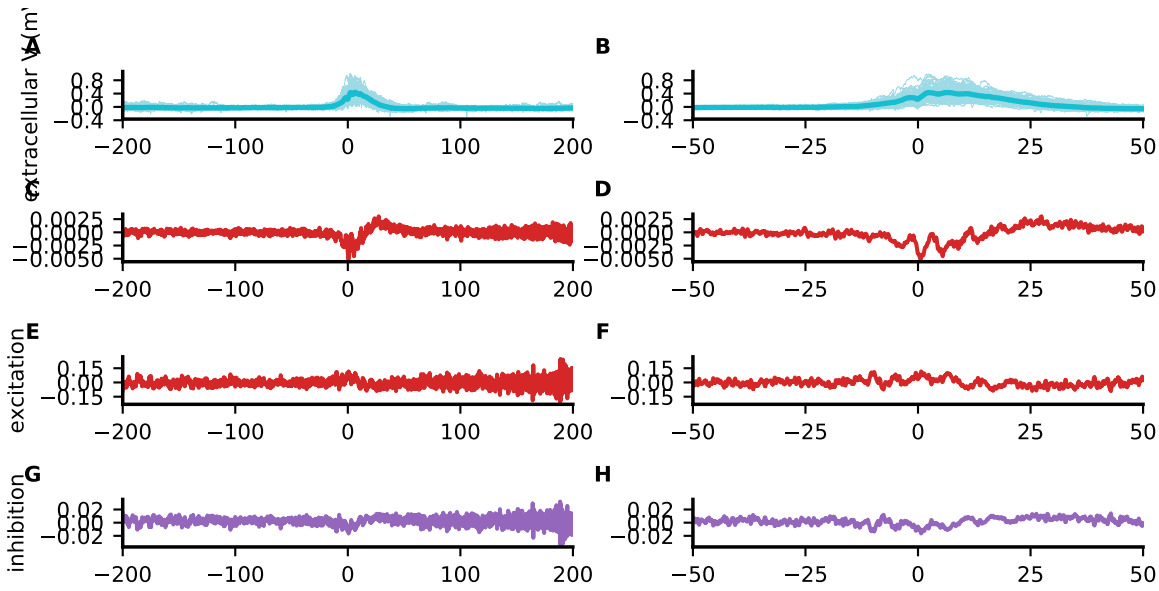

Figure 3.10: Limitations of the linear model to SPW-r recordings. (A) Membrane potential during events (same as figure 3.9 A). (B) Same, but zoomed out. (C) $1/\tau\star$ obtained by the linear model . (D) Same, but zoomed out. (E) Excitatory conductance obtained by the extended linear model. (F) Same, but zoomed out. (G) Inhibitory conductance obtained by the extended linear model. (H) Same, but zoomed out.

3.10 A) yields a waveforms which varies the most during the sharp wave, with high frequency oscillations corresponding to the ripples (figure 3.10 C, zoom in D, portrayed the inverse of $\tau\star$). In this manner, some information about the conductance is stored in the waveform, yet it contains several limitations. First of all, it has a noisy background. Secondly, $\tau\star$ refers to the time constant and must be always positive. As the output of the linear model is the inverse of the time constant, and this changes sign, it would yield a negative time constant (or infinite when $1/\tau\star$ is zero) and thus it carries no physiological meaning.

Another refinement is to include in the previous linear model a term for inhibition. The main problem of the extension to inhibition is the necessity to set a priori values from for the reversal potentials both for excitation and inhibition. Taking from the literature $E_{exc} = 0$ ((Hestrin et al., 1990)) and $E_{inh} = -64$ ((Huguenard and Alger, 1986)), the linear minimization was applied. In this case, we can recover a value for the excitation (figure 3.10 E, zoomed out in F) and the inhibition (figure 3.10 G, zoomed out in H). It can be seen from the traces than the main problems of the $\tau\star$ model are

still present whereas the ability to recover the ripple pattern is diminished.

Together, these results show that the linear model of $\tau\star$ does not suffice to estimate the conductance during complex network oscillations. Main problem is the presence of non tonic inhibition. The appearance of SPW-r alike patterns in the conductance estimations suggests, nonetheless, that the information is there and might be retrieved with a more powerful technique than a linear minimization.

3.3.3 Construction of a deep learning model

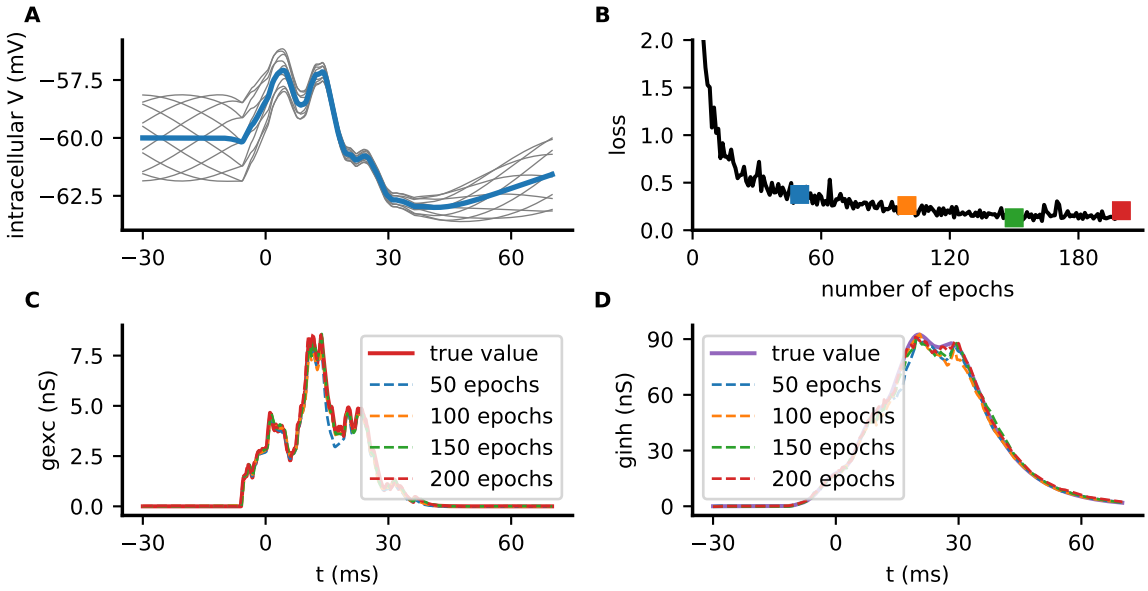

Figure 3.11: Deep learning model for noiseless simulated data correctly predicts the conducances. (A) Membrane potential response to injected current and sinusoidal input. (B) Loss of the deep learning model decreases with the number of epochs run. Colored squares depict the represented waveforms below. (C) True excitatory input (solid line) and reconstructed input (dashed) (D) True inhibitory input (solid line) and reconstructed input (dashed) through the deep learning model for different number of epochs.

To overcome the limitations of the linear model, a deep learning model was applied. The full details of the functioning and the architecture were presented in section 3.1.3. The first step is to assess whether this model can recover the excitatory and inhibitory signals under the most simple conditions. To that aim, excitation and inhibition where artificially constructed from a random distribution resembling the physiological emer-

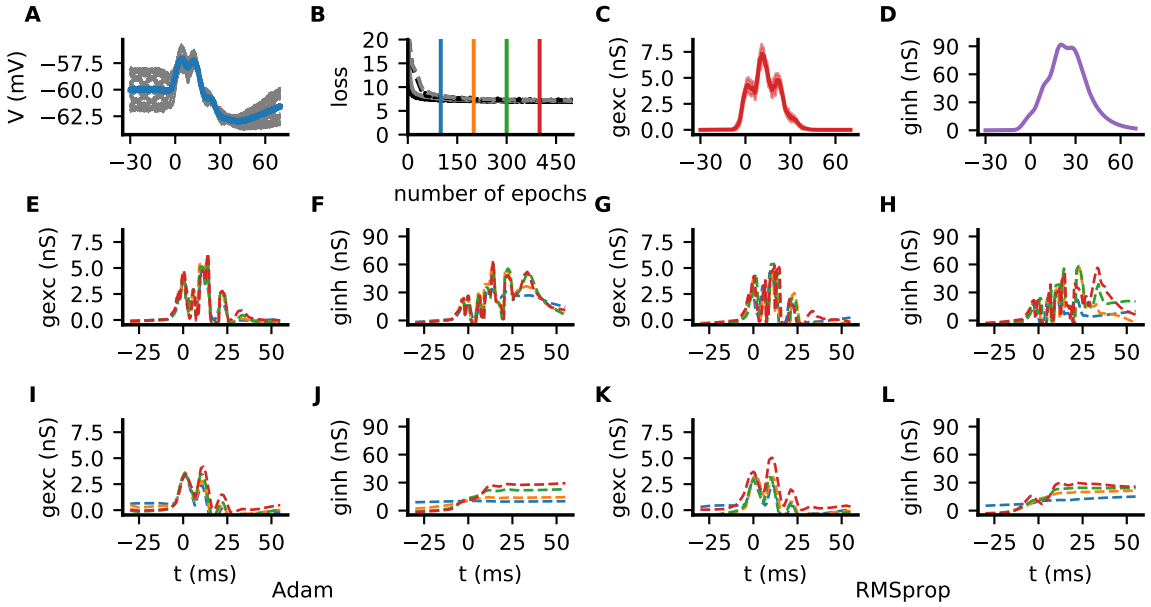

Figure 3.12: Deep learning model for variable inputs and white noise underestimates the value of the conductances.. (A) Membrane potential of all trials (grey lines) and average (blue). (B) Loss of models with Adam optimizer (black lines) and RMSprop (grey lines), and learning rate (lr = 0.001 (solid) and 0.0001 dashed lines). (C) True excitatory input (solid line, average) with standard deviation (shadows) (D) True inhibitory input (solid line, average). Note that the slower dynamics and higher maximum conductance makes the shadows indiscernible. (E), (F) Excitation and inhibition for Adam and lr = 0.001 (G), (H) Excitation and inhibition for RMSProp and lr = 0.001 (I), (J) Excitation and inhibition for Adam and lr = 0.0001 (K), (L) Excitation and inhibition for RMSProp and lr = 0.0001

gence of synaptic inputs during sharp wave ripples and applied to a single compartment neuron (figure 3.11 A). With this approach, the recovered conductances can be compared with the original values applied to the computational neuron. After letting the model process the data for 100 epochs, the minimization of the loss started to converge (figure 3.11 B), suggesting that the procedure was close the minimum it can reach Indeed, the values of the calculated excitatory (figure 3.11 C) and inhibitory (figure 3.12 D) are in close resemblance with their real counterparts (solid red lines).

In summary, for noiseless data, the deep learning model can recover the conductances from SPW-r like events.

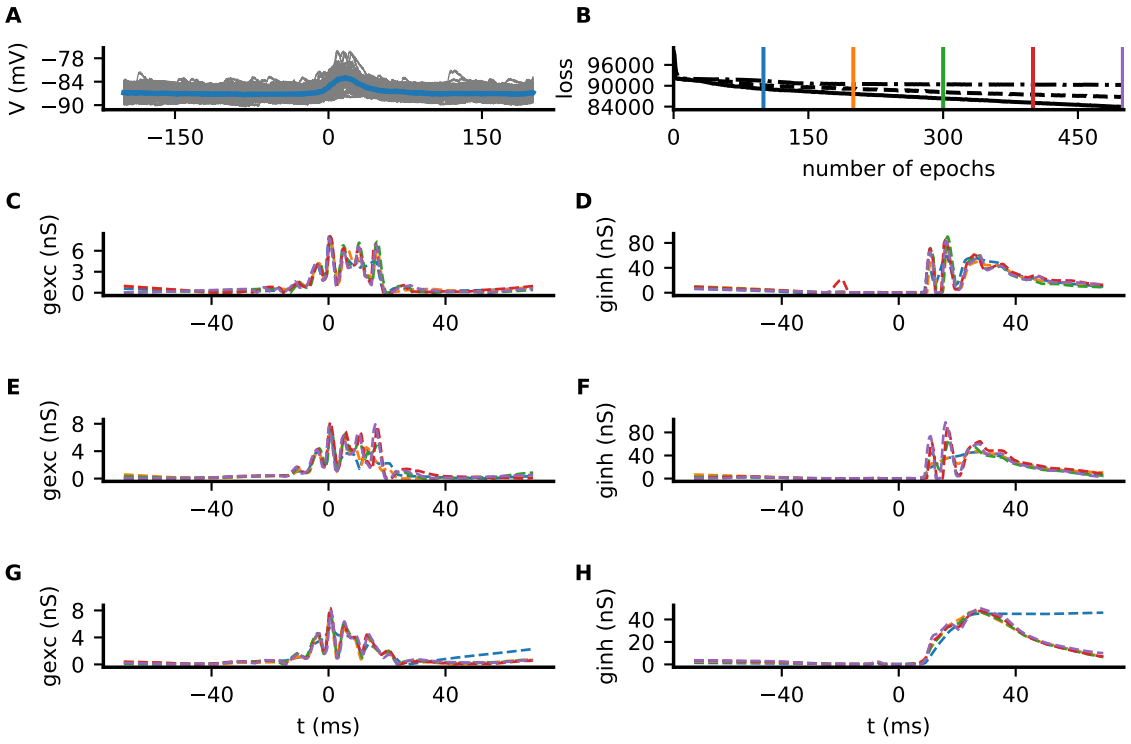

Figure 3.13: Deep learning model applied SPW-r to recordings has higher loss as simulated data. (A) Membrane potential of all trials (grey lines) and average (blue). (B) Loss of models with Adam optimizer for learning rates 0.0002 (solid), 0.0001 (dashed) and 0.00005 dotted. (C), (D) Predicted excitation and inhibition for lr = 0.0002. (E), (F) Predicted excitation and inhibition for lr = 0.0001. (G), (H) Predicted excitation and inhibition for lr = 0.00005.

Deep learning model with noisy data

The next necessary refinement for the deep learning model is to add variability. In experimental conditions, it is unavoidable to have a certain amount of recording noise. Furthermore, it is not possible to have exactly the same amount of synaptic input from trial to trial.

Hence, a noisy dataset was created. In this dataset all synaptic events where independently chosen each trial, so that each trial has the same number of synapses and the same time distribution, yet there is trial to trial variability. Furthermore, white noise with 0.1 mV amplitude was added to mimic the electronic recording error. The trial

to trial variability is clear in the membrane potential traces, where the same pattern of activity is seen, in this case with a component of noise (figure 3.12 A, compare to figure 3.11 A). As for the synaptic input, the trial to trial variability is clearly seen in the excitatory conductances (figure 3.12 B, lighter color). However, due to the higher amplitude of inhibitory conductances and its slower kinetics, the inhibitory variability is more uniform (figure 3.12 D).

The model as previously described did not converge to credible conductance values (data not shown). Thus, two changes were implemented in the deep network to better fit the data. The first one was to add to the loss function a weight in the form of a time dependent factor ($(1 - t^2)/(1 + t^2)$). The deep learning model tries to minimize an equation like in 3.14. In its current form, the drive to optimize at the baseline is the same as in the center of the sharp wave. Thus, in the borders, of the recording, where the phasic conductance is minimal and the signal to noise ratio is the highest, the optimization is biased away from the best solution. With this enhancement, the values of the baseline are still taken into account, but more importance is given to the window of the sharp wave, where the phasic conductances are happening.

Secondly, the network tended to the trivial solution. This means that if all the parameters would be zero, then the equation to be minimized will result in $0 = 0$ (equation 3.14 with parameters set to 0) and thus the solution is achieved. In the presence of noise or synaptic variability were, no perfect solution can be reached and thus the model tended more pronouncedly towards this trivial solution. To discouraged the system into that trajectory, the weight of the static loss (see figure 3.2) was changed from its value of 0.1 to 1. In this manner, the system two driving forces. The first one to find an optimal solution for the conductances and the second to maintain the passive parameters within reasonable values.

Furthermore, the nature of the data in this system is different from the noiseless case. Therefore, two state of the art optimizers (Adam (Kingma and Ba, 2014) and Adadelta (Zeiler, 2012)) were employed. They were tried with several learning rates $(0.0002, 0.0001, 0.00005)$ to explore the responses. This values start from the optimal values published (Chollet and others, 2015) and decrease to increase their effectiveness (Goodfellow et al., 2016).

In general, the loss with these experiments is systematically higher than in the noiseless case (figure 3.12 B). Noise and variability are most likely responsible of this increase. Furthermore, the predicted conductances do not converge near the real values in any

case. Nevertheless, we can observe better performance of RMSprop with respect to Adam (figures 3.12 E-L, right side vs. left side) and higher learning rates with respect to lower (figures 3.12 E-L, top vs. bottom). The most resembling solution is thus RMSprop with learning rate 0.001.

The predicted conductances show, nevertheless, some qualitative resemblances with the true conductances. The ratio between excitation and inhibition is well predicted, and the absolute value of the conductances is underestimated. Some time dependent oscillation behavior in the frequency range of ripples is observed, but its kinetics are faster and more extreme than voltage clamp recordings during SPW ((Maier et al., 2011))

Application to experimental data

The model described in the previous version was finally applied to the intracellular recordings. During preliminary experiments, it was found that, as opposed to the noisy simulated data, the Adam optimizer performed better than the RMSprop (data not shown). Applying the deep learning model to the sample recording (figure 3.13 A) for different learning rates shows a descend in the loss function, yet the absolute values remain orders of magnitude higher than with the test data (figure 3.13 B). This result shows that the amount of noise is higher than in the theoretical data and also that further patterns of activity are present that cannot be conveyed in the equation to be minimized.

However, inspection of the reconstructed excitatory and inhibitory conductances shows that they present waveforms that qualitatively correspond to the expected patterns of conductances. In the case of excitatory conductances, the different learning rates did not affect much the final conductance waveform and amplitude (figures 3.13 C, E ,G). On the other hand, inhibition was more influenced by the election of learning rate, with lower values yielding smoother responses (figure 3.13 H) and higher learning rates yield solutions with sharp oscillations (figure 3.13 D).

Quantitatively, the amplitudes calculated by the deep learning model are around $7nS$ for excitation and $\sim 50nS$ for inhibition. We must point out that, as in the presence of noise the model underestimated the theoretical conductances, these results are most likely also an underestimation of the real conductance happening in the neuron. Moreover, some known features of conductances during sharp wave ripples are present in

these reconstructed waveforms: the value of inhibition in several times greater than the value of excitation and also the onset of inhibition comes with certain delay with respect to the onset of excitation.

In summary, the deep learning model can recover some qualitative features of conductances during sharp wave ripples. Still, more refinements will be necessary to recover quantitatively reliable data.

3.4 Inputs onto AcD cells are privileged towards AP generation

Recently it was shown (Thome et al., 2014) that in 50% of CA1 pyramidal neurons, the origin of the axon is attached to a basal dendrite, rather than to the soma, as it generally happen. This dendrite that connects axon and soma is denoted Axon carrying Dendrite (AcD). This morphological feature has electrophysiological implications. Firstly, the isolation of the AIS from the soma makes input coming from the AcD trigger action potentials more efficiently. Secondly, this dendrite shows higher propensity of dendritic spikes. To explore the underlying mechanism, a computational model was constructed. The main questions to address were to reproduce the efficiency to trigger action potentials from AcD input and how electrotonic properties or perisomatic inhibition influence this efficiency. Finally, the higher propensity to dendritic spikes in the AcD is studied in terms of sodium channel density.

3.4.1 Reduction of AP threshold by AcD input

The first question to address is how the isolation of the AIS from the soma makes AcD input more efficient to trigger action potentials as input from other dendrites. For this aim, the computational neuron had a basal dendrite, AcD, to which the axon was connected at a variable distance from the soma (axon distance, *a.d.*). The first series of experiment consisted on finding the minimum input (number of synapses or current injection) to generate an action potential. This procedure was repeated for axon distance lengths from $0\mu m$ to $15\mu m$, in steps of $0.5\mu m$. For the case where the axon was attached to the soma (a.d. $= 0\mu m$) the calculated input was 5196 synapses for AcD, 5187 for nonAcD input and $0.375nA$ for current injections. For comparison, these values were

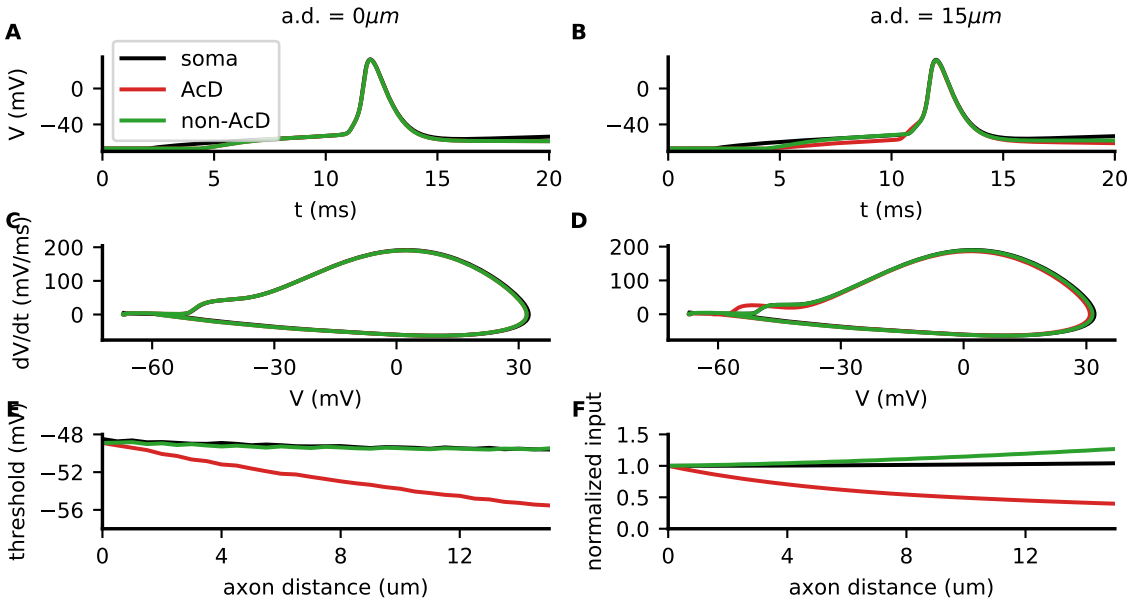

Figure 3.14: Axon distance elongation reduces current and threshold for AcD input. Data for current injection (black), AcD input (red) and nonAcD input (green). (A) Action potentials for $a.d. = 0\mu m$ have same waveform. (B) Action potentials for $a.d. = 15\mu m$ show decreased threshold for AcD input. (C) Phase plots for $a.d. = 0\mu m$ have same waveform. (D) Phase plots for $a.d. = 15\mu m$ show decreased threshold. (E) Threshold of AP initiation is reduced for elongated axon distance. (F) Input applied (normalized to $a.d. = 0\mu m$) increases for nonAcD input while decreases for AcD input.

used to normalize all further inputs.

For no axon distance, all three kinds of input show a similar AP waveform (fig 3.14 A), although somatic input needs more time ($\sim 10ms$) to achieve an AP in comparison to synaptic input ($\sim 8ms$). This is an effect of the injection procedure; synapses are all applied at a fixed time point ($4ms$ in the experiment), whereas current injection starts at a fixed point ($2ms$) and continues thereafter. Thus, less current injected for a longer time leads to the same waveform of AP. Closely examining the phase plot shape (figure 3.14 C) also shows no difference between the three cases considered. All of them show two components in the phase plot. The first one, starting at a polarized state is due to the invasion of the AIS-generated AP and is responsible for the first onset of the AP. At this point, the depolarization in the soma opens the sodium channels and the full blown somatic AP is generated, depicted in the second component of the phase plot.

The similarity between waveforms is broken when the axon steps away from the soma

via the AcD. In this case, although somatic current injection and nonAcD input resemble one another, the onset of the AP for AcD input comes at a more hyperpolarized state (figure 3.14 B). Furthermore, the separation between AIS an soma shifts the axonic invasion to the soma to more polarized states, i.e., lowers the threshold, while maintaining the other component unchanged (figure 3.14 D).

Quantitatively, somatic or nonAcD input results in similar threshold of AP initiation when there is no axon distance. In contrast, the threshold decreases monotonically for longer axon distances, with a threshold difference up to $-6mV$ for an axon distance of $15\mu m$ (figure 3.14 E). Similarly, less AcD input is needed for AP generation for longer axon distances, with 40% of the original input needed with $a.d. = 15\mu m$. Conversely, an enlarged basal dendrite between AIS and soma requires more input (up to 20% more) of nonAcD synapses to achieve an AP. The input remains constant for somatic current injection (fig 3.14). In the case of non AcD input, the elongation of the axon distance increases the electrotonic distance between input site and AIS. Thus the number of synapses must increase in the basal dendrite to elicit the same depolarization. In the case of AcD, the electrotonic distance between synaptic application site and AIS remains similar regardless of the axon distance. However, as the axon separates from the capacitive sink of the soma, the resistance to go into that direction increases. Therefore, a bigger ratio of the EPSP traveling through the AcD goes into the axon and thus the reduction in input.

Taking all together, synapses reaching AcDs need less input that their nonAcD counterparts to set an action potential and, as a consequence of the lesser depolarization caused in the soma, the threshold of AP initiation is reduced.

Is this difference in somatic action potential caused by the propagation from its initiation site, the AIS, to the soma or by other factors? To answer than question, we can observe the traces of soma and AIS for all the measured lengths and both synaptic inputs.

Recordings in the soma for AcD input show that: (i) the predepolarization is smaller for longer axon distances due to reduced input; (ii) the onset is shifted towards previous times, due to the facilitation of AP generation and also to the electrotonic detachment of the AIS from the soma and (iii) there is no alteration of the full blown AP waveform (figures 3.15 A, C). From the point of view of the AIS, the isolation from large capacitive surface of the soma diminishes the amount of current flowing from the AIS to charge the somatic membrane and continues depolarizing the AIS, leading to a higher maxi-

mum membrane potential and also faster onset (figure 3.15 D). Moreover, the isolation also makes the propagated AP from the soma milder when it reaches the AIS (second component of the AP, figure 3.15 B).

For nonAcD input, no clear distinctions of AP somatic waveform are observed for different axon distances (figure 3.15 E). Nevertheless, there is a slight reduction of the AIS component due to the electrotonic distance between soma and AIS that can be observed in the phase plot (figure 3.15 G). On the other hand, the AIS shows the same enhancement in peak and onset observed for AcD input (figures 3.15 F, H).

In summary, the electrotonic detachment of the AIS from the soma changes the AIS onset and its propagation to soma, although only in the case of AcD input the relationship between synaptic input, and AP generation is changed.

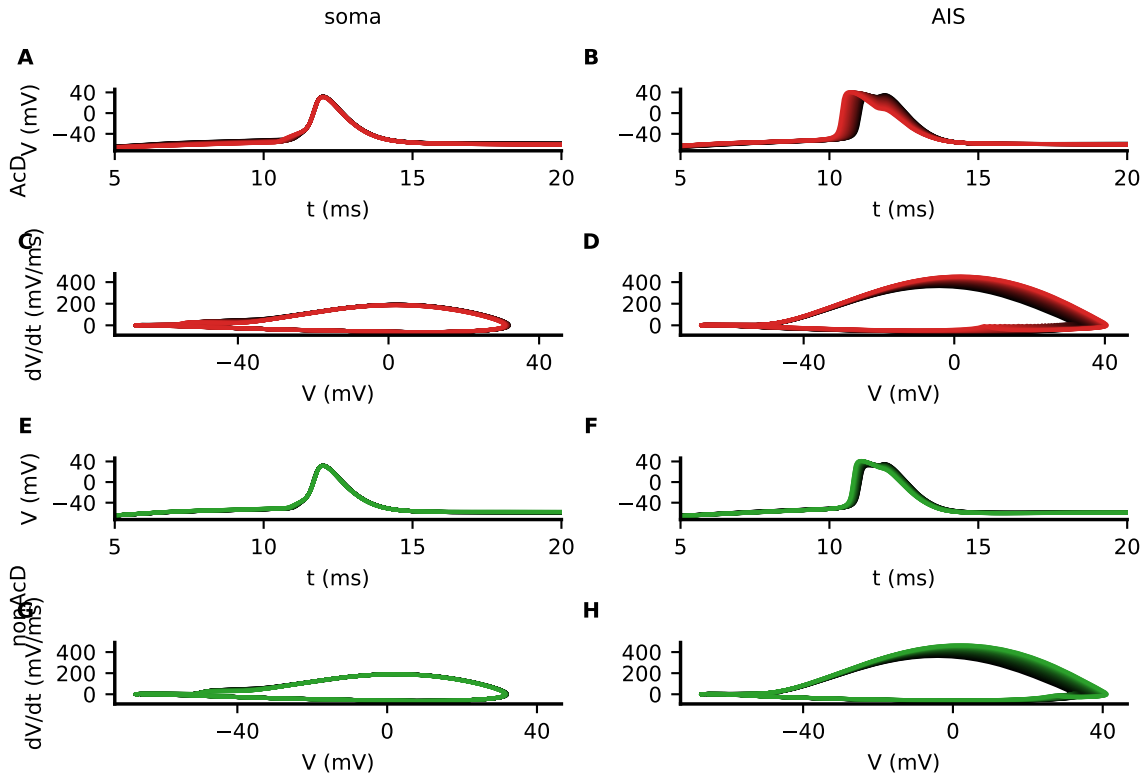

Figure 3.15: Overview of distance dependency from soma to AIS on AP waveform. Colors range from $a.d = 0\mu m$ (black) to $a.d. = 15\mu m$ for AcD input (red) or nonAcD input (green). (A) Somatic membrane potential shows a decrease in threshold for AcD input. (B) AIS membrane potential shows an earlier AP generation for increased axon distances and AcD input. (C) Somatic phase plot shows a decreased threshold for increased axon distances and AcD input. (D) AIS phase plot shows greater excitability of AIS with isolation from soma. (E) Somatic membrane potential shows no change in waveform for increasing axon distance. (F) AIS membrane potential for non AcD shows increased excitability of AIS but no change in threshold. (G) Somatic phase plot shows no changes in somatic waveform with axon distance. (H) AIS phase plot shows greater excitability of AIS with isolation from soma.

3.4.2 Passive propagation is responsible for the reduction in threshold

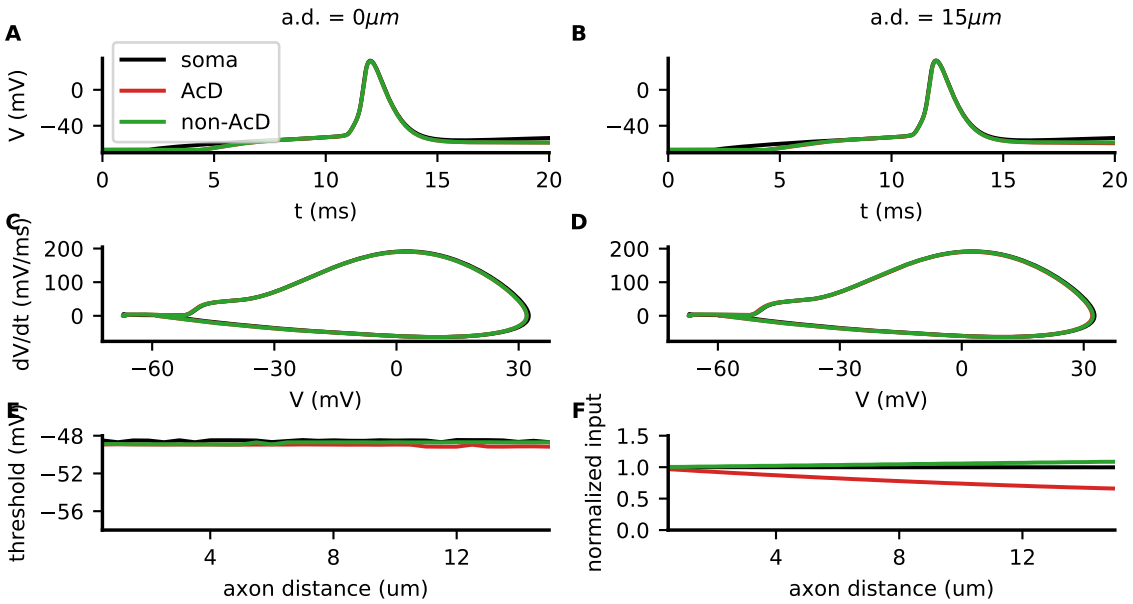

Figure 3.16: Axon distance effect diminished for compensated R_a. Data for current injection (black), AcD input (red) and nonAcD input (green). (A) Action potentials for $a.d. = 0\mu m$. (B) Action potentials for $a.d. = 15\mu m$ do not change from (A). (C) Phase plots for $a.d. = 0\mu m$. (D) Phase plots for $a.d. = 15\mu m$ do not change from (C). (E) Threshold of AP intitiation does not change with axon distance. (F) Input applied (normalized to $a.d. = 0\mu m$ from non-compensated experiments) changes less than in the non compensated case.

As seen in the previous section, the separation of the AIS from the soma reduced the threshold of AP initiation for AcD driven input. A plausible cause is that the increase in electrotonic distance is responsible of reducing the somatic depolarization at the time of AP onset. To test this hypothesis, the experiments were repeated with a compensated electrotonic distance. In this manner, the experiments are performed starting with an axon distance $a.d. = 0.5\mu m$. Then, for each increase in axon distance, axial resistance is reduced proportionally (Baranauskas et al., 2013),

$$R_a = Ra_0 \times \frac{L_0}{L} \tag{3.18}$$

leaving the product $L \times R_a$ constant, while changing the other biophysical magnitudes

(leak resistance, capacitance, and ionic channel densities), so that the only difference between these and the former experiments is the axial resistance.

With this compensated axial resistance, the elongation of the dendrite between soma and AIS does not change the predepolarization or the subsequent AP for AcD input with respect to nonAcD input or current injection (figures 3.16 B, D). Consequently, the threshold of AP initiation remains unchanged for different lengths in the case of AcD input, as well as its nonAcD or current injection counterparts (figure 3.16 E). It is noteworthy that the inputs necessary for AP generation do follow the trend observed in the previous experiments, though reduced in magnitude. In this fashion, the reduction of AcD input was of 30% (as opposed to 60% for normal axial resistivity) and the increase for nonAcD input was 10% (20% in the previous case) (figure 3.16 F, compare to figure 3.14 F).

Thus, the observed shift in the AcD threshold with increasing axon distance is mostly due to the axial resistance whereas the shift in input involves other biophysical factors. Indeed, when the current flows inside the dendrite between AIS and soma, the resistance to flow outwards (leak resistance) is the same as before, while the resistance to flow through (axial resistance) has been reduced proportionally to the length. Thus, in this scenario, more current will flow from the AcD towards the soma than towards the AIS, being needed more input to fire an AP. Conversely, due to the reduced axial resistance towards the AIS, current will flow more easily, resulting in the reduction of input.

3.4.3 Perisomatic inhibition enhances the threshold difference of AcD and nonAcD input

During network oscillations, the inhibition of basket cells acts onto basal and somatic areas of CA1 pyramidal cells (Klausberger et al., 2003). This perisomatic inhibition reduces greatly the input resistance of the pyramidal cells (Bähner et al., 2011). As AcD synapses the somatic compartment and travels directly to the AIS, it is likely that it is more decoupled from perisomatic inhibition than other synaptic inputs.

To test test this hypothesis, tonically open chloride channels were implemented, with reversal potential of $-75mV$ were adjusted to produce a 30% decrease in input resistance. With this model perisomatic inhibition, the axon distance was varied and the threshold and input necessary to trigger action potentials were measured.

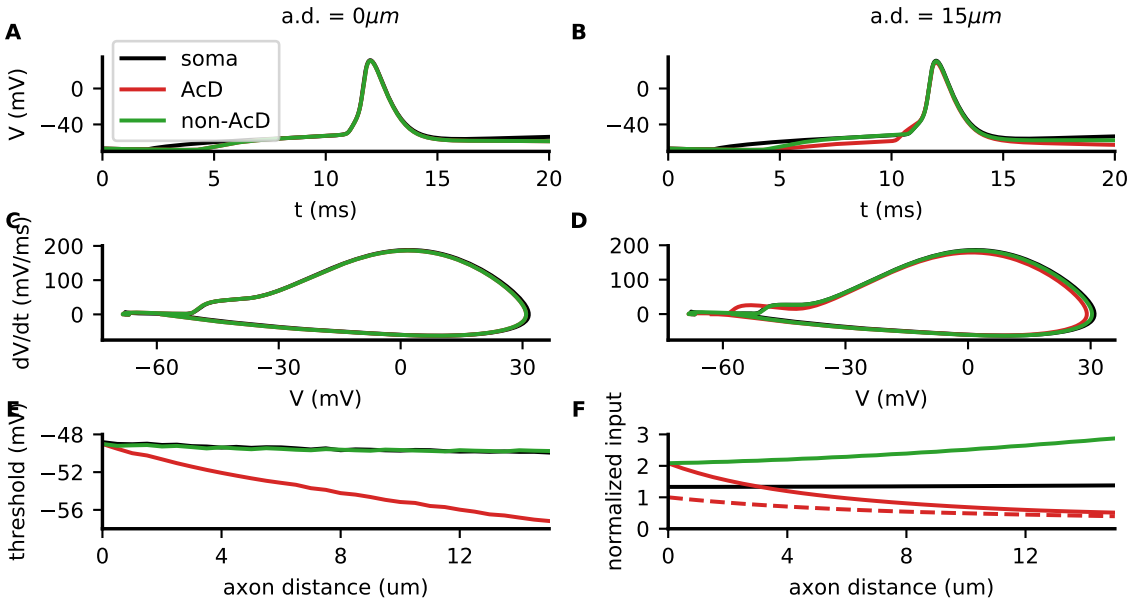

Figure 3.17: Perisomatic inhibition enhances the effect of axon distance. Data for current injection (black), AcD input (red) and nonAcD input (green). (A) Action potentials for $a.d. = 0\mu m$. (B) Action potentials for $a.d. = 15\mu m$ show decreased threshold for AcD input. (C) Phase plots for $a.d. = 0\mu m$. (D) Phase plots for $a.d. = 15\mu m$ show reduced threshold for AcD input. (E) Threshold of AP initiation. The difference is greater for AcD input than in the absence of inhibition while remaining unchanged in the other cases. (F) Input applied (normalized to $a.d. = 0\mu m$ without inhibition). Starting from higher values, for AcD input and long distances, the input without inhibition is recovered.

For no separation between soma and AIS, there was no difference in the corresponding thresholds (figures 3.17 A, C). For longer axon distances, the same lessened predepolarization and shift of the axonic onset (figures 3.17 B, D) were observed. In this case, the effect of the inhibition reduced the AP threshold more than without it, leading up to $-8mV$ (figure 3.17 E). The input necessary to trigger an AP was also reduced shift.

Moreover, perisomatic inhibition requires twice as much excitatory input and 50% more current injection to overcome the inhibition and trigger an AP in the case of no axon distance. For increasing axon distances, the tendency observed without inhibition is preserved, with AcD input decreasing, nonAcD input increasing and current injection slightly increasing (figure 3.17 F). Strikingly, for the longest separations, AcD input tends to the same input necessary without inhibition, meaning that the effect of perisomatic inhibition does not affect AcD input due to the physical separation between AcD-AIS

and soma.

3.4.4 Facilitation of dendritic spikes

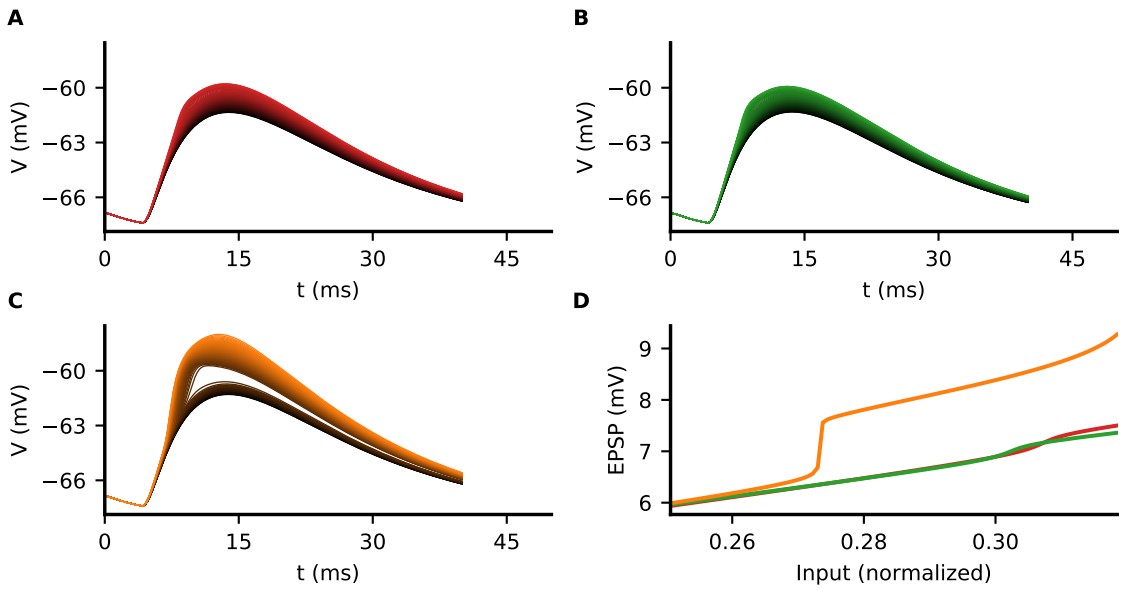

Figure 3.18: Additional dendritic sodium channels account for enhanced excitability in the AcD. Inputs range from 22% to 34% of the input to trigger an action potential. (A) Several EPSPs recorded in the soma for AcD input. Color ranges from black (weakest) to red (strongest). A mild increase in amplitude is observed when a dendritic spike is triggered. (B) Several EPSPs recorded in the soma for nonAcD input. Color ranges from black (weakest) to green (strongest). A mild increase in amplitude is observed when a dendritic spike is triggered. (C) Several EPSPs recorded in the soma for AcD input and enhanced Na^+ density. Color ranges from black (weakest) to red (strongest). A stronger increase in amplitude is observed when a dendritic spike is triggered. (D) Summary I/O curves from (A)-(C). Note that the non-linear jump is the transition from passive summation to dendritic spike.

Dendritic spikes are a powerful mechanisms of on-site dendritic integration and processing, mostly due to active sodium or calcium conductances. Experimental work found that AcDs are more likely to fire dendritic spikes than regular basal dendrites (Thome et al., 2014).

To test whether the higher likelihood of dendritic spikes in AcD is due to its morphological feature or to other factors, the input-output curve for synaptic input was

constructed. A stimulation site was set at $15\mu m$ from the soma for both AcD and nonAcD dendrites. Then, synaptic inputs were applied to this location with amplitudes ranging from 20% to 35% of the input to trigger and action potential and the resulting somatic EPSP was measured (figure 3.18 A-B). Dendritic spikes were easily recognized by a peak in the first derivative or by a non linearity in the I/O curve . Both AcD and nonAcD behaved qualitatively the same for increasing input showing a dendritic spike threshold at 31% of the input (figure 3.18 D). Nevertheless, immunohistochemistry images showed that there might be an increased sodium channel density in the AcD. To test if this increase can explain the higher propensity of dendritic spikes, we increased the sodium channel density by 20% (figure 3.18 C). Here, for increased input, a sharper increase in the EPSP amplitude can be observed. Moreover, the I/O curve in this case leads also to a reduced threshold of activation (figure 3.18 D). In summary, the enhanced DS excitability of the AcD with respect regular dendrites may be caused by an increased sodium channel density.

Taking these results together, the difference in electrotonic distance alone accounts for the reduction of the threshold of AP activation for AcD input. Higher propensity of dendritic spikes is unaffected but might be explained by a local increase in sodium channel density. Finally, the model predicts that AcD input for long axon distances is decoupled from perisomatic inhibition so as to trigger action potentials.

3.5 Bimodal distribution of ectopic action potentials upon alvear stimulation

Ectopic action potentials are a kind of action potentials whose origin arises deep in the axon, rather than from somatic depolarization (Spencer and Kandel, 1961). Therefore, they present a sharp onset seen in the trace and also in the phase plot. They have been studied in vitro in sharp wave ripples (Bähner et al., 2011), as well as in epileptic states (Velazquez and Carlen, 2000). Although they have been proposed to be the synchronization mechanism of CA1 pyramidal cells during sharp wave ripples (Vladimirov et al., 2013), they are yet to be recorded in vivo during sharp wave ripples.

It was shown by Dr. Christian Thome that extracellular alvear stimulation in the alveus produces a bimodal distribution of ectopic spike times in CA1 pyramidal cell recordings (data not shown). In one case, for small stimulation strengths, triggers spike

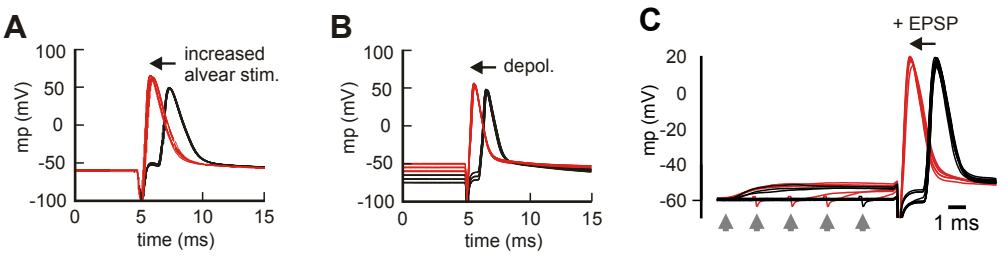

Figure 3.19: Summary of ectopic action potential experiments. Experimental data adapted from Thome *et. al.*(not published). (A): Increasing stimulation strength switches from late spikes (black) to early spikes (red). (B): Depolarizing current injection switches from late spikes (black) to early spikes (red). (C): Excitatory post synaptic potentials switches from late spikes (black) to early spikes (red).

peak around 2.5ms after the stimulation. This is denominated as late spike. For stronger stimulation strengths, the AP peak comes at 1.5ms after the stimulation (early spikes) (figure 3.19 A). Electrophysiological experiments have shown that synaptic stimulation can modulate a transition between both states.

The experimentalist hypothesized that this bimodal spike timing distribution mirrors two ectopic action potential initiation sites, namely the AIS and the first node of ranvier. To gain a deeper understanding on how these two kinds of action potential are generated in the axon, how they are backpropagated towards the soma and how synaptic stimulation couples with the axon to trigger action potentials, I constructed a computational model to mimic the experiments and be able to record on multiple sites simultaneously along the axon

The model follows the pyramidal cell presented in section 3.2. As the axon is a critical part of this study, its morphology was adapted to to have a more detailed axon. Its length was extended, and the biophysical properties that model the myelin sheath were finely tuned (see methods). The precise lengths were taken from immunohistochemistry observations of Dr. Alexei Egorov .

The extracellular alvear stimulation was modeled by two points set 75μm apart, acting as the tips of a bipolar stimulator. A current flowing between both electrode tips generates a distance dependent electric field that affects the active parts of the axon, namely the nodes and the AIS (figure 3.20 A). For small stimulation strengths, a short lived depolarization appeared in the nodes, and the axon quickly recovered its polarity due to the capacitive currents (figure 3.20 B). Although the peak depolarization was high

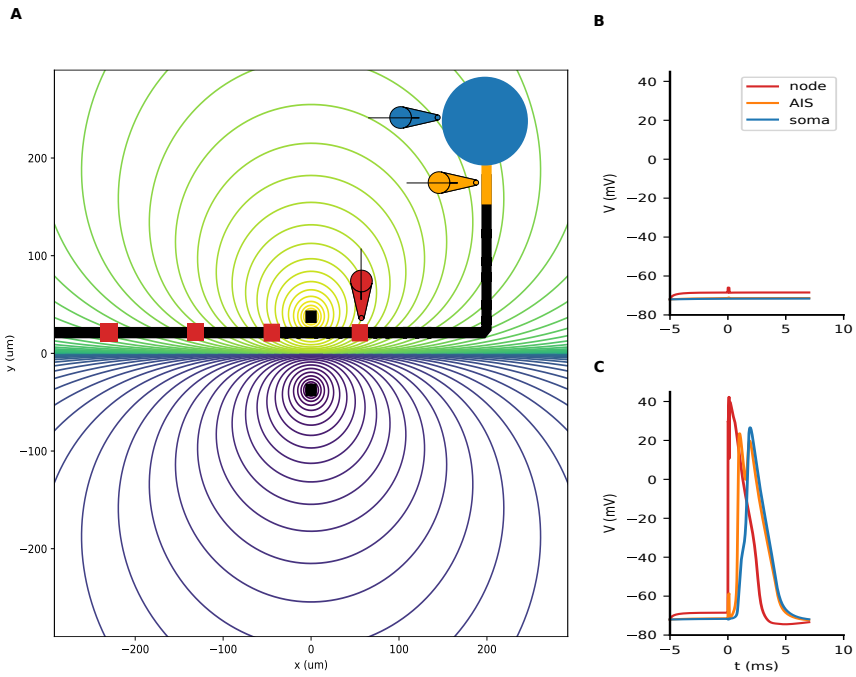

Figure 3.20: Experimental stimulation setting. (A): Schematic of the somatoaxonic axis of the neuron, along with tips of the bipolar stimulator (black dots). The stimulation generates a distance dependent field (color coded in the figure) that decays with distance. Thus, the stimulation received at the first node is greater than in the AIS. (B): A subthreshold stimulation creates a stimulation artifact in the node (red) but does not trigger an AP anywhere. (C): A suprathreshold stimulation generates an AP in the first node of ranvier (red) that is propagated first to the AIS (orange) and then to the soma (blue).

enough to open sodium channels in the node, its rapid recovery to resting membrane potential prevented the triggering of an action potential. For greater stimulations, the depolarization lasted enough to ensure the sodium channels will open, and therefore set the initiation of an AP (figure 3.20 C). From the traces, we can see that the first spike occurs at the first node of ranvier, followed by the axon initial segment and finally arriving at the soma. This suggests that the initiation site is the node of ranvier. Moreover, the time of the peak recorded at the soma ($\sim 2.5ms$) is in agreement with the late spikes from the experimental data.

With this calibration experiment, we can see that the extracellular stimulation can trigger ectopic action potentials.

3.5.1 Modulation of early and late spikes

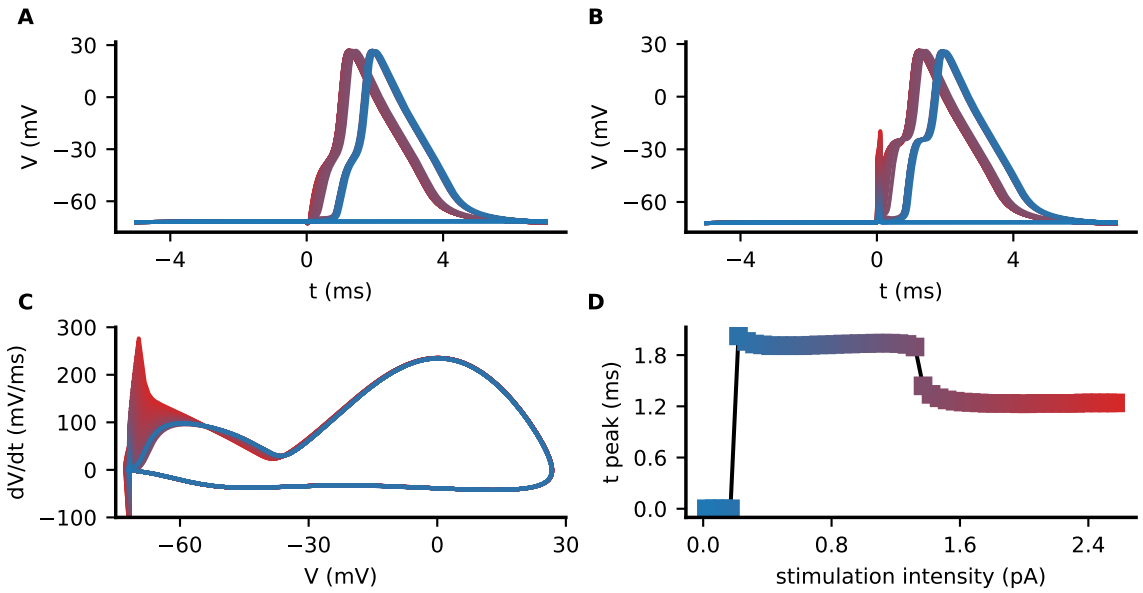

Figure 3.21: Stimulation intensity a bimodal distribution of AP timings. (A): Increasing stimulation intensity (red strongest) switches from no action potential to late spike to early spike in the soma. (B): Increasing stimulation intensity (red strongest) switches from no action potential to late spike to early spike in the AIS. (C): Somatic phase plot shows no difference in waveform (except stimulation artifact) for both spikes.. (D): Bimodal distribution of peak of AP depends on stimulation intensity.

With the model being able to generate ectopic action potentials, can the strength of stimulation affect the timing of action potentials? To test that, the experiment was repeated for different currents in the extracellular stimulator (figure 3.21 A). As described in the methods, the reference for the spike generation was set to be the peak of the spike, rather than the more cumbersome onset. Small stimulation strength yield no spike; for stimulations greater that $0.5nA$, a spike was generated, with a delay around $2ms$ with respect to the stimulation. Furthermore, for even greater stimulations (above $1.4nA$), the stimulation yields another set of spikes with a considerable smaller delay time, around $1.2ms$ (figure 3.21 D). A careful look at the phase plots from the traces recorded at soma shows the typical behavior of an antidromic spike (figure 3.21 C), with two clear components: The first one is the passive invasion of the sodium-driven activity in the AIS, and is characterized by a bump in the derivative while remaining in the polarized regime. The second, moreover, shows the active opening of the somatic sodium channels

and the achievement of full depolarization. The phase plots also show that both early and late spikes show as similar shape, with the exception of the stimulation artifact, which is greater for early spikes and gets merged with the AIS component of the phase plot. This shows that both early and late spikes look mostly the same from the point of view of the soma, with the exception of the onset of the AP, which is affected by the stimulation strength.

The data above shows that there are two distinct timings of somatic spikes, yet their AP properties are rather alike from the phase plots. To investigate further details of this phenomenon, a detailed response along the axon is to be studied. The traces along time at every position of the somatoaxonic unit are plotted (figure 3.22) for early (A) and late (B) spikes The polarized value of the membrane is depicted in violet-like colors. At $t = 0ms$, we see a short lived depolarization due to the stimulation artifact. In the case of the late spike (figure 3.22 A), the spike is generated in the node, which is the place where the earliest full depolarization can be seen. From there, the spike is propagated (forward in time, downward in the figure) towards the distal part of the axon and also back propagates toward the soma. On the axon, some bumps on depolarization can be distinguished, which correspond to the active nodes within the insulating myelin. Also, the clear delay that this propagation experiences to reach the soma is due to the capacitive currents necessary to fully charge the large soma. Similarly, in the case of an early spike (figure 3.22 B), the generation of a spike in the node can be seen, as well as its propagation towards the distal axon. In this case, however, the stimulation was also strong enough to generate a second spike the AIS, which is propagated (again, forward in time, downward in the plot) to the rest of the axon, and towards the soma. When the two spikes, one generated in the AIS and the other in the first node, encounter each other in the axon, none of them can further propagate as the sodium channels required for propagation have been inactivated by the other spike. Therefore, no effect of the node-initiated spike can reach the soma, and the trace recorded there includes only the spike generated in the AIS.

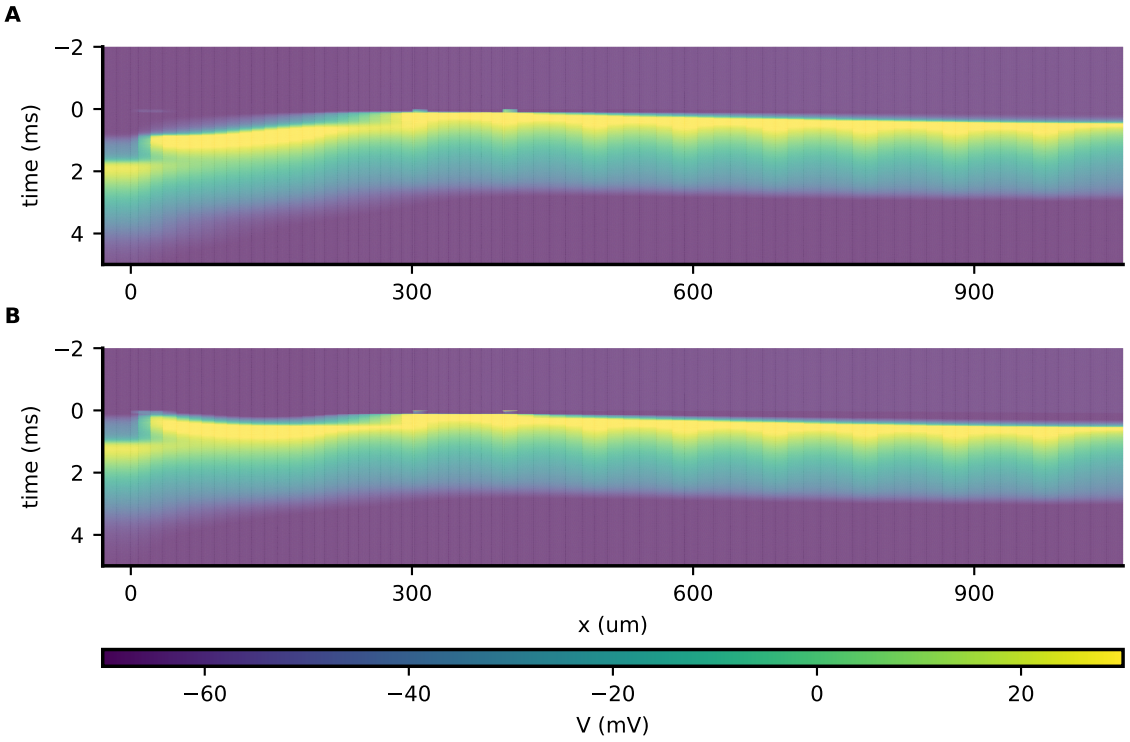

Figure 3.22: Propagation of an ectopic AP along the axon in space and time. (A) A late spike is generated first in the node (uppermost warm colors) and then propagated orthodromically through the axon and antidromically towards the soma (forward in time, downward in the figure). (B) The early spike is generated in the AIS (uppermost warm colors on the left) and the propagated to the soma, where an AP is generated in less time than in (A). Although a second ectopic AP is generated in the node, it cannot reach the soma as the sodium channels in between have already been inactivated by the AIS spike.

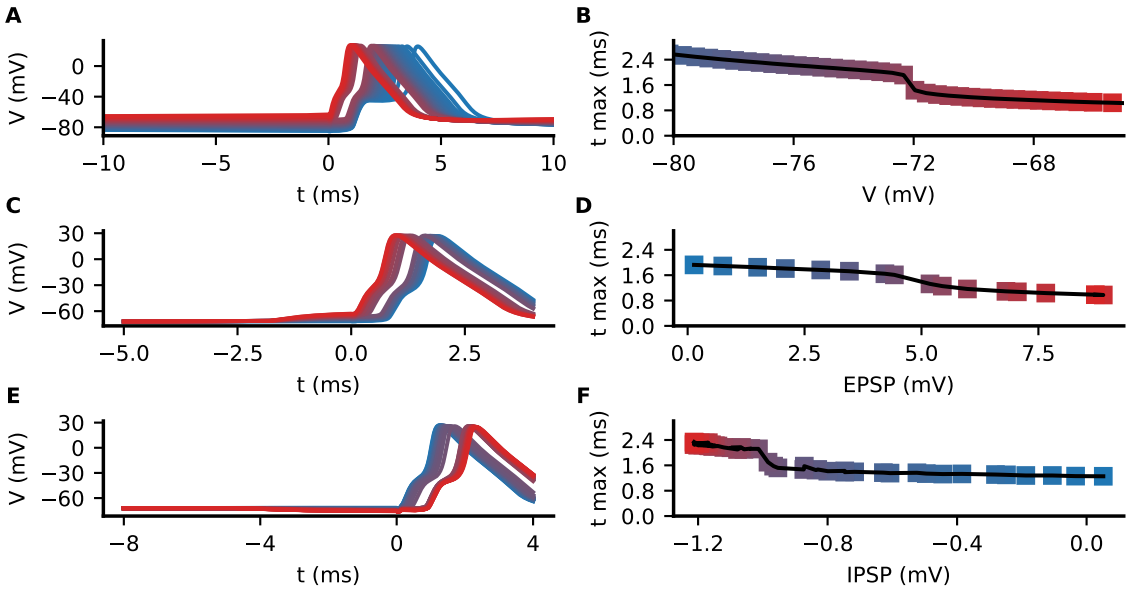

Figure 3.23: Polarity dependence of early and late spikes. (A) Somatic membrane potential for different current injections (color coded) and an extracellular stimulation of AA (B) Time of peak AP recorded in soma. Note the discontinuous jump at $-72.5mV$. (C) Somatic membrane potential for different EPSP amplitudes (color coded) and an extracellular stimulation of AA (D) Time of peak AP recorded in soma. Note the discontinuous jump at $5mV$. (E) Somatic membrane potential for different IPSP amplitudes (color coded) shows bimodal distribution. (F) Time of peak AP recorded in soma. Note the discontinuous jump at $-1mV$.

3.5.2 Synaptic modulation of AP generation

Once we have seen that early and late spikes can be triggered depending on the stimulation strength, the next question is whether, under a constant alvear stimulation strength, other mechanisms can make a transition between these two states, like depolarization of post synaptic potentials did on experimental data (figures 3.19 B, C, like depolarization of post synaptic potentials did on experimental data (figures 3.19 B, C)

The first attempt to study how late and early spike generation is dependent on membrane state is to check how membrane polarity affects its modulation. For that, several somatic current injections were applied and checked against the same extracellular stimulation ($1pA$, figure 3.23 A). The stimulation was chosen so that it falls within the late spike range and may potentially switch to early spike or to failure. Stronger, more positive current injections lead to increased depolarization. This depolarization, in turn, switches to an early spike at $-72mV$ of membrane potential at the time of alvear stimulation (figure 3.23 B). On the other hand, negative currents cause hyperpolarization and delay the spike time. As opposed to varying the strength of the extracellular stimulation, the current injection is changing the state of the membrane and thus, the activation or inactivation of ionic channels. Therefore, the AP waveform and kinetics are changed as a function of membrane potential and the time of the AP peak shows a steady decrease trend (figure 3.23 B) apart from the stark jump seen at $-72mV$. Besides, as a consequence of this trend, the timing difference between early and late spikes is smaller ($0.5ms$ vs $1.2ms$) as the difference when changing the extracellular stimulation strength (see figure 3.21).

When injecting a constant current from the soma, the membrane potential is changed throughout the neuron. Post synaptic potentials, on the other hand, produce a sharp potential change at the site of application, which is propagated with delay and waveform low pass filtering towards other regions of the neuron. The procedure was repeated for the same extracellular stimulation strength ($1pA$) and excitatory synaptic application in the apical dendrite. A $5mV$ EPSP amplitude switches the spike from early to late (figure 3.23 D), with no other visible changes in the shape of the AP (figure 3.23 C). Furthermore, IPSPs elicit the opposite transition, from early spike to late spike. The procedure was repeated, choosing an extracellular stimulation of $1.6pA$, to ensure an early spike, and IPSPs of increasing amplitude were applied. Due to the reversal potential of GABA being closer to the membrane resting potential, IPSPs amplitudes were smaller than EPSPs (figure 3.23 E). Nevertheless, at $-1mV$ amplitude, there is a transition between

early and late spike.

Qualitatively, these results show that membrane potential within the neuron can modulate the onset of early and late spikes. Moreover, synaptic input can further cause analogous behavior.

Quantification of modulation on AP generation

In the previous section I have shown that, under the same extracellular stimulation, somatic current injections and post synaptic potentials act as a switch between early and late spikes. Three questions remain to be answered. The first one is whether synaptic input can also make a transition between an extracellular stimulation that elicits no spike (failed stimulation) and a late spike. Second, how is the synaptic/current input quantitatively related to the alvear stimulation. Third, are the AIS and the first node of ranvier the initiation sites of early and late spikes, respectively?

Thus, the next experiment deals with the transition between failed spike and late spike from a quantitative point of view. In order to quantify the relationship between alvear and other input, the threshold of late spike generation is used. This threshold is the amount of alvear stimulation needed to elicit a late spike under other inputs (either excitatory or inhibitory synapses, or somatic current injection). For ease of comparison, values of the threshold are normalized to the alvear input necessary to trigger an early spike in the absence of any other input. The simulations were carried out using different amounts of somatic current injection and, in the case of synaptic input, different number of synapses as well as different timings with respect to the alvear stimulation were used.

Different amounts of current injection, or synaptic input produced similar AP waveforms as well as similar peak AP timings (figure 3.24 A). When depicted the threshold of late spike generation against the membrane potential in the soma at the time of alvear stimulation, we can see a negative correlation between them (figure 3.24 B). This result is intuitive: The more depolarizing drive present in the soma, the less input is necessary for the alvear stimulation to depolarize until the AP is generated. Conversely, the more hyperpolarizing drive in the soma, the more input is necessary to overcome that hyperpolarization and generate an AP. There are, however, some cases in which the same membrane potential in the soma require different amounts of alvear stimulation to trigger a late spike. The correlation between membrane potential due to synaptic input in the soma and threshold is almost linear for the same timing, and the steepness

depends on the timing. The closer the synaptic stimulus is to the alvear stimulation, the flatter the slope is. This suggests that membrane potential in the soma is related to the threshold of activation, but this correlation is blurred by timing factors.

Comparing the membrane potential in the axon initial segment to the threshold (figure 3.24 C), there is an increase of the correlation, yet there are still different slopes, depending on the synaptic timings. On the other hand, the membrane potential at the first node of ranvier shows a much higher correlation, with the differences in timings disappearing (figure 3.24 D). As the effect of the synaptic input onto the first node of ranvier does not depend on the timings and is the same as the one due to tonic current injection, the membrane potential recorded there is the best predictor of the threshold of late spike generation and, thus, it is likelier that the AP is generate at that location.

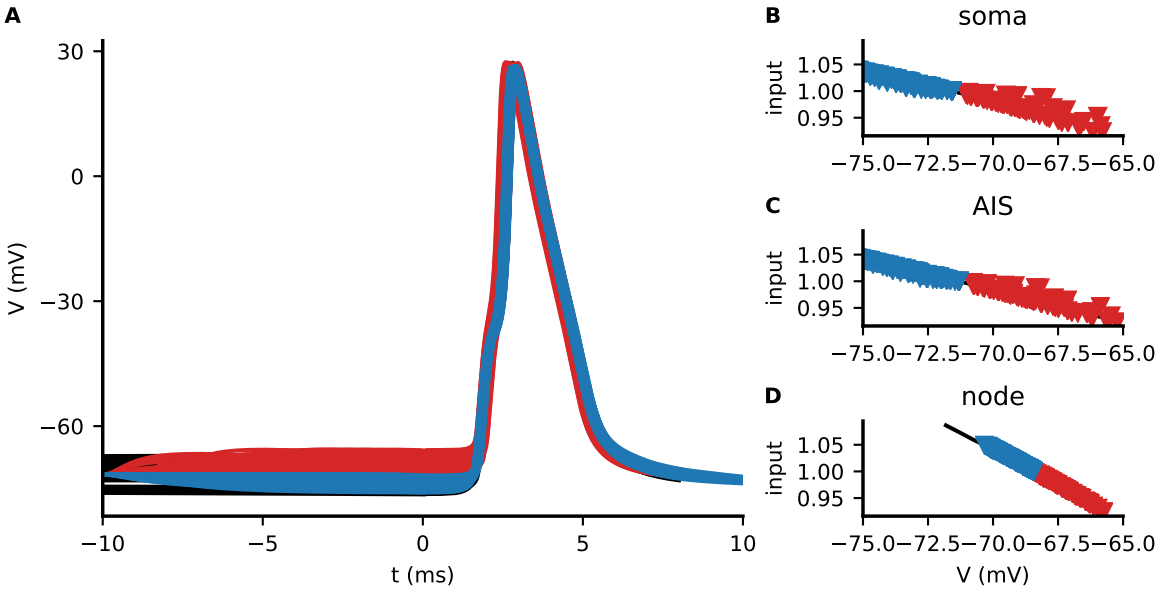

Figure 3.24: Quantification of polarity onto AP generation (A): sample traces with different current injections (black), EPSP (red) and IPSP (blue) and their subsequent late spikes. (B) Scatter of input and membrane potential in the soma shows a slight correlation. (C) Scatter of input and membrane potential in the AIS shows higher correlation than in the soma. (D) Scatter of input and membrane potential in the node is highest suggesting that it there where the influence of membrane potential is highest.

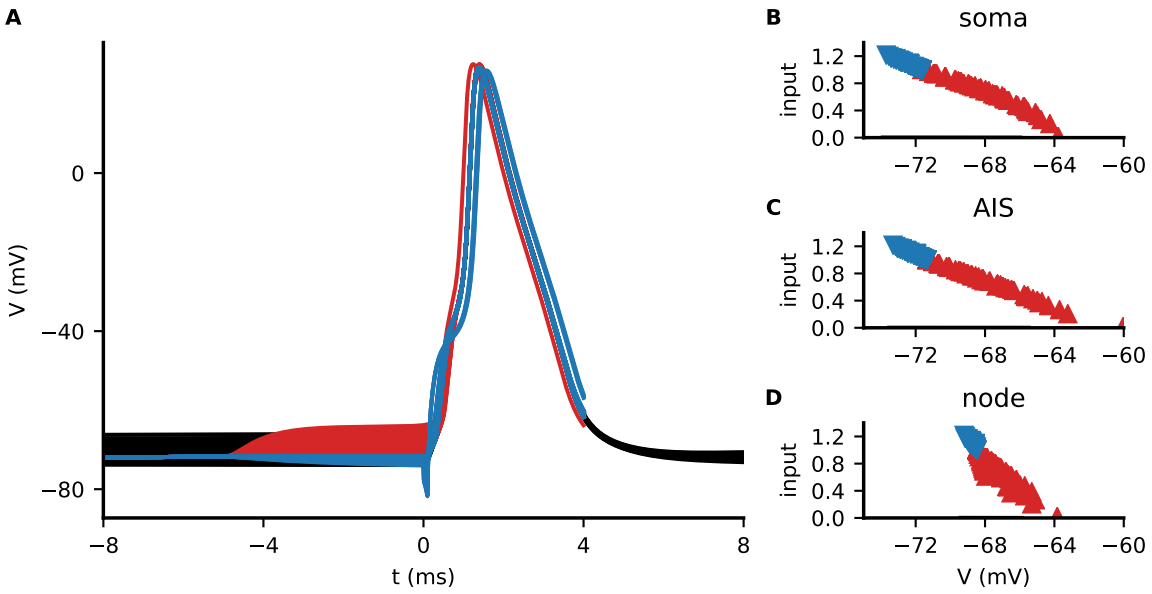

Figure 3.25: Early spikes under synaptic input. (A): sample traces with different current injections (black), EPSP (red) and IPSP (blue) and their subsequent early spikes. (B) Scatter of input and membrane potential in the soma shows correlation. (C) Scatter of input and membrane potential in the AIS shows highest correlation suggesting it is there where the influence of membrane potential is highest. (D) Scatter of input and membrane potential in the node is lower than in the AIS.

Quantification of modulation on late to early transition

For the quantification of the threshold between late and early spikes, the same simulations were carried out. In this case, the alvear stimulation was chosen so as to have the peak of the action potential within $1.2ms$ after the alvear stimulation.

In this case, the stimulation artifact is more pronounced, due to the stronger stimulation required to trigger an early spike (figure 3.25 A). Moreover, the range of thresholds is broader than in the case of late spike (120% to 27%, figure 3.25 B). When compared to the membrane potential in the soma, the different slopes dependent on the timings of the synaptic input are not as pronounced for the membrane potential in the soma (figure 3.25 B). The same applies to the axon initial segment (figure 3.25 C). On the other hand, the slopes are tilted depending on the timing for the membrane potential recorded in the first node of ranvier (figure 3.25 D). This tilt occurs in the opposite direction than in the case of late spike generation: Less timing between synaptic input

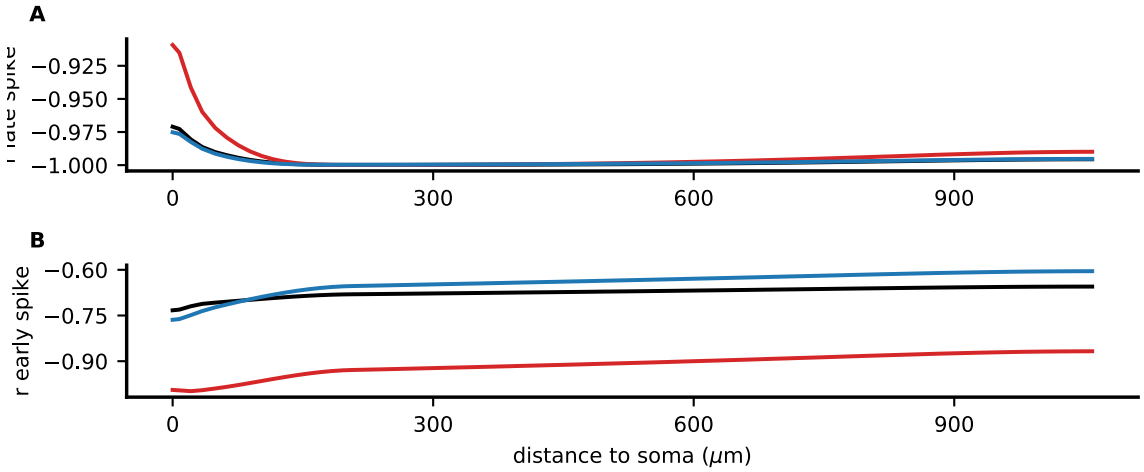

Figure 3.26: Correlation of input and membrane potential along the somatoaxic axis. (A) For late spikes, correlation is highest at the first node, showing that the effect of membrane potential is highest there for excitation (red) inhibition (blue) and current injection (black). (B) For early spikes, correlation is highest at the AIS, showing that the effect of membrane potential is highest there for excitation (red) inhibition (blue) and current injection (black).

and alvear stimulation produces more tilted lines.

Together, this suggests that for early spike generation, the best predictor lies in the soma-AIS area, as the correlation is higher. The different behavior of the slopes can be understood by the morphology and its propagation effects: When the AP is generated in the node, the modulating post synaptic potentials must pass first through the AIS and the soma. For short timings, the low pass filtering of the PSPs through the axon is more accused. This forces excitatory post synaptic potentials with short timings to have more amplitude in the soma and AIS to produce the same depolarization in the first node of ranvier. The higher amplitude in the soma for the short timings produces the flatter lines in figure 3.24 B. The opposite effect occurs in the case of early spike. The key region in this case is the axon initial segment. Short delays are more passively filtered than longer delays, so by the time they reach the first node of ranvier, their amplitude is less than those with longer timings, for the same amplitude in the AIS. Thus, the slopes for shorter timings are more tilted than the ones for longer timings when measured in the AIS. The same reasoning can be applied to inhibitory postsynaptic potentials.

So far we have only considered the AIS and first node of ranvier as sites of modulation of late and early spike. Although the greater sodium channel concentration of these to regions makes them the most likely sites, any another place along the axon might be the modulating site. As seen before, the higher correlation between minimum input to elicit a spike and membrane potential at a given site determines the modulating site. To further test that AIS and first node of ranvier are the generating sites of early and late spikes, respectively, I computed the correlation between threshold alvear input and membrane potential throughout the axon. Late spikes have the highest correlation in the first node of ranvier, whereas this correlation decreases towards the distal parts of the axon and also decreases more abruptly towards the soma (figure 3.26 A). This change in correlation is more accused towards the soma due to the distortion that the charging of the somatic region causes. On the other hand, early spikes show the greatest correlation in the axon initial segment, and then it decays from there towards the soma and along the axon (figure 3.26 B).

Taken together, these results show that extracellular stimulation in the axon can reproduce ectopic action potentials in a bimodal distribution. This bimodal distribution is caused by different initiation sites (node and AIS), and the initiation site can be modulated by synaptic action.

Modulation of early spikes by sodium channel density

Action potential initiation in relies critically on the high sodium channel density in the AIS (Yu et al., 2008). How does this sodium channel density affect the modulation of early and late spikes? To study this effect, I varied the sodium channel density in the axon initial from 0 to $0.30 S/cm^2$ and tested the response for an alvear stimulation ($1.5 pA$) than produces an early spike under the normal sodium channel density ($0.24 S/cm^2$). Increasing the sodium channel density in the AIS does not affect the AP shape (figure 3.27 A), but an earlier peak time is observed (figure 3.27 B). Decreasing the density also delays the time of the peak. At $g_{Na^+} = 0.17 S/cm^2$ (30% reduction of the default density), the transition between a late spike (figure 3.27 C) and an early spike (figure 3.27 D) occurs. This transition is marked not only by the initiation site by also by the jump between peak times (figure 3.27 B). Finally, very low sodium densities in the AIS prevent the ectopic action potential from propagating to the soma. Instead, a widened bump can be recorded (figure 3.27 A). In summary, modulation of early spikes is also dependent on the AIS intrinsic excitability.

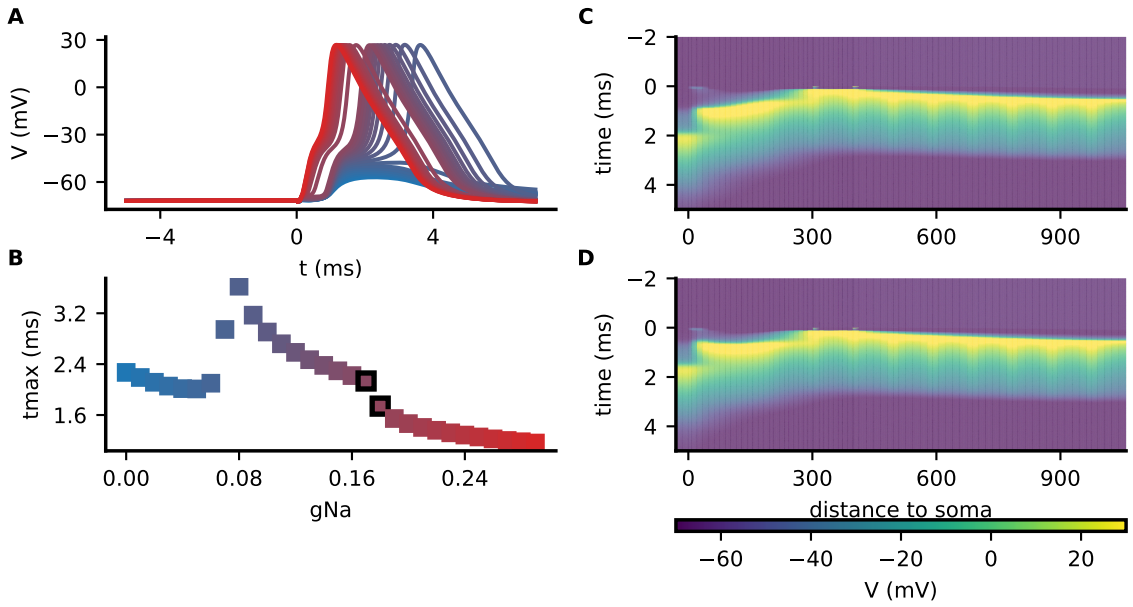

Figure 3.27: AIS sodium channel density can switch between late and early spikes (A) Membrane potential at soma responding to same stimulus for various AIS sodium channel densities (red highest and blue lowest) (B) Time of peak of trace as a function of sodium channel density in the AIS shows failed spikes (left), late spikes (middle) and early spikes (right). The color scale is the same as in (A). (C), (D) Position-time color plots of AP initiation for low sodium channel ((C), left black square on (B)) and high ((D), right black square on (B)) to show differential initiation sites

4 Discussion

4.1 The instantaneous time constant and the biophysics of the membrane

The main aim of this thesis was to measure the excitatory synaptic inputs onto pyramidal cells with the aim of simultaneously measuring the depolarization experienced by the neuron and the currents which drive that depolarization. To that aim, a new magnitude is proposed, the instantaneous time constant, $\tau\star$. This new magnitude follows the intention of expressing excitatory input in terms of a simple magnitude, the time constant. In this manner, excitatory inputs can be seen by its two main features. First the presence of a driving force to depolarize the neuron. Second, a change in the passive properties (i.e., the time constant). This approach has been used to the time constant of shunting (Schiller and Schiller, 2001; Dayan and Abbott, 2005). As the time constant is a magnitude that speaks for the integrating rate, a reduction of its value is to increase the integrating speed and therefore contribute to the integration. Furthermore, as a well established magnitude within the physiology, yields values that are easy to interpret. The change in passive properties by synaptic input has been dealt in (Gidon and Segev, 2012), where off-path inhibition changed the membrane in a way that dampened more effectively synaptic input than in-path. As opposed to that study, I have focused on the excitatory effect inputs exert on those changes in passive properties. The distance dependent behavior has also been studied. As shown in (Jaffe and Carnevale, 1999), excitatory inputs onto apical dendrites of CA1 pyramidal c ells exhibit a distance decay. Although in their study they only focused on amplitudes, the capacitive term of the impedance causes the widening of the EPSP shape as well as the reduction of its amplitude. Corrections of this widening are beyond the scope of this study.

Regarding the ionic currents, the current clamp setting does not allow to disregard them with the same confidence as in voltage clamp. The linear behavior of the mem-

brane at potentials close to the resting membrane potential is ubiquitous (Rall, 1960; Koch et al., 1990; Gidon and Segev, 2012). To ensure that the linearity is maintained, the frequency of the sinusoidal was chosen to 10Hz, higher than the resonance of I_h current ($1 - 2Hz$,(Hutcheon and Yarom, 2000)) to avoid interferences from this resonance. Moreover, maximum depolarizations (including sinusoidal and EPSP components) being below $-55mV$ make it unlikely that sodium (Magee and Johnston, 1995; Hoffman et al., 1997), calcium (Jaffe et al., 1994; Magee and Johnston, 1995) or NMDA (Schiller and Schiller, 2001) conductances are active. Moreover, APV was applied to the recordings for blocking of NMDA receptors.

4.1.1 Measurements of conductances

I have covered in the previous sections the formalism regarding single compartment passive neurons, both for excitation and inhibition. Although this model, with the addition of a binary action potential (integrate and fire neurons) is reliable to describe the basic cell physiology, as has been widely used to model its behavior (Dayan and Abbott, 2005), it presents some limitations with respect to others with more sophisticated morphologic and biophysical models.

The main assumptions that they have been made are the following: First, it is possible to elicit trials that are identical except in the phase of the oscillation, disregarding effects of synaptic variability and recording noise. Second, that the membrane remains in the linear regime without the presents of non tonic conductances and thus the neuron can be described as a RC circuit. Third, that the propagation of EPSPs along the dendrites, although has a well known attenuation does not prevent the method from working. All these assumptions will be checked during the experiments and then commented in the discussion.

Neurons receive most of their synaptic input via their dendrites, from where they are propagated to the soma, where the main integration of the inputs takes place. As explained in the introduction, during this propagation process, the transmission of the signals is attenuated due to the cable properties of the dendrites (Rall, 1970).

Therefore, it is necessary to assert to which extent this attenuation or distortion will affect the instantaneous time constant. Starting from the schematic dendritic compartment described in section 1.2.2

In order to calculate the value of $\tau\star$ at a give point of the synaptic input, the values

of the three electrical magnitudes, I, V, and $\frac{dV}{dt}$ need to be measured. Nevertheless, it is not enough to determine three parameters with only three magnitudes. To overcome that, a small sinusoidal oscillation is used.

Sinusoidal oscillations have been classically used in electrophysiology to measure impedance changes from the phase delay (Van Oosterom et al., 1979; Ferreira-Filho and Martins-Ferreira, 1982). Also, they have been used in neurons to measure frequencies of resonance (Hutcheon and Yarom, 2000; Zemankovics et al., 2010). The limitation of this approach is that the timings to be measured need to be slower than the frequency applied. Therefore, to measure synaptic kinetics in the order of milliseconds, applied frequencies in the order of KHz would be expected. However, it is known that the impedance at those frequencies is much higher than at lower frequencies (Zemankovics et al., 2010; Jaffe and Carnevale, 1999), thus making the voltage variation too small to measure. The approach taken in this study is to assume that the synaptic input elicited at each stimulation is comparable to the other. This assumption is reasonable as it is the standard approach to average EPSCs in voltage clamp to reduce the noise (Numberger and Draguhn, 1996). From there, a larger set of points $I, V, \frac{dV}{dt}$ are available for fitting the equation and thus obtaining $\tau\star$. The amplitude apply needs to be small enough to ensure that the linear regime is maintained (Dayan and Abbott, 2005), yet greater so that it is greater than the noise. For the experiments, amplitudes around $3-4mV$ were sufficient to clearly see the oscillation, while not being big enough to cause a difference in amplitudes of EPSPs of different phases.

Another approach taken theoretically is to assume that $\tau_{membrane} >> \tau syn$. With that, the currents due to the membrane time constant can be considered decoupled (Koch et al., 1990). As the time constant for CA1 pyramidal neurons is one order of magnitude bigger than the dynamics of AMPA receptors (Wheeler et al., 2015). Therefore, the assumption that during the synaptic input, the membrane constant is too slow to cause an effect must be taken with care.

Other methods to estimate conductance changes have been proposed, such as (Borg-Graham et al., 1998; Häusser and Roth, 1997).

In his work, Borg-Graham provided a method to calculate the conductance changes during visual tasks of a cat. Data was collected from VC recordings at four different holding potentials under the same sensory stimulus. Based on Ohm's law, the conductance is estimated as a function of time, and also an effective reversal potential is estimated. In that study, they claim the same procedure can be applied to current

clamp recordings, though it brings two problems. The first one is the presence of capacitive currents, which are slower than synaptic ones; and the second one is the plausible presence of ionic currents. Using $\tau\star$ and the sinusoidal current approach, the capacitive currents are integrated in the model so that their action does not blur the obtention of the conductance. Other active currents are not accounted for and the assumption is that in the voltage ranges applied, the linear regime remains. This assumption has been often taken (Poirazi and Mel, 2001). Nevertheless, the main drawback between $\tau\star$ and the method of Borg-Graham is that it only applies to excitatory synaptic inputs, as opposed to both excitatory and inhibitory synaptic inputs.

Another very powerful method is the one presented in (Häusser and Roth, 1997). Combining voltage jumps at different timings with respect to the synaptic stimulation in voltage clamp, they estimated the kinetics of the synaptic input. In addition, this method can also estimate the timing delay due to the space clamp problem (Armstrong and Gilly, 1992). Despite the great accuracy of this procedure, the two main drawbacks procedure are the lack of a value of the conductance magnitude and that to obtain the kinetics, an a-priori waveform is to be provided. $\tau\star$, on the other hand, provides an estimate of the magnitude due to the change in the instantaneous time constant. In the case of a single compartment neuron, the value of the conductance can be directly estimated from the input resistance. In the case or a real neuron or a multicompartment model there is no analytic relation. Nevertheless, they are proportional and thus relative weights can be compared. Furthermore, $\tau\star$, within its biases, retrieves the waveform of the excitatory conductance, without any a-priori shape needed.

The estimation of conductances changes through the instantaneous time constant conveys two main challenges, one of theoretical nature, and one recording problem. In a neuron with morphology, not only the transmembrane currents are present, which are the only ones accounted in the model. There is another internal current, which equalizes the membrane potential across the neuron. (Rall, 1969). A method to characterize these currents is to include several time constants, calculating the next, larger, after substracting the component of the previous in "peeling" process (Holmes et al., 1992). As the model presented here only includes the greatest contribution, i.e., the capacitive current, the fitting process has a bias that leads to $\tau\star$ underestimating the kinetics of the conductances. An analytical compensation term may be possible but it is beyond the scope of this study. Another approach would be to take this bias and use it, along with EPSC recordings to measure the electrotonic length of a particular synaptic input.

The greatest technical caveat present in this study is the importance of obtaining a reliable value of the derivative of the membrane potential. By extending the classical ohmic treatment of the cell to include directly the capacitive currents, the role the derivative plays in the model is analogous to the membrane potential. However, this magnitude can only be obtained by deriving the trace of the membrane potential. In this process, the noise inherent to any recording is amplified, as the derivative deals with the local differences, and these are noise. Smoothing processes are not desirable as they low pass the data, and therefore some of the fast-timing information of the conductances may be lost. Additionally, it was mentioned above that the amplitude of the sinusoidal needs to stand out from the noise. This is also necessary for the derivative, requiring either high SNR recordings or increasing the amplitude of the sinusoidal which, in turn, may push the membrane outside of the linear regime. The variational technique applied in this study (Chartrand, 2011b), which tries to find a function where smoothness and similarity to the derivative are balanced. This solution obtained satisfactory readouts of $\tau\star$, which are comparable to the post synaptic currents recorded in voltage clamp. Still, the noise in the derivative remains the single greatest source of error for the calculation, especially on experimental data.

In summary, $\tau\star$ with the aid of sinusoidal current injections can estimate both the waveform and magnitude of excitatory conductances, yet the morphology and the subsequent space clamp problem creates a bias towards the underestimation of the values with respect to analogous recordings of excitatory post synaptic currents in voltage clamp.

4.1.2 Integration of EPSPs

The current understanding of integration of excitatory signals shows that there is a range of low depolarizations in which inputs are integrated more or less linearly, followed by larger depolarizations, in which the inputs are added supralinearly aided by active conductances (Poirazi and Mel, 2001; Remy et al., 2009; Thome et al., 2014). Under the linear regime, inputs are assumed to follow the passive properties of the membrane. However, Rall postulated that a depolarization may significantly reduce the driving force of excitatory potentials and thus, reduce the total depolarization sublinearly (Rall, 1969). More recently, computational characterization showed that under particular morphologies, such as CA1 pyramidal cells, synapses act as current sources and thus not affected by the change in driving force (Jaffe and Carnevale, 1999). Active

conductances may however play a role in maintaining the linear regime (Cash and Yuste, 1999). A major challenge is that small active currents may contribute at the dendritic location but remain invisible in the soma (Spruston et al., 1994).

Besides, the time coupling is crucial for synaptic integration. Precise patterns of excitation and inhibition are fundamental for the sustainment of network oscillations and overall brain function (Buzsáki and Draguhn, 2004). Furthermore, cortical neurons can encode synaptic stimuli into action potentials in the millisecond timescale (Tchumatchenko et al., 2011; Huang et al., 2012). In contrast, many presynaptic processes are stochastic such as neurotransmitter release, diffusion or binding to receptor. Thus, it is necessary that neurons have mechanisms to promote the synchrony of their inputs.

Regarding the case timing differences between two excitatory inputs, the theoretical prediction is that the total peak amplitude decreases monotonically as the inputs desynchronize (Rall, 1970). Evidence on this prediction is contradictory, with one study showing sublinear integration for coincident events for oriens and apical stimulation of CA1 pyramidal cells (Cash and Yuste, 1999) and other showing supralinear integration in a window of 10 ms and a sublinear window between 10 and $50ms$ (Margulis and Tang, 1998). Both studies were carried out in hippocampal cultures.

In (Cash and Yuste, 1999) the experimental design follow the works of Rall (Rall, 1964) and the authors were expecting a 40% sublinearity due to the reduced driving force and the shunting caused by the reduction of the input resistance. However, the peaks of their EPSPs were $10mV$, thus not far away from the resting membrane potential and also, as shown in chapter 3.1, the shunting effect of excitation changes also the effective reversal potential and thus may enhance the integration. This is consistent with the computational experiments shown in section 3.2.2.

Furthermore the supralinearity for the $10ms$ window shown in (Margulis and Tang, 1998) was attributed to an sodium currents. TTX application and voltage clamp recordings at $-45mV$ to inactivate sodium channels both showed that the supralinearity was attenuated. Although other active currents like calcium or NMDA are be involved, these results also suggest that the overlap of conductances may play a role in enhancing coinciding integration.

In summary, conductance overlap and the subsequent change of the time constant might be a mechanisms by which inputs close to synchrony are rewarded in depolarizations below the threshold of activation of ionic channels or NMDA receptors.

4.1.3 Extension to inhibition

In the previous sections, the behavior of $\tau\star$for excitatory synaptic input has been considered. The underlying principle is that there are two competing forces in the membrane. The first one is the tendency of the membrane to its resting potential, which can be considered constant in time and the second is the force towards depolarization driven by excitation, whose reversal potential is $0mV$ (Hestrin et al., 1990). Taken together, this allows to synthesize all conductance behavior into a single magnitude, the instantaneous time constant.

However, inhibition and its interplay with excitation is fundamental for synaptic integration (Hao et al., 2009), precise action potential timing (Tchumatchenko et al., 2011) and maintaning network state (Buzsáki and Wang, 2012). Therefore, obtaining a readout of inhibitory conductances along with excitation is a crucial issue to measure a working neuron.

This poses an addition of complexity. As opposed to the case where only excitation is considered, here there are three forces acting together. Inhibition, like excitation, is time dependent and its reversal potential is close to the resting potential (Huguenard and Alger, 1986). Thus, the effect of inhibition is mainly shunting rather than hyperpolarizing (Schiller and Schiller, 2001). With inhibition included, the changes in the membrane cannot be reduced to a single parameter, like $\tau\star$, but the combination of a time constant and an effective reversal potential (Dayan and Abbott, 2005; Borg-Graham et al., 1998). After this step, the effects of conductances cannot be summarized into a single parameter. Thus, no clear analogy to a basic passive element can be made, as with the time constant and excitatory synaptic input. A study of the combined effects of shunting and effective reversal potential can start from this point and might be subject of further study.

4.1.4 Calculation of conductances during network oscillations

As explained in the previous section, in order to account for inhibitory input, the single parameter of the instantaneous time constant can no longer be used. Nevertheless, the approach of applying a sinusoidal current injection via a patch pippete or a sharp electrode can still be used.

Sharp wave ripples are high frequency oscillation events present in vivo in spatial

navigation (Singer et al., 2013) and memory formation (Buzsáki, 1989) tasks. The have been reproduced in vitro setting (Maier et al., 2003; Both et al., 2008) which is a better setting to test their underlying mechanisms.

The construction of a deep learning model was able to reliably recover conductances for test data without noise. However, when trial to trial variability and gaussian noise was added, the calculated values of the excitatory and inhibitory conductances were underestimated by 50%.

Additionally, the loss in the experimental did not converge satisfactorily. Estimates reproduce two main features of conductances during SPW. First, excitation arrives first, followed by a strong inhibition. Second, the ratio of inhibition to excitation is 5, consistent with other measurements. Finally, the value of the measured conductances is in range with other measures (Maier et al., 2011). Nevertheless, as the procedure has shown to underestimate the values of the conductances, these calculated conductances must be taken with care.

What can be done from the experimental point of view to improve the data processing? First, all deep learning applications rely of big datasets to extract the main features (Goodfellow et al., 2016). As the recordings where made during 10 minutes, with $3Hz$ event frequency, and many where discarded due to quality criteria. It is noteworthy to mention that, although the emergence of sharp wave ripples is random, the events fell well distributed withing the face of the sinusoidal, which helps for the analysis.

Another major concern is the resting membrane potential. The recordings analyzed were taken at $-80mV$ membrane potential, below the reversal potential of inhibition. To better discern between excitation and inhibition, recordings should be taken at membrane potentials above the reversal chloride potential.

Deep learning approach

The linear model has failed to retrieve the conductances during network oscillations. This failure has many causes. First, the original linear model does not user an inhibitory component. Once included this inhibitory conductance coexists along with the excitatory. This means that for every time point, two values exist ($g_{exc}(t)$ and $g_{inh}(t)$). This makes the solutions unstable, as a variation in one of the conductances, can be overcome by an opposite change in the other. This leads to ovefitting and, indirectly, to more noise (or the higher SNR measured in the previous section).

In general, the linear model provides the best minimization at each time point, regardless of previous parameters. Basic electrophysiological and biophysical already gives us some information about the nature of the solution that the linear model cannot include. First of all, by definition, both values of $g_{exc}(t)$ and $g_{inh}(t)$ are always positive. Secondly, if we assume that the conductance outside the ripple is tonic, then all conductances in the baseline are incorporated into the leakage and thus $g_{exc}(t)$ and $g_{inh}(t)$ are zero (or close to it). Also, the conductances are assumed to be smooth, i.e., without sharp edges and with low signal to noise ratio.

Some non-linear minimization techniques could be used like the Levemberg-Marquardt algorithm ((Levemberg, 1944; Moré, 1978)). Furthermore, deep learning has emerged lately (Goodfellow et al., 2016) as a widely used technique for extracting underlying information from patterns, with applications mostly developped in classificaction tasks such as object or speech recognition.

As the complexitity addition of inhibition makes the model untractable for the linear minimization, a deep learning approach was taken. Deep learning consists of creating representations of a data set through an artificial neural network. The term of artificial neuron comes from its origins, where networks were designed to resemble real neural networks such as a model of the visual cortex to image pattern recognition (Fukushima, 1988). However, in more recent times, due to lack of a full understanding of neuroscientific neural networks, its design has diverged towards the field of engineering (Goodfellow et al., 2016). They have industrial applications in finance, natural language processing, computer vision or speech recognition (Deng et al., 2014).

The quintessential dataset for deep learning is the MNIST (LeCun et al., 2010), a collection of images of handwritten digits. Most of the literature in the field assesses the efficacy of the method by how well the digits can be classified. Although application of deep methods to regression (a continuous function as output) is possible, there is lesser literature on this field than in classification.

Usually in deep learning models, the output of the last layer is the magnitude to predict. The predicted value is compared against the measured value and the difference is the loss by which the network is optimized. With our datasest, the (normalized) time was used as input, and the output was the time dependent values of the conductances and the constant passive parameters and reversal potentials. This output, along with the membrane magnitudes for each timepoint ($I, V, \frac{dV}{dt}$) was applied to equation 3.17, which acted as the loss function. This network was designed in that way so that the

magnitudes to be predicted (excitatory and inhibitory conductances) appear explicitly in the model. Furthermore, using two recorded quantities (from $(I, V, \frac{dV}{dt})$) as input as the remaining one as output has the problem that the network may try to minimize based on basic electrical properties. For instance, if the derivative is the output, by learning to derive the membrane potential trace, a good minimization is achieved.

When training deep networks, a validation set is needed to prevent overfitting. This means that the network should generalize beyond the training set and not only memorize the given data (Goodfellow et al., 2016). The usual procedure is to leave a subset of the total data outside of the training and then measure the performance of the trained network with it. Given the nature of the data, where a sinusoidal waveform was applied and the goal being to see the behavior in the absence of the sinusoidal, the validation set used here was the average across trials.

For the optimization algorithm chosen to train the network, stochastic gradient descent is the simplest implementation, which consists of update the weights according to the direction of maximum gradient for a subsample of the dataset (Goodfellow et al., 2016). This algorithm, however, has been proven poor on deep networks, as the gradients on the deepest networks tend to become smaller and smaller (Goodfellow et al., 2016). Recently, more sophisticated algorithms have been introduced. I tried all the optimization algorithms available in the keras library (Chollet and others, 2015). Among them, Adam (Kingma and Ba, 2014) and Adadelta (Zeiler, 2012) were the most succesful for this optimization problem.

When designing the network, a key requirement was for the network to yield time dependent outputs (the conductances) as well as constants (the passive parameters and the reversal potentials). This was implemented by having a part of the network input-independent. This decission was made to remain with within the simpler feed forward networks framework. More sophisticated solutions would have been possible, such as long short term memory units (LSTMs) (Gers et al., 1999), although they are more complicated to optimize (Goodfellow et al., 2016).

Another possible approach would be to measure an effective conductance and effective reversal potential (Dayan and Abbott, 2005; Borg-Graham et al., 1998). With these magnitudes, excitation and inhibition could be inferred by independent component analysis (ICA) (Hyvärinen and Oja, 2000). This approach, informally known as the *cocktail party problem*, consists of extracting the most statisctically independent components that form a set of signals, like the voices of different people from the background

sound of a gathering. ICA has been successfully used for disentangling signals from different pathways in the hippocampus (Makarov et al., 2010; Makarova et al., 2011; Martín-Vázquez et al., 2015). In the case study of SPW-r, this approach is not feasible. Firstly, the connectivity between pyramidal cells and intereurons in the CA1 area (Andersen, 2007a) suggests that the excitatory and inhibitory input are not statistically independent. Secondly, ICA can only disentangle up to a constant. In this case, it means that the waveform of the conductances can be detected, but its magnitude could be smaller or bigger by having a bigger or smaller reversal potential. Thus, either a value of the reversal potential needs to be given a priori, or no solution can be reached.

Finally, the deep network constructed so far only reflects the passive conductances of sharp wave ripples. Noise minimization and the addition of elements inside the network to account for active mechanisms might reduce the error and thus infer the behavior of conductances during sharp wave ripples.

4.2 AcD input and output

A recent study has found that the axon of around 50% of CA1 pyramidal cells emanates from a basal dendrite, rather than from the soma (Thome et al., 2014). Moreover, electrophysiology experiments show that synapses onto these axon carrying dendrites elicit more efficiently action potentials (Thome et al., 2014). The computational study made during this thesis complements and enlarges our understanding of this phenomenon.

From the two port theory framework presented in (Jaffe and Carnevale, 1999), the transmission of post synaptic potentials from their initiation site to other neuronal regions can be seen in two ways: either a depolarization is caused at the synapse site and this depolarization is transfered to other regions via the voltage transfer ratio ($V_B = k_{A\to B}V_A$) or the current entering at the synapse is propagated towards the target region in term of the tranfer impedance ($V_B = Z_c I_A$). The computational characterization of this study shows that CA1 pyramidal cells can be better represented by transfer impedance than by voltage ratio. In this framework, nonAcD inputs must traverse the soma in order to reach the AIS. Due to the large surface (and thus capacity) to the soma, the transfer impedance from nonAcD to soma is higher than the equivalent from AcD to AIS, and thus total depolarization elicited in the AIS is greater for the same input if it is coming from the AcD.

AIS location within the axon is plastic and its location modulates overall neuronal excitability (Grubb and Burrone, 2010). A change of location of AIS is thought to homeostatically regulate somatic AP (Hamada et al., 2016). This homeostatic modulation accounts for nonAcD inputs, whereas AcD inputs would be affected to a lesser extend by this reallocation of the AIS.

The computational model also predicts that perisomatic inhibition is innocuous to AcD input for AP generation. Intrincated patterns of excitation and inhibition are crucial for the sustainment of network oscillations. In each oscillation type different types of interneurons provide specific kinds of inhibition (Klausberger et al., 2003; Klausberger and Somogyi, 2008). Therefore having an input insensible to the ongoing perisomatic inhibition of basket cells might contribute to switching from one network state to another in a context of high perisomatic inhibition. Experimental support for this hypothesis is needed. On the other hand, it has recently been proposed that off-path inhibition might shunt more efficiently than on-path (Gidon and Segev, 2012). As that prediction is based on the end conditions of dendrites, this off-path inhibition is most likely to act in dendrites and thus, the off-path effect exerted by perisomatic inhibition to AcD input is sharply reduced, as the simulations show. Inhibition in the AIS mediated by chandelier cells, on the other hand, is not likely to be different.

Finally, the higher propensity of dendritic spikes in AcD branches cannot be explained by the morphology. Indeed, the electrotonic properties of AcD and the control nonAcD are the same. Active mechanisms in dendritic signaling are important for generating dendritic spikes, either trough sodium, calcium (Jaffe et al., 1994; Magee and Johnston, 1995) or NMDA (Schiller and Schiller, 2001) receptors.

4.3 Long range synaptic interaction in the axon

Ectopic action potentials (eAPs) in CA1 pyramidal cells are present in epileptic form activity (Velazquez and Carlen, 2000). Spikelets suggesting the presence of AP in the axon have been reported in vivo (Epsztein et al., 2010). The presence of gap junctions is necessary for the maintenance of SPW-r in vivo (Maier et al., 2003), despite evicence in vivo is yet to come. Due to the sparsity of pyramidal to pyramidal synaptic connections (Andersen, 2007b), gap junctions and their generated eAP have been proposed as a mechanism for excitatory cells synchrony during SPW-r (Traub et al., 2012; Vladimirov et al., 2013).

Our computer simulations reproduce the bimodal pattern of eAPs seen in the electrophysiological experiments. Careful inspection to the axon-wide waveforms confirmed the hypothesis that the late spikes are initiated in a node of ranvier, whereas the early spikes are initiated in the AIS. This is probably due to their high concenctration of sodium channels which makes them These the most excitable sites of the axon.

Furthermore, the simulations confirm the coupling between synaptic input and eAP generation. The first node of ranvier is located $250\mu m$ away from the soma. Thus the distance between synapses proximal to the soma and the node is well below the space constant ($\lambda = 612\mu m$, (Koch et al., 1990)). Thus, those PSPs arrive at the node with enough amplitude to modify the membrane potential of the node. Furthermore, the correlation between membrane potential and input necessary to trigger an eAP was maximum in the node for late spikes and the AIS for early spikes. As the axon is electrotonically connected, the correlation will be present throughout the axon. However, the place with the highest correlation is the most likely where the interaction is present, whereas the correlation of other sites comes from the axial propagation of PSPs. This interaction is indirect, and thus the correlation is reduced.

The threshold of action potential activation shown in the study refers to either the generation of an eAP in the node, or the generation of of two eAP, in the node and in the AIS. There was no case in which a spike would be generated in the node and, due to large inhibition in the AIS, had its backpropagation blocked to reach the soma. This is consistent with experiments on rats (Fabian Roth, personal observation). Back propagating action potentials are important to depolarize the dendritic compartments after the AP generation (Nevian et al., 2007) and may be important in providing feedback for mechanisms of hebbian plasticity (Hebb, 1949).

To sum up, the long range passive propagation of postsynaptic potentials can couple to active sodium channels in the enriched nodes of ranvier or AIS to generate AP. This may interact with gap junctions to generate eAPs.

4.4 Future Experiments

One of the complications of using the instantaneous time constant to measure excitatory conductances is the difficulty of knowing the real value of the post synaptic current in experimental conditions. Double patching of the soma and an apical dendrite could

be a solution to this problem: The dendritic patch could inject current pulses of the shape of an EPSC and the same waveform could be repeated several times with minimal trial to trial variability. Then, the somatic patch could measure the instantaneous time constant. Finally, the electrotonic distance between the applied pulse and the somatic recording could be easily determined via the two patches.

Another approach to improve the reliability of the incoming post synaptic current to assess the quality of the instantaneous time constant would be dynamic clamp (Robinson and Kawai, 1993). With this technique, a single patch pippete in the soma would produce the incoming waveform and the sinusoidal current to detect it. Some theoretical analysis would be needed beforehand, to ensure that the principles under which dynamic clamp works are not altered by adding a sinusoidal current within the same pippete.

The deep learning network proposed in this thesis has produced preliminary results with the obtention of the conductances during network oscillations. A better design is however needed to reliably estimate the values and time courses of the conductances. Long short term memory units (LSTMs) (Hochreiter and Schmidhuber, 1997) are a type of artificial neurons that not only apply a nonlinearity onto the input to produce the output but also combine it with a memory of past events. Using these neurons as building blocks of the artificial neural network could help to store the time information of the conductances and thus improve the algorithm.

Nevertheless, the successful application of a deep learning algorithm deeply relies on the quality of the input dataset. To improve the quality of the network oscillations recorings, a preprocessing step could be added to classify the sharp wave ripples into alike categories (Reichinnek et al., 2010). These alike categories could be used in different instances of the deep learning network and thus each network would have less variability and the conductances could be better estimated.

Acknowledgments

I would firstly like to thank Andreas Draguhn, who has been my guide all these years. He gave me the opportunity to become a neuroscientist in his lab and has supported me with his ideas and also with the freedom to pursue my own questions. My gratitude goes also to Martin Both, who supervised the day to day work and whose insights helped me from the beginning. Thanks also to Alexei Egorov for the endless (not always on the good sense) discussions we have had to bring the biophysical modeling and the physiology closer together. I am very thankful to Rafael Gutiérrez and Stephan Remy, who opened their labs to me and let me work, learn and enrich with experiences and discussions.

The lab is much more than a bunch of senior scientists, and I was lucky to live in one I thank to Susanne being always ready to help and enjoy a conversation, either in her office or in the *Handschuhsheimer Kerwe*. To Nadine, Katja and Lee, who were most kind and supportive with their expertise. To Claus, for all the technical knowledge and german culture that has transmitted to me. Thanks to the other Phd companions for the common environment, and the sharing of personal and professional experiences: Suse, Valandis, Fabian, Greg, Pascal, Vivan, Wei Wei, MK and Jan-Oli and above all Jana. Indeed life is beautiful. Thanks to Christian, for sharing lab and home and whose ideas are behind much of the work of this thesis. And also to Federica, my youngest boss. Special thanks to Xiao Min and Ismini, good friends over the distance and my first inspirations in the lab. Also, a long list of master students shared the time with me, and my gratitude goes to them. Specially to Timm Hondrich, with whom the idea of the instantaneous time constant first came up.

A good life-science balance is fundamental for a healthy life. Thus, my gratitude goes to the people outside the scientific community that have contributed to my mental health. Thanks to Rainer, and all the other people with whom I have lived, for the memories. Thanks to the *Fodenheim* group for the adventures and specially thanks to the *Komando alcantarillas*. May another May come! Distance has proven difficult to

maintain the strong friendships from my former life in Galicia. My long distance apology and gratitude towards your patience.

To my parents for their love and tenacity so that I could finish my phd and to my sister, who despite being younger than me became a doctor before me. And to the rest of my family for their love and support. To Janet, the greatest discovery done during the thesis. We are a good team.

Last, to the "la Caixa" foundation who together with DAAD funded the first stage of this study and to the SFB 1134, who did afterwards.

Bibliography

Andersen P (2007a) *The Hippocampus Book* Oxford University Press, USA Google-Books-ID: IQkTDAAAQBAJ.

Andersen P (2007b) *The hippocampus book* Oxford University Press.

Anderson P, Storm J, Wheal H (1987) Thresholds of action potentials evoked by synapses on the dendrites of pyramidal cells in the rat hippocampus in vitro. *The Journal of physiology* 383:509–526.

Armstrong CM, Gilly WF (1992) [5] access resistance and space clamp problems associated with whole-cell patch clamping. *Methods in enzymology* 207:100–122.

Bähner F, Weiss EK, Birke G, Maier N, Schmitz D, Rudolph U, Frotscher M, Traub RD, Both M, Draguhn A (2011) Cellular correlate of assembly formation in oscillating hippocampal networks in vitro. *Proc Natl Acad Sci U S A* 108:E607–E616.

Baranauskas G, David Y, Fleidervish IA (2013) Spatial mismatch between the na+ flux and spike initiation in axon initial segment. *Proceedings of the National Academy of Sciences* 110:4051–4056.

Borg-Graham LJ, Monier C, Frégnac Y (1998) Visual input evokes transient and strong shunting inhibition in visual cortical neurons. *Nature* 393:369–373.

Both M, Bähner F, von Bohlen und Halbach O, Draguhn A (2008) Propagation of specific network patterns through the mouse hippocampus. *Hippocampus* 18:899–908.

Brette R, Destexhe A (2012) *Handbook of neural activity measurement* Cambridge University Press.

Buzsáki G (1989) Two-stage model of memory trace formation: a role for noisy brain states. *Neuroscience* 31:551–570.

Buzsáki G, Draguhn A (2004) Neuronal oscillations in cortical networks. *Science* 304:1926–1929.

Buzsáki G, Wang XJ (2012) Mechanisms of gamma oscillations. *Annual review of neuroscience* 35:203–225.

Carnevale NT, Hines ML (2006) *The NEURON book* Cambridge University Press.

Cash S, Yuste R (1999) Linear summation of excitatory inputs by ca1 pyramidal neurons. *Neuron* 22:383–394.

Catterall WA, Raman IM, Robinson HPC, Sejnowski TJ, Paulsen O (2012) The hodgkin-huxley heritage: From channels to circuits. *J. Neurosci.* 32:14064–14073.

Chartrand R (2011a) Numerical differentiation of noisy, nonsmooth data. *ISRN Applied Mathematics* 2011.

Chartrand R (2011b) Numerical differentiation of noisy, nonsmooth data 2011.

Chollet F et al. (2015) Keras.

Cutsuridis V, Cobb S, Graham BP (2010) Encoding and retrieval in a model of the hippocampal ca1 microcircuit. *Hippocampus* 20:423–446.

Dayan P, Abbott LF (2005) *Theoretical Neuroscience: Computational and Mathematical Modeling of Neural Systems* The MIT Press.

Deng L, Yu D et al. (2014) Deep learning: methods and applications. *Foundations and Trends® in Signal Processing* 7:197–387.

Dingledine R, Langmoen IA (1980) Conductance changes and inhibitory actions of hippocampal recurrent ipsps. *Brain Research* 185:277–287.

Epsztein J, Lee AK, Chorev E, Brecht M (2010) Impact of spikelets on hippocampal ca1 pyramidal cell activity during spatial exploration. *Science* 327:474–477.

Ferreira-Filho CR, Martins-Ferreira H (1982) Electrical impedance of isolated retina and its changes during spreading depression 7:3231–3239.

Fukushima K (1988) Neocognitron: A hierarchical neural network capable of visual pattern recognition. *Neural networks* 1:119–130.

Gasparini S, Magee JC (2006) State-dependent dendritic computation in hippocampal CA1 pyramidal neurons 26:2088–2100.

Gers FA, Schmidhuber J, Cummins F (1999) Learning to forget: Continual prediction with lstm .

Gidon A, Segev I (2012) Principles governing the operation of synaptic inhibition in

dendrites. *Neuron* 75:330–341.

Goldman DE (1943) Potential, impedance, and rectification in membranes. *The Journal of general physiology* 27:37–60.

Goodfellow I, Bengio Y, Courville A (2016) Deep learning. book in preparation for mit press. *URL¡ http://www. deeplearningbook. org* .

Grubb MS, Burrone J (2010) Channelrhodopsin-2 localised to the axon initial segment. *PLoS One* 5:e13761.

Hamada MS, Goethals S, de Vries SI, Brette R, Kole MH (2016) Covariation of axon initial segment location and dendritic tree normalizes the somatic action potential. *Proceedings of the National Academy of Sciences* p. 201607548.

Hao J, Wang Xd, Dan Y, Poo Mm, Zhang Xh (2009) An arithmetic rule for spatial summation of excitatory and inhibitory inputs in pyramidal neurons. *Proc Natl Acad Sci U S A* 106:21906–21911.

Häusser M, Roth A (1997) Estimating the time course of the excitatory synaptic conductance in neocortical pyramidal cells using a novel voltage jump method. *J Neurosci* 17:7606–7625.

Hebb DO (1949) *The organization of behavior: A neuropsychological approach* John Wiley & Sons.

Hestrin S, Nicoll RA, Perkel DJ, Sah P (1990) Analysis of excitatory synaptic action in pyramidal cells using whole-cell recording from rat hippocampal slices. *J Physiol* 422:203–225.

Hille B (2001) *Ion channels of exitable membranes* Sinauer.

Hines M (1984) Efficient computation of branched nerve equations. *Int J Biomed Comput.* 15:69–76.

Hines ML, Davison AP, Muller E (2009) Neuron and python. *Front Neuroinform* 3:1.

Hines M, Moore J (1997) Computer simulations with neuron. *Duke University* .

Hochreiter S (1998) The vanishing gradient problem during learning recurrent neural nets and problem solutions. *International Journal of Uncertainty, Fuzziness and Knowledge-Based Systems* 6:107–116.

Hochreiter S, Schmidhuber J (1997) Long short-term memory. *Neural computation* 9:1735–1780.

Hodgkin AL, Huxley AF (1952) A quantitative description of membrane current and its application to conduction and excitation in nerve. *J. Physiol.* 117:500–544.

Hodgkin AL, Katz B (1949) The effect of sodium ions on the electrical activity of the giant axon of the squid. *The Journal of physiology* 108:37–77.

Hoffman DA, Magee JC, Colbert CM, Johnston D (1997) K+ channel regulation of signal propagation in dendrites of hippocampal pyramidal neurons. *Nature* 387:869.

Holmes WR, Segev I, Rall W (1992) Interpretation of time constant and electrotonic length estimates in multicylinder or branched neuronal structures. *J Neurophysiol* 68:1401–1420.

Hu W, Tian C, Li T, Yang M, Hou H, Shu Y (2009) Distinct contributions of na(v)1.6 and na(v)1.2 in action potential initiation and backpropagation. *Nat Neurosci* 12:996–1002.

Huang M, Volgushev M, Wolf F (2012) A small fraction of strongly cooperative sodium channels boosts neuronal encoding of high frequencies. *PLoS One* 7:e37629.

Huguenard JR, Alger BE (1986) Whole-cell voltage-clamp study of the fading of GABA-activated currents in acutely dissociated hippocampal neurons 56:1–18.

Hunter JD (2007) Matplotlib: A 2d graphics environment. *Computing In Science & Engineering* 9:90–95.

Hutcheon B, Yarom Y (2000) Resonance, oscillation and the intrinsic frequency preferences of neurons. *Trends Neurosci* 23:216–222.

Hyvärinen A, Oja E (2000) Independent component analysis: algorithms and applications. *Neural networks* 13:411–430.

Ishizuka N, Cowan WM, Amaral DG (1995) A quantitative analysis of the dendritic organization of pyramidal cells in the rat hippocampus. *Journal of Comparative Neurology* 362:17–45.

Jaffe DB, Carnevale NT (1999) Passive normalization of synaptic integration influenced by dendritic architecture. *J Neurophysiol* 82:3268–3285.

Jaffe DB, Ross WN, Lisman JE, Lasser-Ross N, Miyakawa H, Johnston D (1994) A model for dendritic ca2+ accumulation in hippocampal pyramidal neurons based on fluorescence imaging measurements. *Journal of Neurophysiology* 71:1065–1077.

Jarsky T, Roxin A, Kath WL, Spruston N (2005) Conditional dendritic spike propa-

gation following distal synaptic activation of hippocampal ca1 pyramidal neurons. *Nat Neurosci* 8:1667–1676.

Johnston D, Wu S (1995) *Foundations of Cellular Neurophysiology* A Bradford book. Mit Press.

Jones E, Oliphant T, Peterson P et al. (2001–) SciPy: Open source scientific tools for Python.

Kingma D, Ba J (2014) Adam: A method for stochastic optimization. *arXiv preprint arXiv:1412.6980* .

Klausberger T, Magill PJ, Márton LF, Roberts JDB, Cobden PM, Buzsáki G, Somogyi P (2003) Brain-state- and cell-type-specific firing of hippocampal interneurons in vivo. *Nature* 421:844–848.

Klausberger T, Somogyi P (2008) Neuronal diversity and temporal dynamics: the unity of hippocampal circuit operations 321:53–57.

Koch C, Douglas R, Wehmeier U (1990) Visibility of synaptically induced conductance changes: theory and simulations of anatomically characterized cortical pyramidal cells. *J Neurosci* 10:1728–1744.

Koch C, Poggio T, Torre V (1983) Nonlinear interactions in a dendritic tree: localization, timing, and role in information processing. *Proceedings of the National Academy of Sciences* 80:2799–2802.

LeCun Y, Cortes C, Burges CJ (2010) Mnist handwritten digit database. *AT&T Labs [Online]. Available: http://yann. lecun. com/exdb/mnist* 2.

Levemberg K (1944) A method for the solution of certain problems nonlinear in least square. *Quarth. Appl. Math* 2:164–168.

Lorente De Nó R (1947) Action potential of the motoneurons of the hypoglossus nucleus. *Journal of cellular physiology* 29:207–287.

Lörincz A, Notomi T, Tamás G, Shigemoto R, Nusser Z (2002) Polarized and compartment-dependent distribution of hcn1 in pyramidal cell dendrites. *Nature neuroscience* 5:1185.

Magee JC, Johnston D (1995) Characterization of single voltage-gated na+ and ca2+ channels in apical dendrites of rat ca1 pyramidal neurons. *The Journal of physiology* 487:67–90.

Maier N, Nimmrich V, Draguhn A (2003) Cellular and network mechanisms underlying spontaneous sharp wave-ripple complexes in mouse hippocampal slices. *J Physiol* 550:873–887.

Maier N, Tejero-Cantero A, Dorrn AL, Winterer J, Beed PS, Morris G, Kempter R, Poulet JFA, Leibold C, Schmitz D (2011) Coherent phasic excitation during hippocampal ripples. *Neuron* 72:137–152.

Makarov VA, Makarova J, Herreras O (2010) Disentanglement of local field potential sources by independent component analysis. *J Comput Neurosci* 29:445–457.

Makarova J, Ibarz JM, Makarov VA, Benito N, Herreras O (2011) Parallel readout of pathway-specific inputs to laminated brain structures. *Front Syst Neurosci* 5:77.

Margulis M, Tang CM (1998) Temporal integration can readily switch between sublinear and supralinear summation. *Journal of neurophysiology* 79:2809–2813.

Martín-Vázquez G, Benito N, Makarov VA, Herreras O, Makarova J (2015) Diversity of lfps activated in different target regions by a common ca3 input. *Cereb Cortex* .

Milner B, Corkin S, Teuber HL (1968) Further analysis of the hippocampal amnesic syndrome: 14-year follow-up study of hm. *Neuropsychologia* 6:215–234.

Moré JJ (1978) The levenberg-marquardt algorithm: implementation and theory In *Numerical analysis*, pp. 105–116. Springer.

Müller C, Remy S (2013) Fast micro-iontophoresis of glutamate and gaba: A useful tool to investigate synaptic integration. *Journal of visualized experiments: JoVE* .

Naundorf B, Wolf F, Volgushev M (2006) Unique features of action potential initiation in cortical neurons. *Nature* 440:1060–1063.

Neher E, Sakmann B (1976) Single-channel currents recorded from membrane of denervated frog muscle fibres. *Nature* 260:799–802.

Nevian T, Larkum ME, Polsky A, Schiller J (2007) Properties of basal dendrites of layer 5 pyramidal neurons: a direct patch-clamp recording study. *Nat Neurosci* 10:206–214.

Numberger M, Draguhn A (1996) *Patch-Clamp-Technik* Spektrum Akad. Verlag.

O'Keefe J, Conway DH (1978) Hippocampal place units in the freely moving rat: why they fire where they fire. *Exp Brain Res* 31:573–590.

Pods J, Schönke J, Bastian P (2013) Electrodiffusion models of neurons and extracellular space using the poisson-nernst-planck equationsnumerical simulation of the

intra-and extracellular potential for an axon model. *Biophysical journal* 105:242–254.

Poirazi P, Mel BW (2001) Impact of active dendrites and structural plasticity on the memory capacity of neural tissue. *Neuron* 29:779–796.

Rall W (1957) Membrane time constant of motoneurons. *Science* 126:454.

Rall W (1959) Branching dendritic trees and motoneuron membrane resistivity. *Exp Neurol* 1:491–527.

Rall W (1960) Membrane potential transients and membrane time constant of motoneurons. *Exp Neurol* 2:503–532.

Rall W (1969) Distributions of potential in cylindrical coordinates and time constants for a membrane cylinder. *Biophys J* 9:1509–1541.

Rall W (1970) Cable properties of dendrites and effects of synaptic location. *Excitatory synaptic mechanisms* 1:175–187.

Rall W (1964) Theoretical significance of dendritic trees for neural input-output relations. *Neural theory and modeling* .

Rall W (1967) Distinguishing theoretical synaptic potentials computed for different soma-dendritic distributions of synaptic input. *Journal of neurophysiology* 30:1138–1168.

Ramón y Cajal S (1911) Histologie du syste me nerveux de i'homme et des verte be s. *Maloine (Paris)* 2:891–942.

Reichinnek S, Künsting T, Draguhn A, Both M (2010) Field potential signature of distinct multicellular activity patterns in the mouse hippocampus. *J Neurosci* 30:15441–15449.

Remy S, Csicsvari J, Beck H (2009) Activity-dependent control of neuronal output by local and global dendritic spike attenuation 61:906–916.

Robinson HP, Kawai N (1993) Injection of digitally synthesized synaptic conductance transients to measure the integrative properties of neurons. *Journal of neuroscience methods* 49:157–165.

Schiller J, Schiller Y (2001) Nmda receptor-mediated dendritic spikes and coincident signal amplification. *Current opinion in neurobiology* 11:343–348.

Scoville WB, Milner B (1957) Loss of recent memory after bilateral hippocampal lesions. *Journal of neurology, neurosurgery, and psychiatry* 20:11.

Segev I, Rall W (1998) Excitable dendrites and spines: earlier theoretical insights elucidate recent direct observations. *Trends Neurosci* 21:453–460.

Shepherd GM, Brayton RK, Miller JP, Segev I, Rinzel J, Rall W (1985) Signal enhancement in distal cortical dendrites by means of interactions between active dendritic spines. *Proc Natl Acad Sci U S A* 82:2192–2195.

Singer AC, Carr MF, Karlsson MP, Frank LM (2013) Hippocampal swr activity predicts correct decisions during the initial learning of an alternation task. *Neuron* 77:1163–1173.

Spencer W, Kandel E (1961) Electrophysiology of hippocampal neurons: Iv. fast prepotentials. *Journal of Neurophysiology* 24:272–285.

Spruston N, Jonas P, Sakmann B (1995) Dendritic glutamate receptor channels in rat hippocampal CA3 and CA1 pyramidal neurons. 482:325–352.

Spruston N, Jaffe DB, Johnston D (1994) Dendritic attenuation of synaptic potentials and currents: the role of passive membrane properties 17:161–166.

Sterratt D, Graham B, Gillies A, Willshaw D (2011) *Principles of computational modelling in neuroscience* Cambridge University Press.

Tchumatchenko T, Malyshev A, Wolf F, Volgushev M (2011) Ultrafast population encoding by cortical neurons. *J Neurosci* 31:12171–12179.

Tchumatchenko T, Wolf F (2011) Representation of dynamical stimuli in populations of threshold neurons. *PLoS Comput Biol* 7:e1002239.

Thome C, Kelly T, Yanez A, Schultz C, Engelhardt M, Cambridge SB, Both M, Draguhn A, Beck H, Egorov AV (2014) Axon-carrying dendrites convey privileged synaptic input in hippocampal neurons. *Neuron* 83:1–13.

Traub RD, Schmitz D, Maier N, Whittington MA, Draguhn A (2012) Axonal properties determine somatic firing in a model of in vitro ca1 hippocampal sharp wave/ripples and persistent gamma oscillations. *Eur J Neurosci* 36:2650–2660.

Van Oosterom A, De Boer R, Van Dam RT (1979) Intramural resistivity of cardiac tissue. *Medical and Biological Engineering and Computing* 17:337–343.

Velazquez JLP, Carlen PL (2000) Gap junctions, synchrony and seizures. *Trends in neurosciences* 23:68–74.

Vladimirov N, Tu Y, Traub RD (2013) Synaptic gating at axonal branches, and sharp-wave ripples with replay: a simulation study. *Eur J Neurosci* 38:3435–3447.

Wheeler DW, White CM, Rees CL, Komendantov AO, Hamilton DJ, Ascoli GA (2015) Hippocampome.org: a knowledge base of neuron types in the rodent hippocampus 4:e09960.

Yu Y, Shu Y, McCormick DA (2008) Cortical action potential backpropagation explains spike threshold variability and rapid-onset kinetics. *J Neurosci* 28:7260–7272.

Zeiler MD (2012) Adadelta: an adaptive learning rate method. *arXiv preprint arXiv:1212.5701* .

Zemankovics R, Káli S, Paulsen O, Freund TF, Hájos N (2010) Differences in subthreshold resonance of hippocampal pyramidal cells and interneurons: the role of h-current and passive membrane characteristics. *The Journal of physiology* 588:2109–2132.